View metadata, citation and similar papers at core.ac.uk
brought to you by CORE
provided by ScholarBank@NUS

RECEIVER DESIGN AND PERFORMANCE ANALYSIS FOR COMMUNICATION CHANNELS WITH CARRIER PHASE NOISE AND FADING

WANG QIAN
(*B.Eng., Harbin Engineering University*)

A THESIS SUBMITTED
FOR THE DEGREE OF DOCTOR OF PHILOSOPHY
DEPARTMENT OF ELECTRICAL AND COMPUTER ENGINEERING
NATIONAL UNIVERSITY OF SINGAPORE
2016

Dedications:

To my loving parents

and my family who love me always.

Declaration

I hereby declare that this thesis is my original work and it has been written by me in its entirety. I have duly acknowledged all the sources of information which have been used in the thesis.

This thesis has also not been submitted for any degree in any university previously.

Wang Qian

WANG Qian

12 August 2016

Acknowledgment

First and Foremost, I would like to thank my supervisor, Prof. Pooi-Yuen Kam for his invaluable guidance and support throughout the past few years. From him, I learnt not only knowledge and research skills, but also the right attitude and passion towards research. I am also very grateful for his understanding and patience when I face difficulty in work. His wisdom, experience, and passion are admirable and I am really fortunate to have had him as my supervisor.

I would like to thank Prof. Mohan Gurusamy and Prof. Hoon Kim for serving as my Ph.D qualification examiners. I would like to thank Prof. Rui Zhang and Prof. Yan-Fu Tan for being my thesis examiners. I really appreciate their insightful comments.

I would also like to give my special thanks to Prof. Changyuan Yu, who allows me to attend his regular group meetings and has been providing insightful discussions and helpful suggestions. From him and other members of his group, I have learned a lot that are significantly helpful in my own research.

I would like to thank fellow researchers Song Tianyu, Wu Mingwei, Yuan Haifeng, Fu Hua, Lin Xuzheng, Liu Liang, Wu Gaofeng, Zhou

Xun, Xu Zhuoran, Cao Shengjiao, Wang Yu, Wu Tong, Yu Yi, Luo Shixin, Jia Chenlong, Guo Zheng, Hu Qikai, Zhou Jingjing, Zheng Huanhuan, Zhang Shuowen, Kang Seungmin, Utku Tefek, Guo Yinghao, Chen Can, Hu Yang, Li Yan and many others for their help in my research and other ways. I would also like to thank my sincere friends Li Xuefang and Ding Jie for their emotional support during my research life.

I grateful acknowledge the support of part of my research studies by the National University of Singapore in the form of a President's Graduate Fellowship.

Last but not least, I would like to express my sincere appreciation to my family for their love, encouragement and support that have always comforted and motivated me.

Table of Contents

Summary

In most communications, e.g., fiber-optic and wireless communications, advanced two-dimensional carrier modulation formats, such as M-ary phase shift keying (MPSK), M-ary quadrature amplitude modulation (M-QAM) and M-ary amplitude phase-shift keying (M-APSK), are commonly used for higher spectral efficiencies. Coherent detection of high order phase-modulated signals is easily impaired by phase noise due to the imperfect transmitter and receiver local oscillators, in addition to usual thermal, additive, white, Gaussian noise (AWGN). Carrier phase estimation (PE) with PE algorithms is imperative, producing a noisy phase reference which degrades the system performance. In the general situation, a non-zero phase reference error (PRE) always exists due to the oscillator phase noise and a finite signal-to-noise ratio (SNR) in phase estimation. However, most engineers ignore this PRE and still use the suboptimal minimum Euclidean-distance (MED) detector, which does not consider the PRE and results in a degraded system performance. The design of an optimum detector taking the PRE into account is challenging, but no complete theory has been developed for this detection problem so far. This thesis thus studies the issues of coherent detector design and error performance analysis with PRE considered for the phase noise channel.

We first consider the design of the optimum detector for two-dimensional amplitude/phase modulated signals received in AWGN and a Gaussian distributed PRE due to imperfect PE. We propose a novel approach of using the amplitude and phase information of the received signal, based on viewing the AWGN as an equivalent additive, observation phase noise (AOPN) whose statistics is Tikhonov. This allows the AOPN to be combined with PRE, and the maximum *a posterior*

probability/maximum-likelihood (ML) detection scheme to be readily derived in amplitude-phase form. This amplitude-phase approach is simpler and more convenient than the conventional method that uses the in-phase and quadrature components of signals received in phase noise. For constellations which have multiple rings, e.g., M-QAM and M-APSK, the conventional MED detector without considering the PRE is actually suboptimum. The ML detector for equi-probable signals is structurally very different from the MED detector, and it is very computationally inefficient. Thus, simpler and closed-form approximations to the ML detector are given, which can be easily implemented on-line. The approximate ML decision boundaries for both 8-star QAM and rotated 8-star QAM are illustrated as examples and shown to be not necessarily straight lines. As the variance of PRE or the SNR or both increase, the decision boundaries between two adjacent signal rings asymptotically become circular. This leads to a suboptimal detector which we call an annular-sector (AS) detector. This AS detector performs amplitude detection and phase detection separately and employs an annular sector as the decision region for each signal point.

Using the amplitude-phase form of the received signal model in the presence of AWGN and PRE, we provide a unified and systematic approach to predicting the error probability of MPSK, M-QAM and M-APSK with coherent detection. Our approach is based on that the Tikhonov probability density function (pdf) of the AOPN can be accurately approximated by a Gaussian pdf, which leads to an approximate Gaussian AOPN+PRE model. This facilitates the computation of the probability of the received signal phasor falling in any sector in the complex plane, which thus enables us to express the symbol error probability (SEP) and bit error probability (BEP) of MPSK with the ML detector and Gray code mapping in terms of Gaussian Q-functions. Moreover, simple, accurate and closed-form approximations to the SEP of the AS detector are obtained for both 16QAM and general M-APSK. All these expressions provide explicit insights into how the PRE variance affects the performance.

Differential detection is the special case of coherent detection, which takes only the previous signal to form the phase reference. Due to its simplicity in practical implementation, it is also considered here. Our amplitude-phase-form method can be easily generalized to obtain the SEP and BEP results of Gray coded M-ary differential phase shift keying (MDPSK) with differential detection in phase noise.

To further improve the error performance of coherent receivers with PRE, we address the issue of optimizing signal constellations. Our newly derived SEP results facilitate the constellation optimization in phase noise, which only requires numerical computation and avoids extensive simulations. By minimizing the SEP of the AS detector, we give M-APSK with optimized ring radii as examples.

All the work above provides a good example to show the importance of using the amplitude-phase statistics for analysis in the phase noise channel. In contrast to the in-phase and quadrature form of the received signal, the amplitude-phase-form signal model facilitates receiver design and performance analysis in phase noise.

For wireless communications, multipath fading and shadowing inevitably cause amplitude attenuation of the received signal. The average error performance of coherent receivers over fading is thus analysed, and we assume perfect phase tracking to simply illustrate our novel approach. The approach is to use the tight upper and lower bounds on the Gaussian Q-function we derived recently, which can be easily averaged over the general mixture gamma (MG) distribution. The MG distribution is used to approximate the SNR distributions of a class of composite fading models, which include the Nakagami-m, Generalized-K (K_G) and Nakagami-lognormal fading as specific examples. We thus obtain tight, simple algebraic-form bounds and invertible expressions for the average symbol error probability (ASEP) of MPSK in a class of composite fading channels. This approach also facilitates analysing the effects of atmospheric turbulence and pointing errors on free space optical communication systems where intensity modulation with direct detection is usually employed. Especially for inter-satellite links with pointing errors only, we derive closed-form and invertible approximations to the ASEP from which we can easily

get the diversity gain. Furthermore, a closed-form outage probability expression for the combined effects is obtained.

List of Tables

List of Figures

List of Acronyms

AWGN	Additive White Gaussian Noise
AOPN	Additive Observation Phase Noise
ASEP	Average Symbol Error Probability
ABEP	Average Bit Error Probability
AS	Annular-Sector
BEP	Bit Error Probability
BPSK	Binary Phase Shift Keying
DA	Decision-Aided
DB	Decision Boundaries
FSO	Free Space Optical
GL	Gamma-Lognormal
IEEE	Institute of Electrical and Electronics Engineers
IM/DD	Intensity Modulation with Direct Detection
K_G	Generalized-K
MPSK	M-ary Phase Shift Keying
MDPSK	M-ary Differential Phase Shift Keying
M-QAM	M-ary Quadrature Amplitude Modulation
M-APSK	M-ary Amplitude Phase-Shift Keying
MAP	Maximum *A Posterior* Probability
ML	Maximum Likelihood
MED	Minimum Euclidean Distance
MG	Mixture Gamma
MGF	Moment Generating Function

NL	Nakagami-Lognormal
OOK	On-Off Keying
pdf	Probability Density Function
PE	Phase Estimation
PRE	Phase Reference Error
PLL	Phase-Locked Loop
QPSK	Quadrature Phase Shift Keying
RF	Radio Frequency
RPN	Residual Phase Noise
RL	Rayleigh Lognormal
SNR	Signal-to-Noise Ratio
SEP	Symbol Error Probability

List of Notations

$(\cdot)^T$	the transpose of a vector or a matrix
$(\cdot)^*$	the conjugate only of a scalar or a vector or a matrix
$(\cdot)^H$	the Hermitian transpose of a vector or a matrix
$\lvert \cdot \rvert$	the absolute value of a scalar
$\lVert \cdot \rVert$	the Euclidean norm of a vector
$\lVert \cdot \rVert_F$	the Frobenius norm of a matrix
$\mathbb{E}[\cdot]$	the statistical expectation operator
$\mathrm{Re}[\cdot]$	the real part of the argument
$\mathrm{Im}[\cdot]$	the imaginary part of the argument

Chapter 1

Introduction

Both fiber-optic and wireless data communications have become increasingly vital parts of our modern daily life. Data transmission in fiber-optic channels is prone to damage by linear impairments (e.g., laser phase noise), frequency offset between the transmitter and local oscillator lasers, and fiber nonlinearity [1–3]. The phase-modulated optical signals transmitted in the fiber are further distorted by the linear effects of fiber chromatic and polarization-mode dispersion. Besides, fiber self-phase modulation effect limits the performance of long-haul phase-modulated transmission systems through nonlinear phase noise [4, 5], which is closely related to the power of each symbol. We will not deal with nonlinear phase noise in the thesis. Among these impairments, laser phase noise plays a significant role in affecting the performance of coherent receivers. We assume here that all the dispersions and nonlinear impairments have been compensated for by optical means, and laser phase noise is mainly considered. Moreover, for optical wireless communications, especially with synchronous receiver with phase tracking, the laser sources for both transmitter and local oscillators can hardly be "coherent", which results in unknown phase noise [6].

Signals in wireless communications also experience oscillator phase noise, which limits the sensitivity of a coherent receiver for phase-modulated signals. The linear phase noise is due to the phase fluctuation or incoherence of the imperfect transmitter and receiver local oscillators [7–10]. Oscillators inherently produce high levels of phase noise. It is known that phase noise in RF oscillators increases with carrier frequency. Phase noise in a transmit chain will "leak" power into adjacent channels, and there is a continuum of local oscillators that can mix with interfering

signals [7,8]. On the other hand, due to the constructive and destructive combination of randomly delayed, reflected, scattered, and diffracted signal components in wireless channels, multipath fading causes an attenuation in the signal amplitude or phase [11, 12]. In the case where transmitter, receiver or objects in the environment are moving, the signal frequency is also affected due to Doppler shift. Due to mobility, the applicable channel statistics may change over time. There are a lot of fading models widely used, e.g., Rayleigh fading, Rician fading and Nakagami-m fading, each with one or more fading parameters. Therefore, for any communication scheme, two main concerns are carrier phase noise and fading.

All the time, two fundamental research issues are receiver design and performance analysis. The aim of receiver design is to develop an optimum receiver structure that minimizes the probability of decision errors. Receiver design depends on the channel model and the knowledge of the channel statistics at the receiver, and more and more cost-effective and flexible receiver design schemes are being sought for [2,13]. Performance analysis aims to derive error probability or outage probability in a mathematical expression, which enables one to see the insights on how the system parameters affect the system performance and thus to do performance optimization efficiently [14]. Advanced two-dimensional carrier modulation formats, such as M-ary phase-shift keying (MPSK) and differential phase-shift keying (MDPSK), and M-ary quadrature amplitude modulation (M-QAM) and amplitude phase-shift keying (M-APSK), are commonly used for higher spectral efficiencies [15–19]. In wireless and mobile communication links, higher-order M-APSK are especially popular recently [19–21]. M-APSK exhibits a near-capacity performance under peak-power-limited channels [22], and is considered as the most preferred modulation mechanism for nonlinear satellite transmission [22–24]. M-APSK is already adopted by the second generation digital video broadcasting specification for satellite (DVB-S2) and approved by the consultative committee for space data systems (CCSDS) [24]. For 8-point star QAM (8-star QAM and rotated 8-star QAM included), the angular distance between adjacent symbols is $\pi/2$, larger than

that of other possible 8-ary constellations. This makes 8-point star QAM more phase-noise-tolerant, perform well at large phase noise and have large laser linewidth tolerance. Thus, 8-star QAM and rotated 8-star QAM are considered as promising modulation formats in coherent optical communications [25, 26].

Most times, the in-phase and quadrature statistics of the received signal is used for analysis, which turns out to be not very simple for the phase noise channel. Here, we want to emphasize a new perspective of using the received amplitude and phase information in phase noise, which enables us to do receiver design and performance analysis more intuitively and conveniently.

In this chapter, we first give an overview of receiver design in phase noise channel and our research objective in detector design in Section 1.1. We then give an overview of performance analysis in carrier phase noise and fading, respectively, and our detailed research objectives in Section 1.2. In Section 1.3, we give a summary on our main contributions in the two areas. Finally, we present the organization of the thesis in Section 1.4.

1.1 Receiver Design

The issue of designing wireless systems to operate in the presence of oscillator phase noise is classical in communication theory. Recently, there is renewed interest in this problem [9,10]. One of the main reasons is the unprecedented explosion in the number of wireless and mobile devices that are enabled for communication-intensive and bandwidth hungry applications. The use of inexpensive, noisy oscillators in such systems is therefore inevitable. Phase noise is also dominant in communication systems that operate over millimeter-wave bands like 60Ghz and higher. In this regard, more cost-effective, flexible, high speed connectivity solutions are being sought for [9, 10].

Prior to data detection, one challenge in coherent systems is to recover the carrier phase, which is easily perturbed, for instance, by laser phase noise in fiber-optic communications [27, 28] or oscillator phase noise in wireless

communications [7, 29]. In early stage of coherent receivers, a phase-locked loop (PLL) is normally used to track the carrier phase with respect to the local oscillator carrier. However, for optical communications, optical PLLs operating at optical wavelengths in combination with distributed feedback lasers are difficult to implement due to the large product of laser linewidth and loop delay [30]. Instead of using bulky and complicated optical components, digital signal processing (DSP) algorithms have played a vital role in compensating for the fiber transmission impairments in digital coherent receivers recently [31]. With the aid of high-speed analog-to-digital converters, carrier phase estimation (PE) can be done in high-speed DSP units rather than using optical PLLs for unknown carrier phase tracking. DSP-based PE techniques, such as Wiener filter [32, 33] and Kalman filter [34], are demonstrated via experiments to be very effective to recover carrier phase. The commonly-used Viterbi & Viterbi (V&V) Mth-power scheme is based on a nonlinear transformation of received MPSK signals [35]. This Mth-power scheme is further extended to M-QAM formats in [27] and modified in [36, 37]. Although it is capable of accurately tracking, this Mth-power scheme relies heavily on nonlinear computations, such as rectangular-to-polar or inverse transformations, and phase unwrapping, which increase power consumption and memory requirements [38]. To address the nonlinear computations, [15,28] introduce a computationally-linear decision-aided maximum likelihood (DA ML) PE into coherent optical communication systems, to eliminate the nonlinear operations while keeping or even improving the laser linewidth tolerance. Reference [15] shows that the optimal memory length of DA ML can be calculated when the statistics of the additive noise and phase noise are known. Similar to the Mth-power algorithm, DA ML is also subjected to block length effect because of the trade-off between averaging over additive noise and phase noise [39]. Moreover, the DA ML phase estimation scheme performs similar to the Mth-power scheme in linear phase noise, and it outperforms the Mth-power scheme when nonlinear phase noise exists as the main distortion [40]. In the general situation, a noisy phase reference is produced by the

phase estimation (PE) algorithm due to laser phase noise and a finite signal-to-noise ratio (SNR). Thus, we usually have a phase reference error (PRE) for data detection which degrades the system performance.

After phase estimation, a robust and simple detector that is easy to implement is imperative, as our demand on the system reliability increases. For different channel models, different data detection techniques are considered in receiver design, e.g., coherent detection, differential detection, sequence detection, depending on the signal model and receiver knowledge [41–44]. Differential encoding and differential detection is a viable alternative that does not require channel state information or explicit carrier PE, which, however, incurs substantial performance loss compared to coherent detection. For instance, the performance of MDPSK is about 3dB worse than that of coherent MPSK [14]. Thus, coherent detection of phase-modulated signals impaired by thermal, additive, white, Gaussian noise (AWGN) as well as laser or oscillator phase noise are commonly considered [2, 45–47]. The design of the maximum likelihood (ML) (optimum) detector that takes the PRE into account is challenging [48–50], but no complete theory has been developed for this detection problem so far. The optimum decision regions for equi-probable signals are much complicated [50]. Mostly, the conventional minimum Euclidean distance (MED) detector is used [2, 26, 51], although it is optimal when only AWGN exists. A two-stage detector consisting of a radius detector, an amplitude-dependent phase rotation and a phase detector, is first proposed in [49] and further discussed in [52,53] for strong nonlinear phase noise. This two-stage detector works well at high SNR, and asymptotically becomes optimal for larger phase noise. However, all these detectors are suboptimal in phase-noise channel, and there has been limited research on the systematic derivation of the ML (optimum) detector in closed-form [50].

Therefore, with the efficient phase estimation algorithms applied, we aim to introduce a novel approach in designing a robust, optimum, symbol-by-symbol detector for communication channels with carrier phase noise. This detector should be applicable to any two-dimensional carrier modulations.

1.2 Performance Analysis

For communication channels where carrier phase noise exists, it is of great interest to be able to quickly and accurately predict the symbol/bit error probability (SEP/BEP) of higher-order phase-modulated signals with coherent detection in the presence of AWGN and PRE [46, 54–58]. However, only limited research on specific modulations has been done before, for instance, [59] gives the generalized BER expressions of MPSK in the presence of phase error. No unified, analytically tractable approach has been developed for any two-dimensional carrier modulations so far, to derive simple, closed-form SEP expressions of the ML detector taking the PRE into account. For MDPSK with differential detection, it is also of importance to be able to quickly estimate the SEP/BEP in the presence of AWGN and residual phase noise (RPN) [60–63]. Without the closed-form results, constellation optimization for better system performance can only be carried on via extensive simulations which cost a lot of time. Some search methods have been proposed in [53] and the references therein to weaken the problem of efficiency. Hence, the mathematically tractable results, which can provide explicit insights into how the parameters affect the error performance and can be used to systematically optimize constellations in phase noise, are highly in demand.

Similarly, many unsolved problems remain in the performance analysis of fading channels. We want to obtain the performance metrics in simple and closed forms, such that it is straightforward for system designers to specify required SNR to meet a certain level of system performance. The widely used performance metrics in fading channels are average symbol error probability (ASEP) and average bit error probability (ABEP). They are obtained by averaging the instantaneous SEP or BEP values over the fading distribution. The instantaneous SEP and BEP are equivalent to the SEP and BEP of an AWGN channel with a given instantaneous fading gain or SNR. For most modulation formats, the instantaneous SEP and BEP usually involve the Gaussian Q-functions, or integrals of exponential functions. Thus, averaging the instantaneous SEP or BEP over fading may not result in a closed form, and

may involve special functions [12]. In addition, in a shadowed fading environment, shadowing statistics need to be considered as well, which increases the complexity of performance analysis. Hence, [64–66] address the system outage caused by the shadowing effect. The existing results for the exact ASEP of MPSK either involve numerical integration of moment generating functions (MGF), such as in [12, 67] for the composite multipath/shadowing fading channels, or numerically computing higher-order transcendental functions as in [64, 68–70] for Rayleigh/Ricean and Nakagami-m fading. For example, for Nakagami-m fading with arbitrary m, the ASEP and ABEP results are expressed in terms of Gauss hypergeometric function or Lauricella function [68,69]. They are complicated in general, and do not facilitate further analysis of error performance with respect to the system parameters. In this way, we need to consider new mathematical approaches, such as simple, tight and closed-form bounds to approximate the ASEP/ABEP. Actually, although the Gaussian Q-function involved is conventionally defined as the area under the tail of a normalized Gaussian random variable with zero mean and unit variance, it is also expressed as a finite range integral of an exponential function in [71]. By applying the Jensen's inequality on the integral form, tight bounds on the Gaussian Q-function are derived for simple forms which can be easily averaged over fading [72–75]. Moreover, a number of composite fading models to model the effect of multipath fading and shadowing have been developed, such as the Generalized-K (K_G), Nakagami-lognormal (NL), $\eta-\mu$, $\kappa-\mu$, Nakagami-q (Hoyt) and Nakagami-n (Rician) fading [12]. For simple analysis, several composite distributions have been proposed to approximate the distributions of these composite fading models, including the G-distribution [76], the mixture gamma (MG) distribution [77,78], the mixture of Gaussian distribution [79] and the H-fading model [80]. Recently, the use of the MG distribution for capacity and error probability analysis has become very popular [81–85], since the MG distribution is versatile and mathematically tractable.

Even moving on to free space optical (FSO) communications with frequent use of intensity modulation and direct detection, atmospheric turbulence, geometric

spread and pointing errors cause fluctuations in the intensity of the received signal and degrade FSO link performance. The pointing errors are due to platform vibrations, which cause vibrations of the transmitter telescope and, therefore, misalignment between the transmitter and the receiver [86, 87]. Especially, long distance inter-satellite laser communication links are highly vulnerable due to the degrading effect of pointing errors [86–90]. Various statistical models have been proposed over the years to describe the pointing errors [86, 88]. In these works, the effects of misalignment on the error performance have been investigated. However, the existing results for the ABEP involve numerical multiple integrals [86], or numerically computing higher-order transcendental functions [87]. No simple, closed-form expressions for the ABEP are given so far, and the diversity gain cannot be easily derived. Therefore, by using the bounds on the Gaussian Q-function and exploring new approximations to the SNR distributions of fading models, we aim to find tight bounds and invertible approximations to the ASEP/ABEP for simpler analysis.

1.3 Main Contributions

1.3.1 The Amplitude-Phase Form

We will show that using the amplitude and phase information of the received signal is very important for the phase noise channel. In contrast to the in-phase and quadrature form of the received signal, the amplitude-phase-form received signal model facilitates receiver design and performance analysis in phase noise. The received phase incorporates the AWGN and carrier phase noise together. It is based on viewing the AWGN as an equivalent phase noise that is described by an additive, observation phase noise (AOPN) model that we developed in [91]. The AOPN has a conditional probability density function (pdf) which is Tikhonov, when conditioned on knowing the received signal amplitude.

1.3.2 Coherent Detector Design

We design a coherent receiver that works well for any high-order amplitude/phase-modulated signals in communication channels with Brownian motion carrier phase noise.

This thesis considers a receiver that consists of a phase estimation algorithm preceding the data detector. To be specific, we mainly consider the use of the DA ML phase estimator in [15, 45], which leads to a PRE. We then propose a unified amplitude-phase-representation approach to derive the maximum *a posterior* probability (MAP)/ ML detector for two-dimensional carrier modulations in the presence of AWGN and PRE. The AOPN due to the AWGN is combined with the PRE, and the use of the received amplitude and phase information leads to a more convenient and simpler analysis than using the conventional method of using the in-phase and quadrature components of the received signal. We show that for MPSK which only has one ring of signal points, the ML detector, for any PRE variance, performs the same as the MED detector which is derived without taking phase noise into account. On the other hand, for multiple-ring constellations, the ML detector is the same as the MED detector only when no PRE exists. In general, the ML detector is very computationally inefficient for implementation in real time. Thus, closed-form, simpler approximations of the ML detector are obtained, and they are shown in simulations to perform almost the same as the exact one. More importantly, when PRE exists, our approximate ML detectors perform much better than the MED detector which is suboptimal and always leads to straight-line decision boundaries (DB).

For large PRE or for high SNR, the approximately optimal DB resulting from the approximate ML detectors asymptotically become circular between signal rings, thus leading to annular sectors as decision regions. This implies that the performance of the ML detector approaches that of what we call the annular-sector (AS) detector here, for increasing input power or PRE variance. It is worth noting that for the special case of an M-APSK constellation, such as 8-star QAM where each ring

has the same number of signal points with the same phase values, our simplest approximate ML detector further simplifies to an equivalent structure that performs ring detection and phase detection separately, and always leads to circular decision boundaries in the middle of two rings corresponding to the AS detector. The AS detector does not depend on the channel parameters: AWGN spectrum density and PRE variance. Our work here provides a unified view of all the existing suboptimal detectors in the presence of linear phase noise.

1.3.3 Performance Analysis

The impact of carrier phase noise on the error performance of amplitude/phase-modulated signals in communication channels will be analyzed here in detail. Our novel approach lies in showing that for high SNR, the Tikhonov pdf of the AOPN is well approximated by a Gaussian pdf. This AOPN can be combined with the PRE or RPN, and the distribution of this combined phase noise (AOPN + PRE/RPN) is approximately Gaussian. This Gaussian AOPN+PRE/RPN model leads to a simple expression for the probability of the received signal phasor falling in any sector in the complex plane. We illustrate its application to the computation of the SEP/BEP of MPSK/MDPSK for $M \geq 4$ in phase-noise channels. Our SEP/BEP results are all expressed as linear combinations of single Gaussian Q-functions. For comparison, the exact SEP/BEP results for MDPSK ($M \geq 4$) with RPN are first derived here via [92, eqs.(9)(11)]. Our unified approach is mathematically simpler and increasingly more accurate for larger values of M. Using the suboptimum annular-sector detector, we also derive explicit, closed-form SEP expressions for 16QAM and general M-APSK (8-point star QAM included). It is shown that within a large range of PRE variances, these SEP approximations agree very well with the Monte Carlo simulations for all SNR values of interest. These results facilitate constellation optimization without extensive simulations, and enable us to optimize by numerical computation only. Here, we give M-APSK optimization for minimum SEP as an example in strong

phase noise.

For performance analysis in wireless communications with fading, we mainly analyze the ASEP of coherent receivers with perfect phase track. We focus on the mixture gamma (MG) distribution in [77] using the Gauss-quadrature approximations, to approximate different composite fading models. Our approach to the error performance analysis is to obtain tight, algebraic-form bounds on the ASEP of MPSK over the MG distributed fading. It is based on arbitrarily tight upper and lower bounds on the Gaussian Q-function we derived recently in [72, 73], which can be easily averaged over this general MG distribution. We first consider higher-order MPSK ($M > 2$) of single diversity, based on the union upper bound on the conditional SEP which is a single Gaussian Q-function [12]. Using our upper bound on the Gaussian Q-function, we first derive a tight upper bound on the exact ASEP of MPSK ($M > 2$) for the MG distribution. This work is easily specialized to the Nakagami-m, the K_G and the NL composite fading models whose SNR distributions are well approximated by the MG distribution with suitable choices of parameters. These bounds can be further used as good approximations which are invertible for high SNR, and they offer insights into how the parameters determine system performance in fading. For the special case of BPSK ($M = 2$) where the conditional SEP/BEP is exactly one Gaussian Q-function, algebraic-form upper and lower bounds are obtained. The bounds can be arbitrarily tight by adjusting the parameters in our bounds on the Gaussian Q-function. By taking the average of the upper and lower bounds, we then obtain very accurate approximations to the exact ASEP/ABEP of BPSK in all the three specific fading models. Moreover, these approximate expressions are also invertible for reasonably high SNR. All these results are simple, requiring no numerical integration or numerical evaluation of higher-order transcendental functions, and involving only simple algebraic expressions with explicit parameters, which are easy to evaluate.

The bounds and invertible results also find applications in FSO communications with intensity modulation and direct detection damaged by atmospheric turbulence,

geometric spread and pointing errors. More importantly, the diversity gain for inter-satellite laser links with pointing errors only is straightforwardly obtained, which is related to the ratio of the equivalent beam radius to the pointing error displacement standard jitter at the receiver. We will show the explicit insights into how the channel parameters affect the ASEP of FSO systems via numerical results.

1.4 Organization of the Thesis

The rest of the thesis is organized as follows.

In Chapter 2, we introduce the received signal models we use for the phase noise channel, which are given in amplitude-phase form. Therein, we propose a new AOPN model, which leads to the Gaussian AOPN+PRE/RPN models. Constellations involved for coherent receivers are also introduced.

In Chapter 3, we propose optimum coherent detectors in amplitude-phase form for communication channels with PRE after imperfect phase estimation. We illustrate the approximate ML DB on 8-point star QAM. Simulations are done to show the validity and superior performance of these detectors.

Chapter 4 goes into the error probability analysis of communication systems impaired by carrier phase noise. A family of closed-form expressions for the SEP and BEP are obtained. Numerical results are given to show the accuracy of our new approximations.

In Chapter 5, constellation optimization for the phase noise channel is considered. Optimization formulations which minimize the SEP are introduced. We specifically provide M-APSK with optimized ring radii as an example.

Chapter 6 analyzes the ASEP over different fading in wireless communications, based on the bounds on the Gaussian Q-function and using the MG distribution. We derive tight bounds and invertible approximations to the ASEP over several composite fading. Our approach is further extended to analyze the influence of atmospheric turbulence and pointing errors on FSO systems using OOK modulation.

Finally, the concluding remarks are drawn in Chapter 7 and possible extensions

of the work in this thesis are recommended.

Chapter 2

Received Signal Model with Phase Noise

Both fiber-optic and wireless communication systems are subject to impairment by linear phase noise due to the transmitter and receiver local oscillators, on top of AWGN [2, 14]. For fiber-optic communications, laser phase noise significantly affects the system performance, and all the dispersions and nonlinear impairments are assumed to be compensated for by using optical devices [3–5]. Thus, laser phase noise is the main issue we consider here [15, 17, 93]. Wireless communication system design in the presence of oscillator phase noise is a classical problem [48]. Due to the unprecedented explosion in the number of wireless and mobile devices, a renewed interest in this problem boosts in recent times. The impact of phase noise on the performance of multiple-input multiple-output systems is also studied in [10,94,95] and the references therein. In this thesis, we only consider a single-input single-output phase noise channel. Phase noise in wireless communication links is due to phase and frequency instability in the local radio frequency (RF) oscillators, which leads to synchronization issues and degrades the system performance [96, 97]. Note that phase noise in RF oscillators increases with frequency [8, 98]. The effect of phase noise is more severe when higher order modulation schemes are used in order to attain high spectral efficiency [50, 91]. We thus provide a general received signal model in a phase noise channel. We assume no inter symbol interference and no time offset.

First, the kth discrete-time, complex received signal $r'(k)$ in the presence of AWGN $n'(k)$, attenuation coefficient h and unknown carrier phase noise $\theta(k)$ is

given by [9, 45, 48]

$$r'(k) = h(k)m(k)e^{j\theta(k)} + n'(k). \tag{2.1}$$

Here, $m(k)$ is the transmitted signal, which takes on each value from the signal set $\{S_i = A_i e^{j\phi_i},\ i = 0, 1, \ldots, M-1\}$ with probability $P(S_i)$, where A_i and ϕ_i are the amplitude and phase of each symbol, and M is the number of signal points. Term $n'(k)$ is a zero-mean, circularly symmetric, complex, Gaussian random variable with variance N_0, where N_0 is the one-sided spectrum of the AWGN. For fiber-optic links, $\theta(k)$ is the laser phase noise from the transmitter and local oscillator lasers and is modeled as a Wiener process [2]. For wireless links, $\theta(k)$ is phase noise resulting from the imperfect and incoherent oscillators at transmitter and receiver [9,45]. The phase of the oscillator drifts randomly and is also modeled as a Wiener process. The random-walk model for $\{\theta(k)\}$ is mostly used, given by [32, 60]

$$\theta(k) = \theta(k-1) + \Delta\theta(k) \tag{2.2}$$

which is a good approximation to the Wiener process. Since only white noise sources are considered in the oscillator, $\Delta\theta(k)$ is a sequence of independent and identically distributed (iid) Gaussian random variables with mean zero and variance σ^2. For optical communications mainly considered here, the power spectrum of laser linewidth Δv has a Lorentzian line-shape, inducing a Gaussian-distributed phase deviation with mean zero and variance [99]

$$\sigma^2 = \sigma_p^2 = 2\pi T(\Delta v)$$

in a symbol interval T. Here, Δv denotes the total 3-dB linewidth for both transmitter and local oscillator lasers. Term $h(k)$ denotes the real amplitude gain, which is normally brought in by channel attenuation in transmission. For fiber optical signals, the path loss in transmission can usually be measured and known,

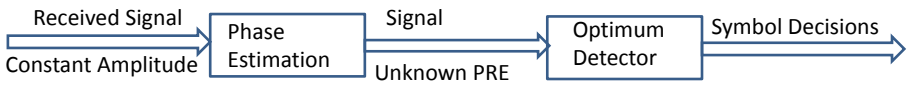

Figure 2.1: Receiver structure in phase noise.

i.e., $h(k) = \text{constant}$ in (2.1) [15]. Moreover, for quasi-static fading channels with oscillator phase noise, the coefficient $h(k)$ is assumed to be deterministic, time-invariant, and known to the receiver [9, 10]. Thus, we assume $h(k) = 1$ in phase noise channel for simplicity.

In the following, the exact signal model used for coherent detection of any two-dimensional carrier modulation in the presence of unknown carrier phase noise is introduced. The high order constellations we will use throughout this thesis are also introduced later.

2.1 The Amplitude-Phase Form for Coherent Detection

Prior to data detection, compensation for the unknown time-varying carrier phase using the estimate from an optical phase-locked loop (PLL) tracking or a phase estimation (PE) algorithm is imperative. In the general situation, a noisy phase reference is produced due to laser phase noise and a finite SNR in the PLL or PE algorithm. Thus, as Fig. 2.1 shows, we usually have a phase reference error (PRE) for data detection which degrades the system performance [15, 45, 46]. At each time $t = kT$ (T =symbol duration), we obtain an estimate $\hat{\theta}(k)$ of the carrier phase $\theta(k)$ using a PE algorithm. After compensation by $\hat{\theta}(k)$, we have the received signal $r(k)$ given by $r(k) = r'(k)e^{-j\hat{\theta}(k)}$. Thus, the received signal over the kth

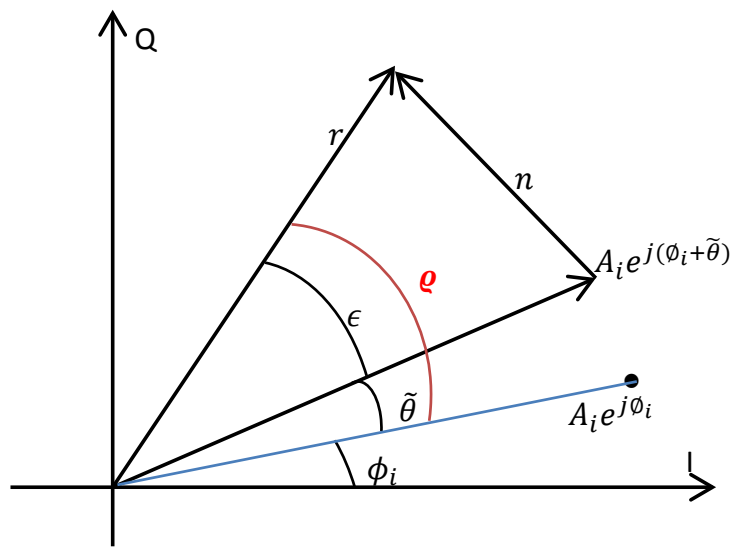

Figure 2.2: Geometric representation of the received signal r of phase-modulated signals.

symbol interval becomes [91]

$$\begin{aligned} r(k) &= m(k)e^{j(\theta(k)-\hat{\theta}(k))} + n'(k)e^{-j\hat{\theta}(k)} \\ &= m(k)e^{j\tilde{\theta}(k)} + n(k). \end{aligned} \tag{2.3}$$

Here, $\tilde{\theta}(k) = \theta(k) - \hat{\theta}(k)$ denotes the PRE. Term $n(k) = n'(k)e^{-j\hat{\theta}(k)}$ is statistically identical to $n'(k)$, i.e., it is complex Gaussian distributed with $n(k) \sim CN(0,\ N_0)$, where CN denotes the complex normal (Gaussian) distribution. We use this model (2.3) as the sufficient statistics in symbol decision.

Next, we motivate the amplitude-phase-form received signal model we will use for the phase noise channel. Fig. 2.2 gives a geometric representation of $m(k)e^{j\tilde{\theta}(k)}$, $n(k)$ and $r(k)$ in the in-phase-and-quadrature (I-Q) coordinate complex plane. The

received signal model (2.3) can be rewritten as

$$\begin{aligned} r(k) &= |r(k)|e^{j\angle r(k)} \\ &= |r(k)|e^{j(\phi_i(k)+\tilde{\theta}(k)+\epsilon(k))}. \end{aligned} \tag{2.4}$$

referring to Fig. 2.2, where we have

$$\angle r(k) = \phi_i(k) + \tilde{\theta}(k) + \epsilon(k).$$

Here, $|r(k)|$ and $\angle r(k)$ are the received signal amplitude and phase, respectively. In the following, we drop the dependence on time k for simplicity. Term ϵ is the additive observation phase noise due to n, whose statistics is derived later. We denote E_s as the average energy per symbol and $\gamma \triangleq E_s/N_0$ as the average SNR. We express A_i as $A_i = \rho_i\sqrt{E_s}$ where ρ_i is the weight coefficient of the amplitude for the signal point S_i, and we have $M = \sum_{i=0}^{M-1} \rho_i^2$ due to the average energy constraint. We let $\varrho = \tilde{\theta} + \epsilon$ for short.

Now we consider the distribution of PRE $\tilde{\theta}$. There are three popular carrier PE methods. We let $\sigma_{\tilde{\theta}}^2$ represent the variance of $\tilde{\theta}$, which varies with different PE methods. The first one is the PLL tracking method [54]. The PRE $\tilde{\theta}$ introduced by PLL tracking has the Tikhonov pdf [46] [100],

$$p(\tilde{\theta}) = \frac{e^{\alpha\cos\tilde{\theta}}}{2\pi I_0(\alpha)}, \quad |\ \tilde{\theta}\ | < \pi \tag{2.5}$$

where α is the SNR in the loop bandwidth, and $I_0(.)$ is the modified Bessel function of the first kind of order zero. In most cases of practical interest, $\alpha \gg 1$. Hence, (2.5) can be simplified to a Gaussian pdf with $\sigma_{\tilde{\theta}}^2 \triangleq \mathrm{var}[\tilde{\theta}] \approx \alpha^{-1}$:

$$p(\tilde{\theta}) = \frac{1}{\sqrt{2\pi\alpha^{-1}}} e^{-\frac{\tilde{\theta}^2}{2\alpha^{-1}}}. \tag{2.6}$$

Another popular phase tracking method is decision aided maximum likelihood (DA ML) PE [15]. The PRE $\tilde{\theta}$ from imperfect carrier PE is due to the laser phase noise

and a finite SNR. In DA ML PE, $\tilde{\theta}$ is approximately Gaussian distributed with mean zero and variance to be

$$\sigma_{\tilde{\theta}}^2 = \frac{2L^2 + 3L + 1}{6L}\sigma_p^2 + \frac{\sigma_{n'}^2}{2L} \tag{2.7}$$

where L is the averaging memory length, and $\sigma_{n'}^2 = \gamma^{-1}$ [15]. This result for the PRE variance assumes that there are no past decision errors in the DA ML PE. Term σ_p^2 is given by $2\pi T(\Delta v)$ where Δv is the combined transmitter and receiver laser linewidth and T is the symbol duration. The third popular PE method is the Mth-power scheme [35]. Even in this case, the pdf of $\tilde{\theta}$ is approximately Gaussian. Thus, we have $\tilde{\theta} \sim N(0, \sigma_{\tilde{\theta}}^2)$ in the range $[-\pi, \pi)$ for all the three methods, where N denotes the normal (Gaussian) distribution. Note that we do the simulations later in the ideal decision feedback case of DA ML PE, i.e., no past decision errors in the DA ML PE, and thus $\tilde{\theta}$ is generated as a Gaussian distributed random variable with the variance given by $\sigma_{\tilde{\theta}}^2$ above. We only focus on examining the performance of our detectors using the values of $\sigma_{\tilde{\theta}}^2$.

2.1.1 The Additive Observation Phase Noise Model

This section introduces the additive observation phase noise (AOPN) model ϵ in (2.4). The AOPN ϵ is due to the AWGN n, and ϵ ranges in the interval $[-\pi, \pi)$.

First, conditioned on transmitting S_i, the exact joint probability density function (pdf) of $|r|$ and ϵ and the marginal pdf of $|r|$ are well-known and given, respectively, by [101, Chap.4] [102, eqs.(7-8)]

$$p(|r|, \epsilon \mid S_i) = \frac{|r|}{\pi N_0} \exp\left[-\frac{|r|^2 + A_i^2 - 2|r|A_i \cos\epsilon}{N_0}\right] \tag{2.8}$$

and

$$p(|r| \mid S_i) = \frac{|r|}{N_0/2} \exp\left[-\frac{|r|^2 + A_i^2}{N_0}\right] I_0\left(\frac{|r|A_i}{N_0/2}\right). \tag{2.9}$$

Using $p\left(\epsilon \mid |r|, S_i\right) = \frac{p(\epsilon, |r| | S_i)}{p(|r| | S_i)}$, we have

$$p\left(\epsilon \mid |r|, S_i\right) = \frac{\exp\left[\frac{|r|A_i}{N_0/2}\cos\epsilon\right]}{2\pi I_0\left(\frac{|r|A_i}{N_0/2}\right)}, \quad -\pi \leq \epsilon < \pi \tag{2.10}$$

which is a Tikhonov pdf with mean zero, and depends on the transmitted and received signal amplitude, A_i and $|r|$, and the AWGN variance N_0. This result (2.10) offers the statistical model for the AOPN ϵ.

For further error analysis, we need to use this Tikhonov pdf (2.10) to calculate the probability of the event: $\theta_0 \leq \epsilon < \theta_1$, with any transmitted phase ϕ_i, that is,

$$P(\theta_0 \leq \epsilon < \theta_1 \mid |r|, S_i) = \int_{\theta_0}^{\theta_1} p\left(\epsilon \mid |r|, S_i\right) d\epsilon,$$
$$P(\theta_0 \leq \epsilon < \theta_1 \mid S_i) = \int_0^{\infty} P(\theta_0 \leq \epsilon < \theta_1 \mid |r|, S_i) p(|r| \mid S_i) d|r|.$$

However, this result is complex and intractable.

To simplify the analysis, we introduce the asymptotic behavior of the Tikhonov PDF (2.10) under high SNR later, when the Tikhonov pdf can be well approximated by the Gaussian pdf. That is the approximate Gaussian AOPN model.

2.1.2 The Gaussian AOPN+PRE Model

We first introduce the simplified distribution of ϵ, i.e., the approximate Gaussian AOPN model. Then we give the Gaussian AOPN+PRE model.

For high SNR, i.e., $\gamma \gg 1$, we have $|\epsilon| \ll 1$ rad with high probability, and therefore we have: $\cos\epsilon \approx 1 - \frac{1}{2}\epsilon^2$. Since we have: $I_0\left(x\right) \approx \frac{\exp(x)}{\sqrt{2\pi x}}$ for large values of x, the pdf (2.10) thus becomes Gaussian with variance $\frac{N_0}{2|r|A_i}$:

$$p\left(\epsilon \mid |r|, S_i\right) \approx \sqrt{\frac{|r|A_i}{\pi N_0}} \exp\left[-\frac{|r|A_i\epsilon^2}{N_0}\right]. \tag{2.11}$$

Furthermore, for high SNR, we can have $|r| \approx A_i$ for most times. Thus, (2.11)

becomes independent of $|r|$, i.e.,

$$p\left(\epsilon \mid S_i\right) \approx \sqrt{\frac{A_i^2}{\pi N_0}} \exp\left[-\frac{A_i^2 \epsilon^2}{N_0}\right]. \tag{2.12}$$

That is, we have $\epsilon \sim N\left(0, \frac{N_0}{2A_i^2}\right)$, which is the approximate Gaussian AOPN model. The approximate Gaussian phase distribution without conditioning on $|r|$ may have been used by others before, e.g., Proakis [14], but our work leading to eq.(5) establishes this Gaussian AOPN model rigorously.

Since $\tilde{\theta}$ and ϵ are independent for PLL and DA ML, it thus follows that conditioned on S_i transmitted, we have

$$\varrho \sim N(0,\ \frac{N_0}{2A_i^2} + \sigma_{\tilde{\theta}}^2) \tag{2.13}$$

which is the Gaussian AOPN+PRE model in the range $[-\pi, \pi)$.

2.1.3 Constellations Involved

For coherent receivers, MPSK, M-APSK and M-QAM constellations, which are widely used for increased spectral efficiencies, are specifically considered here as transmitted signals for numerical illustration.

MPSK

For MPSK, the transmitted signal $m(k)$ in (2.3) takes on each value from the signal set $\{S_i = \sqrt{E_s} e^{j\frac{2\pi i}{M}},\ i = 0, 1, \ldots, M-1\}$. That is, the signal points are uniformly spaced on one ring whose radius is $\sqrt{E_s}$. As shown in Fig. 2.3, the signal points on each ring form a 4PSK constellation, i.e., quadrature phase shift keying (QPSK).

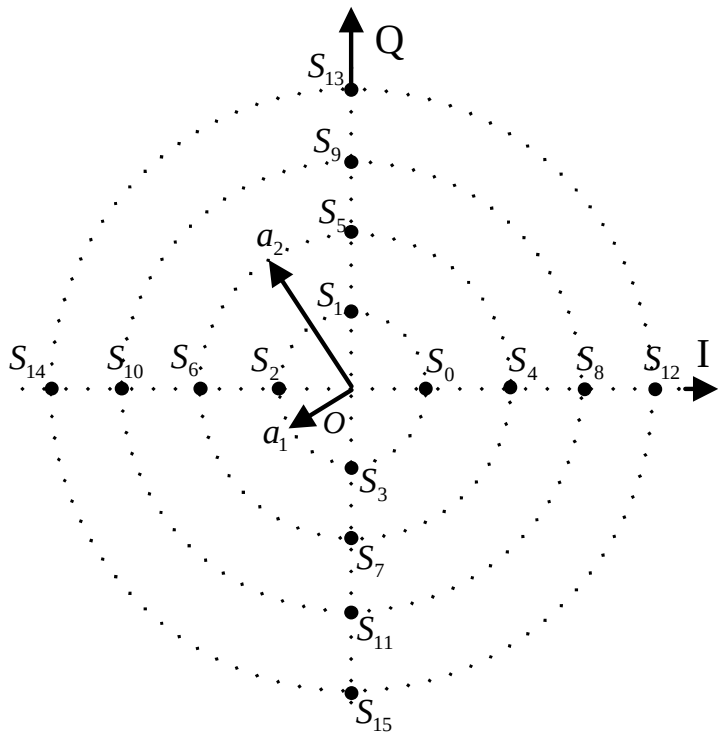

Figure 2.3: (4,4,4,4)-16APSK constellation.

M-APSK

For general M-APSK, the signal set is $\{S_i = a_k e^{j(\frac{2\pi i}{l_k}+\psi_k)} : 1 \leq k \leq N,\ 0 \leq i \leq l_k - 1\}$, where N is the number of amplitude levels or rings, a_k, l_k and ψ_k denote the radius, the number of points and the relative phase shift corresponding to the kth ring, respectively [23]. We have $\sum_{k=1}^{N} l_k = M$ and the radii are assumed to be ordered such that $a_1 < \cdots < a_N$. The average energy constraint is thus $\sum_{k=1}^{N} l_k a_k^2 = ME_s$. We also define the vector $\boldsymbol{l} \equiv (l_1, \cdots, l_N)$ and use the notation $\boldsymbol{l}$-MAPSK for an M-APSK constellation with N rings and l_k signal points on the kth ring, e.g., (4,4,4,4)-16APSK [53], as shown in Fig. 2.3.

M-QAM

For square M-QAM, the signal set is $\{S_i = A_I + jA_Q\}$, where A_I and A_Q are the amplitudes of the in-phase and quadrature components, respectively. And A_I and A_Q are selected independently from the set $\{\pm\frac{d}{2}, \pm\frac{3d}{2}, \ldots, \pm(\sqrt{M}-1)\frac{d}{2}\}$ where

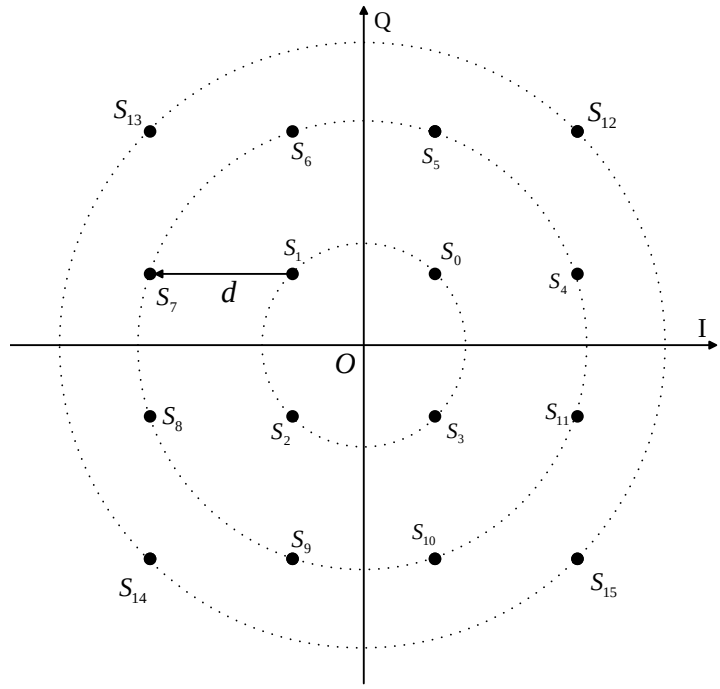

Figure 2.4: 16QAM constellation.

d denotes the Euclidean distance between any two adjacent signal points. We will specifically use $M = 16$ for illustration.

For 16QAM, we have $d = \sqrt{\frac{2E_s}{5}}$ for a given average energy per symbol E_s, as shown in Fig. 2.4. From the 3-ring perspective, the signal set is rewritten as $\{S_i = \frac{d}{\sqrt{2}}e^{j(\frac{\pi i}{2}+\frac{\pi}{4})}$ for $i = 0, 1, 2, 3$; $\frac{\sqrt{10}d}{2}e^{(j[\nu\ \frac{\pi}{2}-\nu\ \frac{\pi}{2}+\nu\ \pi-\nu\ \nu+\pi\ -\frac{3\pi}{2}-\nu\ \nu+\frac{3\pi}{2}\ 2\pi-\nu])}$ with $\nu = \arctan(\frac{1}{3})$ for $i = 4, 5, ..., 11$; and $\frac{3d}{\sqrt{2}}e^{j(\frac{\pi(i-12)}{2}+\frac{\pi}{4})}$ for $i = 12, 13, 14, 15\}$.

2.2 The Amplitude-Phase Form for Differential Detection

In optical fiber systems, differentially modulated signals are also used for transmission, since the receiver is significantly simpler to implement. This is a non-coherent scheme. This section thus introduces the received signal model for differentially detected MDPSK in the presence of AWGN and laser phase noise. The amplitude-phase form necessarily applies to the received signal of MDPSK

with carrier phase noise.

For MDPSK, the kth discrete-time, complex received signal $r(k)$ is modeled as

$$\begin{aligned} r(k) &= \sqrt{E_s} e^{j(\phi(k)+\theta(k))} + n(k) \\ &= |r(k)| e^{j(\phi(k)+\tilde{\varrho}(k))}. \end{aligned} \tag{2.14}$$

Here, $\tilde{\varrho}(k) = \theta(k) + \epsilon(k)$. Term $\theta(k)$ is the laser phase noise, and $\epsilon(k)$ is the AOPN due to AWGN $n(k)$. Based on the random-walk model (2.2) for $\theta(k)$, the residual phase noise (RPN) $\Delta\theta(k)$ is thus zero-mean Gaussian distributed with variance $\sigma_p^2 = 2\pi T \Delta v$. The symbol information is carried in the phase difference between two adjacent received signals, i.e., $\Delta\phi(k) = \phi(k) - \phi(k-1)$. We assume $\Delta\phi(k)$ takes on each value in $\left\{\Delta\phi_l = \frac{2\pi l}{M}\right\}_{l=0}^{M-1}$ with equal probability.

For differential detection, the receiver decides that $\Delta\phi(k) = \frac{2\pi m}{M}$, $m \in \{0, 1, \ldots, M-1\}$, if we have [14]

$$q_m(k) = \max_l \ \{q_l(k) = \Re[r(k) r^\star(k-1) e^{-j\Delta\phi_l}]\}. \tag{2.15}$$

The idea of differential detection is that by forming $r(k)r^\star(k-1) = |r(k)||r(k-1)|e^{j(\Delta\phi(k)+\tilde{\varrho}(k)-\tilde{\varrho}(k-1))}$, $\theta(k)$ is reduced to the RPN $\Delta\theta(k)$. That is, we have

$$\Delta\tilde{\varrho}(k) = \tilde{\varrho}(k) - \tilde{\varrho}(k-1) = \Delta\theta(k) + \epsilon(k) - \epsilon(k-1).$$

Since $\epsilon(k)$ and $\epsilon(k-1)$ are iid, zero-mean, Gaussian random variables with variance $\frac{N_0}{2A_i^2} = \frac{N_0}{2E_s} = 0.5\gamma^{-1}$, $\Delta\tilde{\varrho}(k)$ is also Gaussian distributed over $[-\pi, \pi)$ with mean zero and variance $(\gamma^{-1} + \sigma_p^2)$. That is, we have

$$\Delta\tilde{\varrho}(k) \sim N(0,\ \gamma^{-1} + \sigma_p^2) \tag{2.16}$$

which is the Gaussian AOPN+RPN model. This model provides an easier way to derive the SEP/BEP expressions of differentially detected MDPSK with RPN. In the following, we drop the dependence on time k for simplicity.

2.3 Summary

For coherent detection and differential detection in the phase noise channel, respectively, the specific amplitude-phase-form received signal models are given for following analysis. Based on the the additive observation phase noise model, we will design optimum detector in amplitude-phase form and do performance analysis in phase noise.

Chapter 3

Coherent Detectors for the Phase Noise Channel

For communication channels with time-varying phase, engineers assume perfect phase estimation most times and simply use the minimum Euclidean distance (MED) detector to make decision, as Fig. 3.1(a) shows. However, this way actually leads to a large performance loss, since a noisy phase reference is generally produced due to laser or oscillator phase noise and a finite SNR in phase estimation. Thus, we usually have a phase reference error (PRE) for data detection in most situations. In this chapter, we consider the design of the optimum detector and the approximate ones for any two-dimensional amplitude/phase modulated signals, as shown in Fig. 3.1(b). The received signal is effected by AWGN and a Gaussian distributed PRE due to imperfect carrier phase estimation, which is given by (2.3). We also introduce two suboptimum detectors for memoryless phase noise channels: the MED detector and the annular-sector (AS) detector. Our work here provides a unified view of the relationship between the optimum detector and all the suboptimal ones in the presence of linear phase noise. Numerical results for comparison are presented.

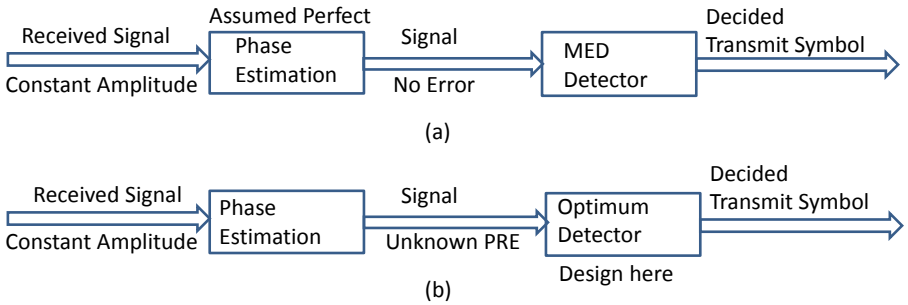

Figure 3.1: Receiver structure in phase noise: (a) in literature; and (b) considered here.

In Section 3.1, the exact MAP/ML detector and the approximate ones in the amplitude-phase form are derived. The approximate ML DB are illustrated on 8-point star QAM in Section 3.2. Section 3.3 provides numerical comparison and parameter mismatch analysis.

3.1 Detectors in Amplitude-Phase Form

In this section, we first propose a unified amplitude-phase-representation approach to derive the maximum *a posterior* probability (MAP)/maximum likelihood (ML) detector for two-dimensional carrier modulations in the presence of AWGN and PRE. It is based on viewing the AWGN as an equivalent phase noise that is described by the additive observation phase noise (AOPN) model that we developed in [91], as introduced in Chap. 2. Now, we will design the MAP/ML (optimum) detector based on $|r|$ and $\angle r$ in the polar coordinates for the received signal model (2.4).

Conventionally, the MAP/ML detector is designed in the rectangular coordinates, where one has $r = \Re[r] + j\Im[r]$ and the likelihood function $p(r \mid S_i) = p(\Re[r], \Im[r] \mid S_i)$. In fact, $p(r \mid S_i)$ can be further evaluated by transforming from rectangular coordinates $(\Re[r], \Im[r])$ to polar coordinates $(|r|, \angle r)$, i.e., one has

$$\begin{aligned} p(r \mid S_i) &= p(|r|, \angle r \mid S_i)\ |r|^{-1} \\ &= p(|r| \mid S_i) p(\angle r \mid |r|, S_i)\ |r|^{-1}. \end{aligned} \tag{3.1}$$

In this way, based on the basic AOPN model proposed in [102], the MAP/ML detector will be derived in the amplitude-phase form, which turns out to be simpler for analysis in phase noise.

First, as mentioned in Section 2.1.1, the exact joint probability density function

(pdf) of $|r|$ and ϵ conditioned on transmitting S_i is given by [101] [102, eq.(7)]

$$p(|r|, \epsilon \mid S_i) = \frac{|r|}{\pi N_0} \exp\left[-\frac{|r|^2 + A_i^2 - 2|r|A_i \cos\epsilon}{N_0}\right] \tag{3.2}$$

Thus, because we have: $\angle r = \phi_i + \tilde{\theta} + \epsilon$, the conditional joint pdf of $|r|$ and $\angle r$ given the signal S_i and the PRE $\tilde{\theta}$ is

$$p(|r|, \angle r \mid \tilde{\theta}, S_i) = \frac{|r|}{\pi N_0} \exp\left[-\frac{|r|^2 + A_i^2 - 2|r|A_i \cos(\angle r - \phi_i - \tilde{\theta})}{N_0}\right] \tag{3.3}$$

Then, given a transmitted symbol S_i, the exact joint pdf of $|r|$ and $\angle r$ is derived as

$$\begin{aligned} p(|r|, \angle r \mid S_i) &= \int_{-\pi}^{\pi} p(|r|, \angle r \mid \tilde{\theta}, S_i) p(\tilde{\theta}) d\tilde{\theta} = \\ &\int_{-\pi}^{\pi} \frac{|r|}{\pi N_0} \exp\left[-\frac{|r|^2 + A_i^2 - 2|r|A_i \cos(\angle r - \phi_i - \tilde{\theta})}{N_0}\right] \times \frac{1}{\sqrt{2\pi\sigma_{\tilde{\theta}}^2}} \exp\left[-\frac{\tilde{\theta}^2}{2\sigma_{\tilde{\theta}}^2}\right] d\tilde{\theta} \end{aligned} \tag{3.4}$$

This joint likelihood function (3.4) leads to the exact MAP decision rule expressed in the amplitude-phase form. We denote $\widehat{S}_{MAP}$ as the optimum decision on the signal m. That is, by using (3.1) in conjunction with (3.4) and factoring out the terms therein which only involve $|r|$, N_0 and $\sigma_{\tilde{\theta}}^2$ and are independent of any signal point in making a decision, we thus have

$$\begin{aligned} \widehat{S}_{MAP} &= \underset{i \in \{0,\ldots,M-1\}}{\arg\max} \; P(r \mid S_i) P(S_i) \\ &= \underset{S_i = A_i e^{j\phi_i}}{\arg\max} \; P(S_i) \times \int_{-\pi}^{\pi} \exp\left[\frac{2|r|A_i \cos(\angle r - \phi_i - \tilde{\theta})}{N_0} - \frac{\tilde{\theta}^2}{2\sigma_{\tilde{\theta}}^2} - \frac{A_i^2}{N_0}\right] d\tilde{\theta}. \end{aligned} \tag{3.5}$$

From now on, we focus on the case of equi-probable transmitted signals, i.e., $P(S_i) = \frac{1}{M}$ for any i, and the MAP detector (3.5) will reduce to the ML detector. Thus the exact ML (optimum) decision rule expressed in the amplitude-phase form

is

$$\begin{aligned}\widehat{S}_{ML} &= \underset{S_i=A_ie^{j\phi_i}}{\arg\max}\ P(|r|, \angle r \mid S_i) \\ &= \underset{\{A_i,\phi_i\}}{\arg\max} \int_{-\pi}^{\pi} \exp\left[\frac{2|r|A_i\cos(\angle r-\phi_i-\tilde{\theta})}{N_0} - \frac{\tilde{\theta}^2}{2\sigma_{\tilde{\theta}}^2} - \frac{A_i^2}{N_0}\right] d\tilde{\theta}. \end{aligned} \tag{3.6}$$

Here, $\widehat{S}_{ML}$ is the optimum decision given by the ML detector.

We can see that (3.6) involves an integral, which is inefficient to implement in real time. To facilitate on-line implementation, we will develop here simple and closed-form approximations from (3.6).

3.1.1 Approximate ML Detectors

To derive simpler and closed-form approximations to the ML detector, we first consider the term: $\cos\epsilon = \cos(\angle r - \phi_i - \tilde{\theta})$, and refer to Fig. 2.2. Since ϵ due to n is approximately Gaussian distributed with mean zero and variance $\frac{N_0}{2A_i^2} = \frac{1}{2\rho_i^2\gamma}$, we consider the high SNR region, i.e., large γ so that ϵ is small at most times. Thus, we can use the approximation: $\cos\epsilon \approx 1 - \frac{\epsilon^2}{2}$, for $\epsilon \ll 1$. Therefore, we have: $\cos(\angle r - \phi_i - \tilde{\theta}) \approx 1 - \frac{(\angle r-\phi_i-\tilde{\theta})^2}{2}$, and (3.4) is simplified to

$$\begin{aligned} p(|r|, \angle r \mid S_i) &= p(|r| \mid S_i)p(\angle r \mid |r|, S_i) \\ &\approx \sqrt{\frac{|r|}{\pi N_0 A_i}} \exp\left[\frac{-(|r|-A_i)^2}{N_0}\right] \times \int_{-\pi}^{\pi} \frac{\exp\left[-\frac{(\angle r-\phi_i-\tilde{\theta})^2}{N_0/(|r|A_i)}\right]}{\sqrt{\pi N_0/(|r|A_i)}} \frac{\exp\left[\frac{-\tilde{\theta}^2}{2\sigma_{\tilde{\theta}}^2}\right]}{\sqrt{2\pi\sigma_{\tilde{\theta}}^2}} d\tilde{\theta} \\ &= \sqrt{\frac{|r|}{\pi N_0 A_i}} \exp\left[\frac{-(|r|-A_i)^2}{N_0}\right] \frac{\exp\left[-\frac{(\angle r-\phi_i)^2}{2(\frac{N_0}{2A_i|r|}+\sigma_{\tilde{\theta}}^2)}\right]}{\sqrt{2\pi(\frac{N_0}{2A_i|r|}+\sigma_{\tilde{\theta}}^2)}} \end{aligned} \tag{3.7}$$

Taking the natural logarithm of both sides of (3.7), we arrive at our first closed-form approximation to the ML decision rule, which makes the decision $\widehat{S}_{aML1}$ as

$$\begin{aligned}\widehat{S}_{aML1} &= \underset{S_i=A_ie^{j\phi_i}}{\arg\max}\ \ln p(|r|, \angle r \mid S_i) \\ &= \underset{\{A_i,\phi_i\}}{\arg\min}\ \frac{(|r|-A_i)^2}{N_0/2} + \frac{(\angle r-\phi_i)^2}{\frac{N_0}{2A_i|r|}+\sigma_{\tilde{\theta}}^2} + \ln\left(\frac{N_0}{2|r|^2}+\frac{A_i}{|r|}\sigma_{\tilde{\theta}}^2\right).\end{aligned} \tag{3.8}$$

Here, $\ln\left(\frac{N_0}{2|r|^2}+\frac{A_i}{|r|}\sigma_{\tilde{\theta}}^2\right)$ can be replaced by $\ln\left(\frac{N_0}{2|r|}+A_i\sigma_{\tilde{\theta}}^2\right)$ because the constant term $|r|$ can be factored out. For any two signal points on the same amplitude level or ring, i.e., that have the same A_i in (3.8), we can see that the decision is only dependent on $(\angle r-\phi_i)^2$ or $|\angle r-\phi_i|$ for choosing the ϕ_i closest to $\angle r$. Hence, the DB are always angular bisectors for the signal points on one ring. It should be noted that although we consider high SNR for the approximation, $\widehat{S}_{aML1}$ is also very accurate in low SNR, as will be shown later. We thus obtain a simpler, approximately optimum detector (3.8), detecting the phase $\angle r$ from the compensated received signal and the ring $|r|$ to make a decision together, which is easy to implement on-line.

The approximate ML detector in (3.8) can be further simplified in two cases. Conditioned on any $S_i = A_ie^{j\phi_i}$ sent, we can have $|r| \approx A_i$ for high SNR, for most times. In this way, replacing $|r|$ with A_i in the second and third items of (3.8) gives the second suboptimum decision $\widehat{S}_{aML2}$ as

$$\widehat{S}_{aML2} = \underset{\{A_i,\phi_i\}}{\arg\min}\ \frac{(|r|-A_i)^2}{N_0/2} + \frac{(\angle r-\phi_i)^2}{\frac{N_0}{2A_i^2}+\sigma_{\tilde{\theta}}^2} + \ln\left(\frac{N_0}{2A_i^2}+\sigma_{\tilde{\theta}}^2\right) \tag{3.9}$$

On the other hand, by replacing A_i with $|r|$ in the second and third items of (3.8), the third suboptimum ML decision $\widehat{S}_{aML3}$ is obtained as

$$\widehat{S}_{aML3} = \underset{\{A_i,\phi_i\}}{\arg\min}\ \frac{(|r|-A_i)^2}{N_0/2} + \frac{(\angle r-\phi_i)^2}{\frac{N_0}{2|r|^2}+\sigma_{\tilde{\theta}}^2} \tag{3.10}$$

since $\ln\left(\frac{N_0}{2|r|^2}+\sigma_{\tilde{\theta}}^2\right)$ does not affect the decision and thus can be ignored.

Our results $\widehat{S}_{ML}$, $\widehat{S}_{aML1}$, $\widehat{S}_{aML2}$ and $\widehat{S}_{aML3}$ in (3.6), (3.8), (3.9) and (3.10)

are derived for all two-dimensional carrier modulations in linear carrier phase noise due to the transmitter and receiver local oscillators. Although (3.9) is also derived in [50, eq.(15)], it is only one special case of our results. Eq. (3.10) has the simplest form. We will show later in simulations that $\widehat{S}_{aML1}$, $\widehat{S}_{aML2}$ and $\widehat{S}_{aML3}$ have almost the same error performance as $\widehat{S}_{ML}$ through the whole SNR region of interest, based on 8-star QAM, rotated 8-star QAM, 16QAM and (4,4,8)-16APSK. Besides, these detectors can lead to the optimal irregular DB.

3.1.2 AS Detector

Here, we introduce a suboptimal detector which performs ring detection and phase detection separately. We call it the annular-sector (AS) detector, since the corresponding decision regions are always annular sectors.

First, for the special case of M-APSK such as 8-star QAM [26] and (4,4,4,4)-16APSK [53] where each ring has the same number of signal points with the same phase values, our suboptimum ML detector $\widehat{S}_{aML3}$ in (3.10) further simplifies to a structure that performs ring detection and phase detection separately. For 8-star QAM, for instance, since the four signal points on the inner ring with radius a_1 have the same phases as those on the outer ring with radius a_2, i.e., $\phi_i \in (0, \frac{\pi}{2}, \pi, \frac{3\pi}{2})$ as Fig. 3.2(a) shows, $\widehat{S}_{aML3}$ in (3.10) can decide on the phase ϕ_i closest to $\angle r$ and on the ring A_i closest to $|r|$ separately. That is, for 8-star QAM, our detector $\widehat{S}_{aML3}$ can be equivalently implemented as follows:

$$
\begin{aligned}
&|r| \underset{\widehat{A}=a_2}{\overset{\widehat{A}=a_1}{\lesseqgtr}} r_{th} = \frac{a_1 + a_2}{2}, \\
&\widehat{\phi} = \underset{\phi_i \in \{\widehat{A}e^{j\phi_i}\}}{\arg\min} \ (\angle r - \phi_i)^2.
\end{aligned} \tag{3.11}
$$

Here, $\widehat{A}$ and $\widehat{\phi}$ denote the suboptimum decisions on A_i and ϕ_i, respectively. Here, we define (3.11) as the AS detector $\widehat{S}_{AS}$ for any two-ring constellations, first making the ring decision $\widehat{A}$, and then detecting ϕ_i restricted to the signal points on that decided ring $\widehat{A}$, i.e., $\phi_i \in \{\widehat{A}e^{j\phi_i}\}$. This AS detector leads to the circular DB in

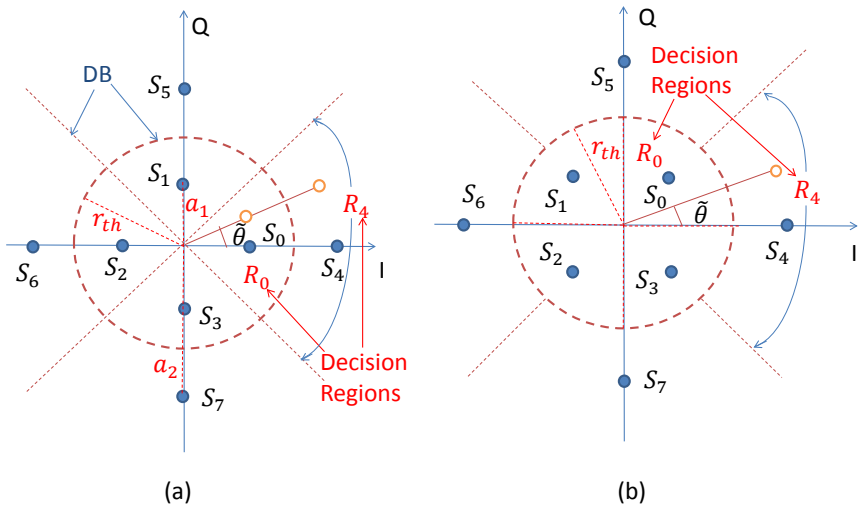

Figure 3.2: 8-point star QAM with PRE $\tilde{\theta}$ and AS decision regions: (a) 8-star QAM; and (b) rotated 8-star QAM.

the middle of two rings and graphically employs a so called annular sector as the decision region for each signal point, as shown in Fig. 3.2. It is shown later that for 8-star QAM and (4,4,4,4)-16APSK, the ML detector (3.6) performs almost the same as this suboptimal detector (3.11) through the whole SNR region for any $\sigma_{\tilde{\theta}}^2$ as expected. In contrast, for rotated 8-star QAM as an example, the $\widehat{S}_{AS}$ in (3.11) is not equivalent to $\widehat{S}_{aML3}$ in (3.10). This is because after deciding on the ϕ_i closest to $\angle r$ for each ring, the decision A_i still depends on all the terms of (3.10), since $\frac{(\angle r-\phi_i)^2}{\frac{N_0}{2|r|^2}+\sigma_{\tilde{\theta}}^2}$ cannot be ignored due to the different ϕ_i values.

However, for any constellation, in the limit as $N_0 \to 0$, i.e., with only phase noise, our suboptimum ML detectors $\widehat{S}_{aML1}$, $\widehat{S}_{aML2}$ and $\widehat{S}_{aML3}$ converge to the AS detector $\widehat{S}_{AS}$. This can be explained from $\widehat{S}_{aML3}$ in (3.10), because for high SNR or $N_0 \to 0$, the term $\frac{(|r|-A_i)^2}{N_0/2}$ has a much larger effect on the decision than the other term, so that we can first detect A_i and then detect ϕ_i on that ring. We will show later via simulations that for other constellations, e.g., rotated 8-star QAM, the $\widehat{S}_{AS}$ is a good approximation to the ML detector only in high SNR or for large $\sigma_{\tilde{\theta}}^2$. Here, $\widehat{S}_{AS}$ employs one-dimensional decisions separately: first in a radius

detector (first stage) whose decision threshold is the arithmetic mean of two adjacent rings' radii, and then in a phase detector (second stage) where we ignore the phase rotation. That is, for any multiple-ring constellations, this suboptimal detector $\widehat{S}_{AS}$ is generally formulated as

$$\begin{aligned} &\frac{a_k + a_{k-1}}{2} \leq |r| < \frac{a_k + a_{k+1}}{2} \Rightarrow \widehat{A} = a_k, \\ &\widehat{\phi} = \underset{\phi_i \in \{\widehat{A}e^{j\phi_i}\}}{\arg\min} \ |\angle r - \phi_i|. \end{aligned} \tag{3.12}$$

Here, a_k denotes the radius of the kth ring, and the radii are assumed to be ordered such that $a_1 < \cdots < a_N$ where N is the number of amplitude levels or rings. We have $a_0 = -a_1$ and $a_{N+1} = \infty$ for the signal points on the innermost and outermost rings, respectively. Here, we define (3.12) as the general AS detector $\widehat{S}_{AS}$ throughout this thesis, first making the ring decision $\widehat{A}$, and then detecting ϕ_i restricted to the signal points on that decided ring $\widehat{A}$, i.e., $\phi_i \in \{\widehat{A}e^{j\phi_i}\}$. This AS detector (3.12) leads to the circular DB in the middle of two rings, and the angular bisector DB for the signal points on one ring.

It should be noted that our results here are for linear phase noise. References [49, 52, 53] have also shown that AS decision regions can result from suboptimal detection in the presence of strong nonlinear phase noise. We will consider the nonlinear phase noise [51, 103] in the future research.

Note that our detectors $\widehat{S}_{ML}$, $\widehat{S}_{aML1}$, $\widehat{S}_{aML2}$ and $\widehat{S}_{aML3}$ require the explicit knowledge of the channel parameters: AWGN spectrum density N_0 and PRE variance $\sigma_{\tilde{\theta}}^2$ for decision. The suboptimum detector $\widehat{S}_{AS}$ does not depend on N_0 and $\sigma_{\tilde{\theta}}^2$. Therefore, in practice when N_0 and $\sigma_{\tilde{\theta}}^2$ may not be known exactly, one may implement $\widehat{S}_{AS}$ in phase noise instead of the ML detector for simplicity. For this reason, one would be interested in how much performance loss $\widehat{S}_{AS}$ has compared with $\widehat{S}_{ML}$ in phase noise. We will show the comparison via simulations later.

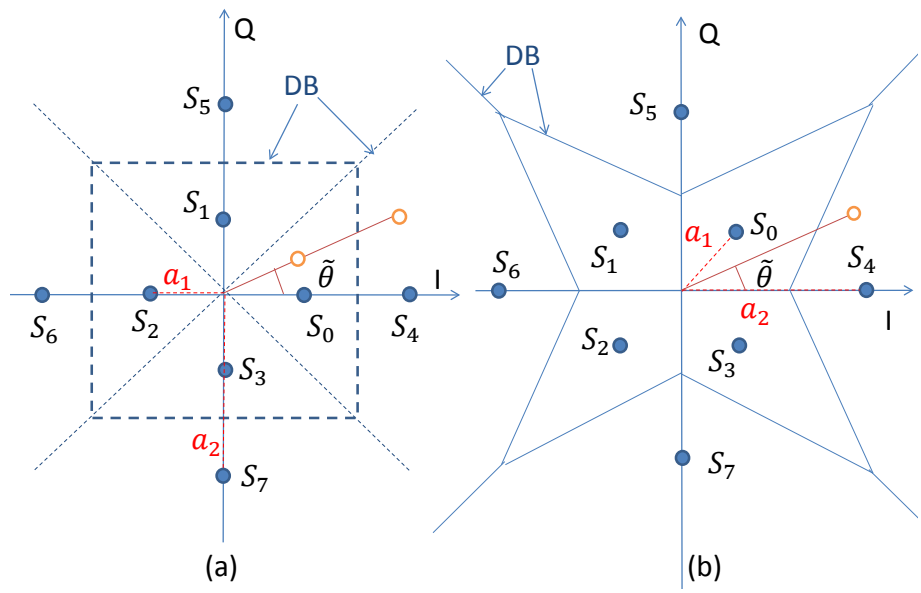

Figure 3.3: 8-point star QAM with PRE $\tilde{\theta}$ and straight-line DB: (a) 8-star QAM; and (b) rotated 8-star QAM.

3.1.3 MED Detector

Another well-known, suboptimal detector is the conventional MED detector which is derived without taking the PRE into account. The MED detector, denoted as $\widehat{S}_{MED}$, is only optimal in pure AWGN and leads to straight-line DB, as shown in Fig. 3.3. Generally, the decision from the MED detector is

$$\widehat{S}_{MED} = \arg\min_{S_i} \|r - S_i\|^2. \tag{3.13}$$

First, for the special case of MPSK which only has one ring of signal points, i.e., $A_i = A$ for all i, the ML (optimal) DB are determined only by $\angle r$. This is because in deciding between any two adjacent symbols $Ae^{j\phi_i}$ and $Ae^{j\phi_{i+1}}$, one should pick ϕ_i if $|\angle r - \phi_i|$ is smaller than $|\angle r - \phi_{i+1}|$ so that the integrand in (3.6) is maximized for any value of $\tilde{\theta}$. Thus, the ML DB are the angular bisectors between the signal points, which are identical to the DB of the MED detector. That is, for MPSK, the ML detector performs always the same as the MED detector for all values of $\sigma^2_{\tilde{\theta}}$.

Furthermore, one should expect that for any constellation, the ML detector (3.6) will reduce to the MED detector $\widehat{S}_{MED}$ in the pure AWGN channel. Since we have $|r|A_i\cos(\angle r-\phi_i-\tilde{\theta})=\Re\left[|r|A_ie^{j(\angle r-\phi_i-\tilde{\theta})}\right]$, (3.6) thus can be rewritten as

$$\widehat{S}_{ML}=\arg\max_{S_i}\int_{-\pi}^{\pi}\exp\left[\frac{2\Re\left[r(S_ie^{j\tilde{\theta}})^*\right]-A_i^2}{N_0}-\frac{\tilde{\theta}^2}{2\sigma_{\tilde{\theta}}^2}\right]d\tilde{\theta}$$

where $*$ denotes the conjugate operator. When no PRE exists, i.e., $\tilde{\theta}=0$, due to the property of exp(.) and integral, $\widehat{S}_{ML}$ above can further reduce to

$$\begin{aligned}\widehat{S}_{ML}|_{\tilde{\theta}=0}&=\arg\max_{S_i=A_ie^{j\phi_i}}\{2\Re\left[r(S_ie^{j\tilde{\theta}})^*\right]-A_i^2\}|_{\tilde{\theta}=0}\\&=\arg\max_{S_i}2\Re\left[rS_i^*\right]-A_i^2\\&=\widehat{S}_{MED}.\end{aligned}\tag{3.14}$$

That is, if the PRE $\tilde{\theta}$ is known to be 0, the only contribution in (3.6) would come from $2|r|A_i\cos(\angle r-\phi_i)-A_i^2$, which then reduces (3.6) to $\widehat{S}_{MED}$ in (3.13).

The suboptimum detector $\widehat{S}_{MED}$ in (3.13) also does not require the information of N_0 and $\sigma_{\tilde{\theta}}^2$ for detection. Therefore, in practical implementation when N_0 and $\sigma_{\tilde{\theta}}^2$ may not be known exactly, one would wonder whether $\widehat{S}_{MED}$ or $\widehat{S}_{AS}$ should be employed instead of the ML detector. Thus, we will compare their SEP performance to show the transition relationship later.

3.2 The ML DB for 8-point Star QAM

In this section, we will first introduce 8-point star QAM which includes 8-star QAM and rotated 8-star QAM. Then using our approximate ML detectors, we illustrate the irregular DB for these formats.

Figs. 3.3(a) and 3.3(b) give the constellation maps of 8-star QAM and rotated 8-star QAM, respectively. Here, a_1 and a_2 are the radii of the inner ring and the

outer ring, respectively. For 8-star QAM, the signal set $\{S_i\}$ with $M = 8$ is $\{A_i e^{j\phi_i} = a_1 e^{j(\frac{\pi i}{2})}$ for $i = 0, 1, 2, 3$ and $a_2 e^{j(\frac{\pi(i-4)}{2})}$ for $i = 4, 5, 6, 7\}$. For rotated 8-star QAM, the points on the inner ring have a 45° phase offset compared with the points on the outer ring, i.e., $\{A_i e^{j\phi_i} = a_1 e^{j(\frac{\pi i}{2}+\frac{\pi}{4})}$ for $i = 0, 1, 2, 3$ and $a_2 e^{j(\frac{\pi(i-4)}{2})}$ for $i = 4, 5, 6, 7\}$. Here, we assume $a_1 = \alpha\sqrt{E_s}$ and $a_2 = \beta\alpha\sqrt{E_s}$, where α is the coefficient of the inner ring and $\beta = a_2/a_1$ is the ring ratio. Since the mean of energies of the inner ring and outer ring should be E_s, we have

$$\frac{\alpha^2(\beta^2+1)}{2} = 1, \quad \beta > 1 \text{ and } 0 < \alpha < 1. \tag{3.15}$$

In the following, we fix β for both 8-point star QAM constellations. We set $\beta = 2.4$ in 8-star QAM and $\beta = 2$ in the rotated one throughout this chapter, which are the optimal values of β within a large range of γ (from about 8dB to about 30dB) for minimum SEP of the corresponding constellation in pure AWGN. These can be easily checked by the exact SEP expressions (4.35) and (4.36) derived for the pure AWGN channel in Chap. 4 Appendix. As an example, for 8-star QAM with $\beta = 2.4$, we have $\alpha = 0.54$, $r_1 = 0.54\sqrt{E_s}$, $r_2 = 1.3\sqrt{E_s}$ and the radius of circular DB is $r_{th} = \frac{r_1+r_2}{2} = 0.92\sqrt{E_s}$.

By using our approximate ML detector $\widehat{S}_{aML2}$ in (3.9), we can get the approximately optimal DB as a function of SNR γ and PRE variance $\sigma_{\tilde{\theta}}^2$ in phase noise. For instance, the DB between S_0 and S_4 for rotated 8-star QAM is given by

$$P(|r|, \angle r \big| S_0) \underset{S_4}{\overset{S_0}{\gtrless}} P(|r|, \angle r \big| S_4),$$

which leads to

$$\begin{aligned} |r| \underset{S_4}{\overset{S_0}{\lessgtr}} & \frac{a_1+a_2}{2} + \frac{N_0}{4(a_2-a_1)} \ln \frac{\sigma_{\tilde{\theta}}^2 + \frac{N_0}{2a_2^2}}{\sigma_{\tilde{\theta}}^2 + \frac{N_0}{2a_1^2}} \\ & + \frac{N_0}{4(a_2-a_1)} \left(\frac{\angle r^2}{\sigma_{\tilde{\theta}}^2 + \frac{N_0}{2a_2^2}} - \frac{(\angle r - \frac{\pi}{4})^2}{\sigma_{\tilde{\theta}}^2 + \frac{N_0}{2a_1^2}} \right) \end{aligned} \tag{3.16}$$

since we have $\phi_0 = \frac{\pi}{4}$ and $\phi_4 = 0$. Fig. 4.1 shows the DB of rotated 8-star QAM given by our detector $\widehat{S}_{aML2}$ under different parameters. The DB given by our $\widehat{S}_{aML3}$ are almost identical to those of $\widehat{S}_{aML2}$. We show that the DB between the two rings varies with γ and $\sigma^2_{\tilde{\theta}}$, while the DB between any two signal points on the same ring are always angular bisectors. For low SNR or for weak phase noise, the AWGN dominates. Therefore, the DB for small γ or $\sigma^2_{\tilde{\theta}}$ are asymptotically straight-line, approaching to those of AWGN-limited case, i.e., $\sigma^2_{\tilde{\theta}} = 0$ in Fig. 4.1. Otherwise, we can see that the DB for large phase noise or high SNR are asymptotically circular between rings, since phase noise dominates for both cases. It can be seen that (3.16) can be simplified to $|r| \underset{S_4}{\overset{S_0}{\lessgtr}} \frac{a_1+a_2}{2}$ when $\sigma^2_{\tilde{\theta}} \gg \frac{N_0}{2a_1^2}$ or $N_0 \to 0$. This implies that for larger γ or $\sigma^2_{\tilde{\theta}}$, the ML detector can be replaced by the $\widehat{S}_{AS}$ in (3.12) in practice. Reference [104] has also suggested that circular DB between rings are optimal for 8-point star QAM in the phase-noise-limited case where $N_0 \to 0$. We check by multiple plots that the DB between rings becomes almost circular when γ is about $10\sigma^{-2}_{\tilde{\theta}}$ or above, which just corresponds to the above fact of $\sigma^2_{\tilde{\theta}} \gg \frac{N_0}{2a_1^2}$.

For 8-star QAM, the DB of our $\widehat{S}_{aML2}$ exhibits the same trend as that of rotated 8-star QAM, and Fig. 3.5 shows the changing DB with varying $\sigma^2_{\tilde{\theta}}$ and γ, respectively. However, the DB of our suboptimum detector $\widehat{S}_{aML3}$ for 8-star QAM is always circular in the middle irrespective of γ and $\sigma^2_{\tilde{\theta}}$, due to the equivalence to $\widehat{S}_{AS}$ in (3.11).

In nonlinear phase noise, [105] obtained the (nonlinear) optimal DB by applying the expectation maximization algorithm to compensate for the distortion and phase shift on the constellations. We will consider this nonlinear case in future work.

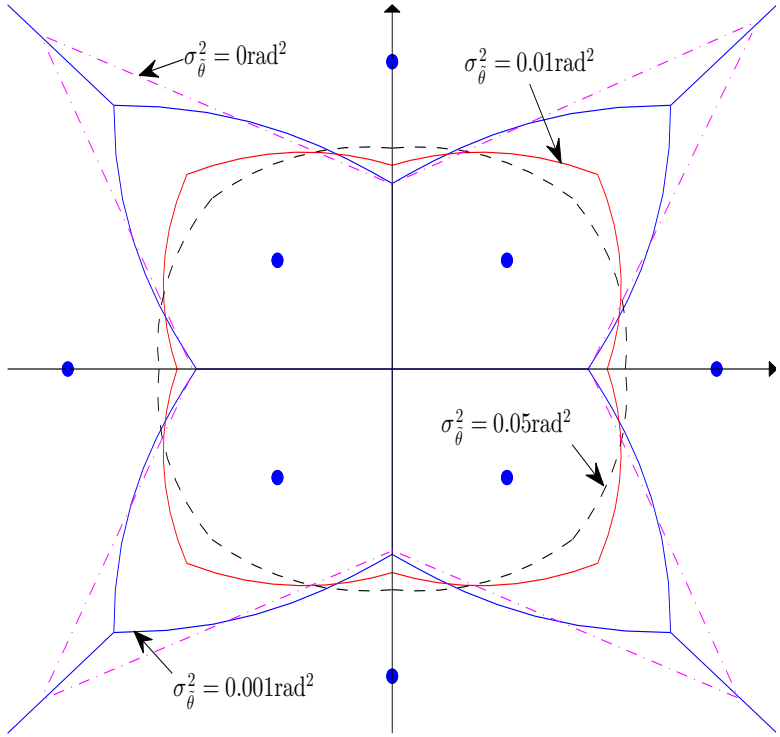

(a)

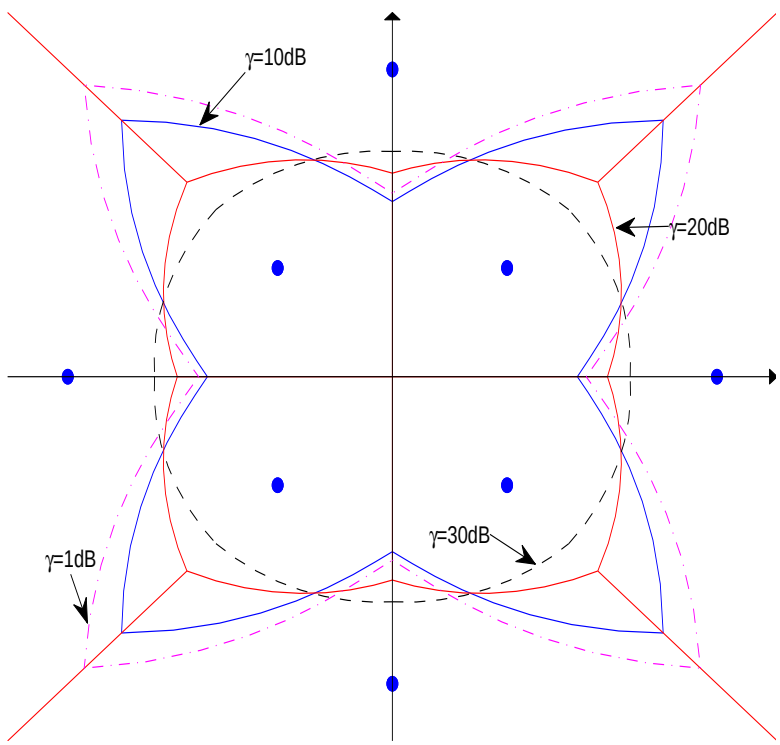

(b)

Figure 3.4: DB of our detector $\widehat{S}_{aML2}$ (or $\widehat{S}_{aML3}$) for rotated 8-star QAM with $\beta = 2$: (a) varying $\sigma^2_{\tilde{\theta}}$ with $\gamma = 20$dB; and (b) varying γ with $\sigma^2_{\tilde{\theta}} = 0.01\text{rad}^2$.

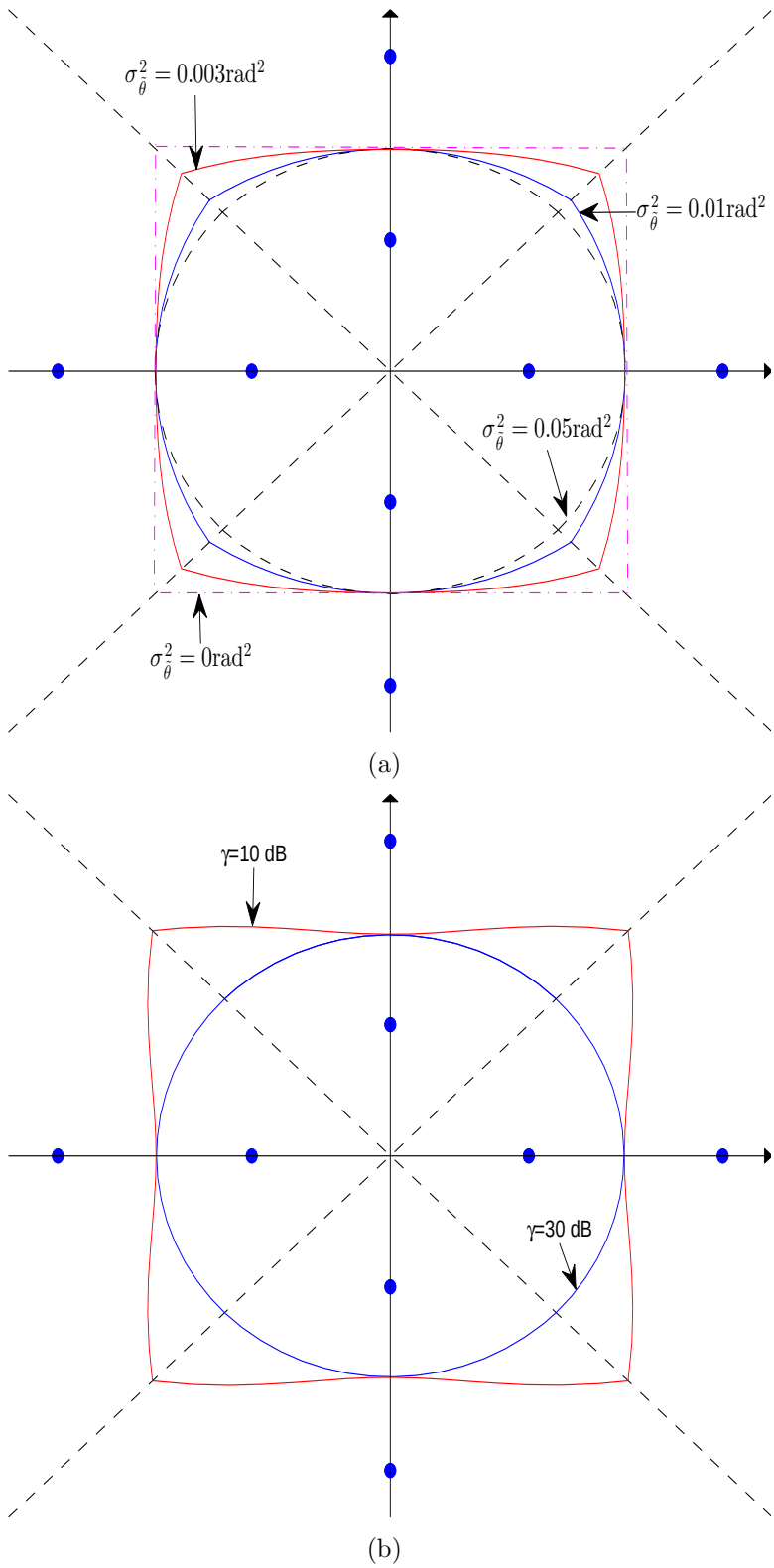

Figure 3.5: DB of our detector $\widehat{S}_{aML2}$ for 8-star QAM with $\beta = 2.4$: (a) varying $\sigma^2_{\tilde{\theta}}$ with $\gamma = 20\text{dB}$; and (b) varying γ with $\sigma^2_{\tilde{\theta}} = 0.01\text{rad}^2$.

3.3 Numerical Results

We will use Monte Carlo simulation to get the SEP results for the MED detector (3.13), the AS detector (3.12), and all the exact and approximate ML detectors in phase noise with different PRE variances $\sigma_{\tilde{\theta}}^2$. Here, we generate $\tilde{\theta}$ as a Gaussian distributed random variable with the variance given by

$$\sigma_{\tilde{\theta}}^2 = \frac{2L^2 + 3L + 1}{6L}\sigma_p^2 + \frac{1}{2\gamma L}. \tag{3.17}$$

This thus corresponds to the simulations in the ideal decision feedback case, i.e., no past decision errors in the DA ML PE, which is used only for examining the performance of our detectors.

As discussed in [15], an optimal memory length L which gives the minimum value of $\sigma_{\tilde{\theta}}^2$ can be derived from (3.17), that is [15, eq. (17)]

$$L_{opt} = \left\lfloor \frac{1}{4}\sqrt{1 + \frac{24}{\gamma\sigma_p^2}} - \frac{3}{4} \right\rfloor.$$

Here, $\lfloor x \rfloor$ denotes the largest integer less than or equal to x. It is shown in [15] that DA ML with L_{opt} always leads to a minimum PRE variance, thus resulting in the optimal error performance. We can see that the choice of L_{opt} depends on the knowledge of γ and σ_p^2, which requires a series of accurate estimation. For simple illustration, we do not consider L_{opt} here. To keep the accuracy of DA ML PE in the SNR region of interest, we set $L = 8$ for 8-point star QAM, and for 16-point constellations, we use $L = 12$ throughout the simulations, as mentioned in [15]. Note that a longer memory interval L will lead to less tolerance to the combined normalized laser linewidth $\sigma_p^2 = 2\pi(\Delta v)T$ for a given SEP performance of DA ML.

Here, 8-star QAM, rotated 8-star QAM, 16QAM and (4,4,8)-16APSK are used as examples for numerical illustration. Figs. 3.3 and 2.4 give the constellation maps of 8-point star QAM and 16QAM, respectively. The (4,4,8)-16APSK constellation with uniformly-spaced ring radii, i.e., $\{S_i = \frac{\bar{d}}{2}e^{j(\frac{\pi i}{2}+\frac{\pi}{4})}$ for $i = 0, 1, 2, 3$; $\bar{d}e^{j(\frac{\pi(i-4)}{2}+\frac{\pi}{4})}$

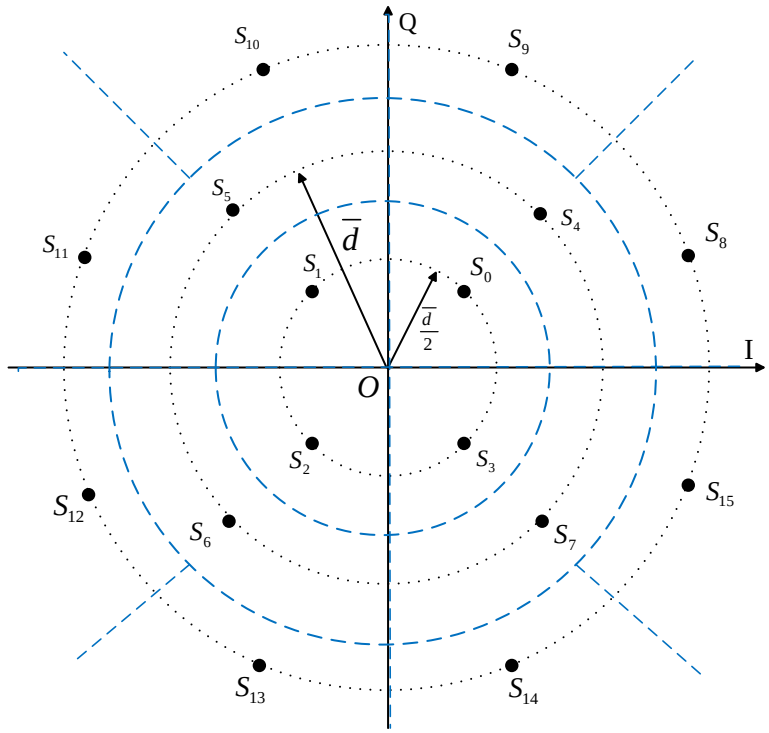

Figure 3.6: (4,4,8)-16APSK with AS decision regions.

for $i = 4, 5, 6, 7$; and $\frac{3\bar{d}}{2}e^{j(\frac{\pi(i-8)}{4}+\frac{\pi}{8})}$ for $i = 8, 9...15\}$ with $\bar{d} = \sqrt{\frac{16E_s}{23}}$, is shown in Fig. 3.6. We introduce this 3-ring 16APSK to compare with the widely used 16QAM, which can also be regarded as a 3-ring constellation, i.e., (4,8,4)-16QAM, as shown in Fig. 2.4. It should be noted in simulations that we make $\angle r$ in the range $[0, 2\pi)$. And for 8-star QAM, we need consider two more cases $\{A_i = a_1, \phi_i = 2\pi\}$ and $\{A_i = a_2, \phi_i = 2\pi\}$ to find the minimum, since (3.8), (3.9 and (3.10) include $(\angle r - \phi_i)^2$. If $\{A_i = a_1, \phi_i = 2\pi\}$ makes the minimum, we decide that S_0 is sent. If $\{A_i = a_2, \phi_i = 2\pi\}$ leads to the minimum, S_4 is decided. For (3.6), however, we do not need to consider these cases because of the cos(.) inside. Similarly, for rotated 8-star QAM, we only add the case of $\{A_i = a_2, \phi_i = 2\pi\}$ for the outer ring, since $\phi_i \neq 0$ on the inner ring. We decide that S_4 is sent when $\{A_i = a_2, \phi_i = 2\pi\}$ results in the minimum value.

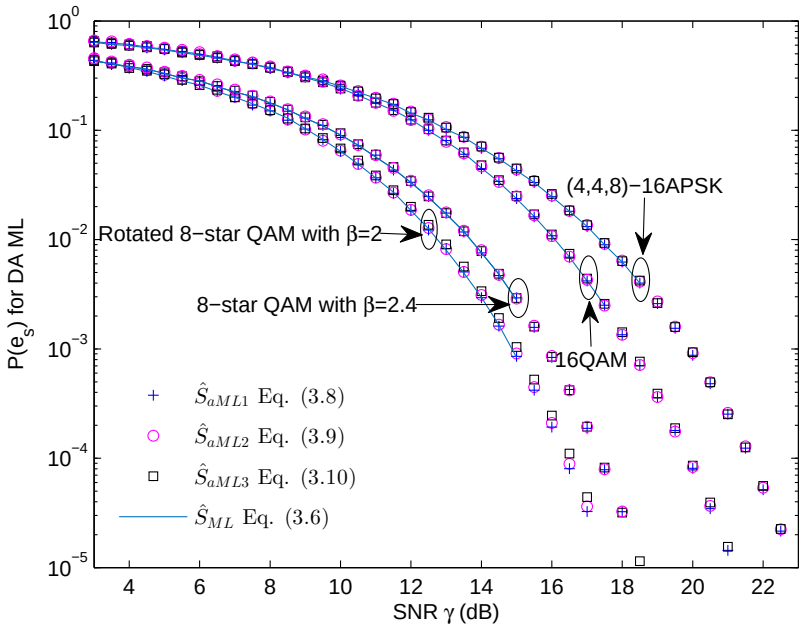

(a)

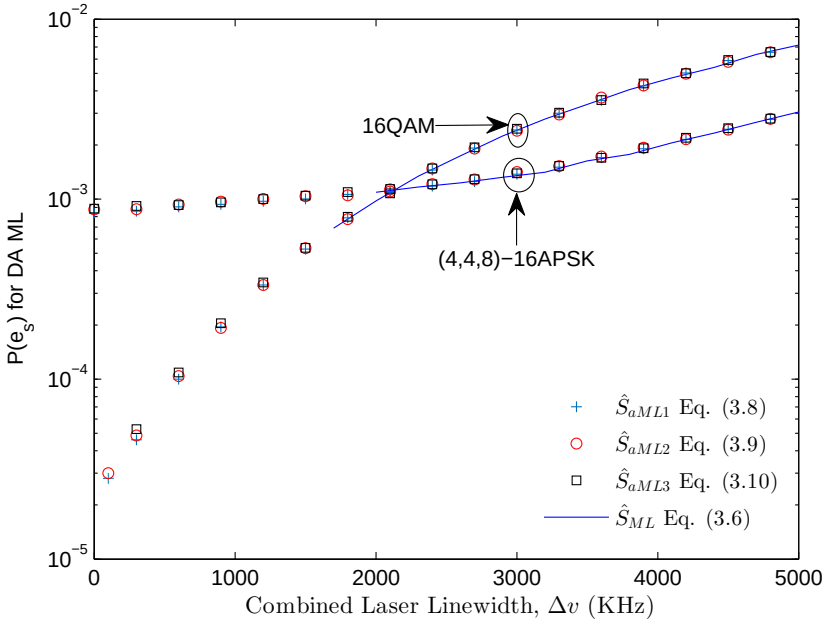

(b)

Figure 3.7: Performance comparison of $\widehat{S}_{ML}$, $\widehat{S}_{aML1}$, $\widehat{S}_{aML2}$ and $\widehat{S}_{aML3}$ for DA ML PE at a data rate of 40Gbit/s: (a) as SNR γ increases; and (b) as combined laser linewidth Δv increases with fixed $\gamma = 20$dB.

3.3.1 Comparison among $\widehat{S}_{ML}$, $\widehat{S}_{aML1}$, $\widehat{S}_{aML2}$ and $\widehat{S}_{aML3}$

In Fig. 3.7(a), σ_p^2 (rad^2) is set to be $4.5\pi \times 10^{-4}$ and $\pi \times 10^{-4}$ for 8-point star QAM and 16-point constellations, respectively, which corresponds to 3MHz and 500KHz of combined laser linewidth (Δv) at a data rate of 40Gbit/s [15]. In Fig. 3.7(b), Δv increases from 0KHz to 5MHz, at a data rate of 40Gbit/s for a given $\gamma = 20$dB. As Fig. 3.7 shows, the approximate ML detectors we derived have almost the same error performance as the exact ML detector $\widehat{S}_{ML}$ through the whole SNR region of interest for any Δv. Although we assume high SNR in the derivations, our detectors also work very well in low SNR down to 3dB. It should be noted that $\widehat{S}_{ML}$ in (3.6) is very computationally inefficient. Therefore, in practical implementation, one can implement any of our approximate ML detectors $\widehat{S}_{aML1}$, $\widehat{S}_{aML2}$ and $\widehat{S}_{aML3}$ instead of $\widehat{S}_{ML}$ for efficiency. To keep the accuracy and to reduce the computational load, our first approximate ML detector $\widehat{S}_{aML1}$ in (3.8) is used instead of $\widehat{S}_{ML}$ in the following simulation for the SEP of the ML detector. Moreover, Fig. 3.7(b) shows that (4,4,8)-16APSK is much less sensitive to increased Δv than 16QAM.

3.3.2 Comparison between $\widehat{S}_{aML1}$ and $\widehat{S}_{AS}$

As Fig. 3.8 and Fig. 3.9(a) show, for low SNR, our $\widehat{S}_{aML1}$ in (3.8) always performs better than $\widehat{S}_{AS}$. As γ increases for a given $\sigma_{\tilde{\theta}}^2$ or σ_p^2 (or $(\Delta v)T$), or as $\sigma_{\tilde{\theta}}^2$ or σ_p^2 increases for a fixed γ, the performance of $\widehat{S}_{AS}$ asymptotically approaches that of $\widehat{S}_{aML1}$. This phenomenon corresponds to the geometrical fact in Fig. 4.1 that the approximate ML decision region for each signal point asymptotically becomes an annular sector as $\sigma_{\tilde{\theta}}^2$ or γ increases. This implies that for larger $\sigma_{\tilde{\theta}}^2$ or γ, $\widehat{S}_{AS}$ can replace $\widehat{S}_{aML1}$ for simpler implementation. For rotated 8-star QAM as an example, Fig. 3.8(a) shows that for $\sigma_{\tilde{\theta}}^2 = 0.02$rad^2, the SNR penalty of $\widehat{S}_{AS}$ compared to $\widehat{S}_{aML1}$ is about 1dB at the SEP value of 10^{-3} of practical interest. As γ increases, the performance loss becomes smaller and smaller. For 16QAM with $\gamma = 28$dB in Fig. 3.9(a), we see that $\widehat{S}_{AS}$ has almost the same laser linewidth tolerance as $\widehat{S}_{ML}$.

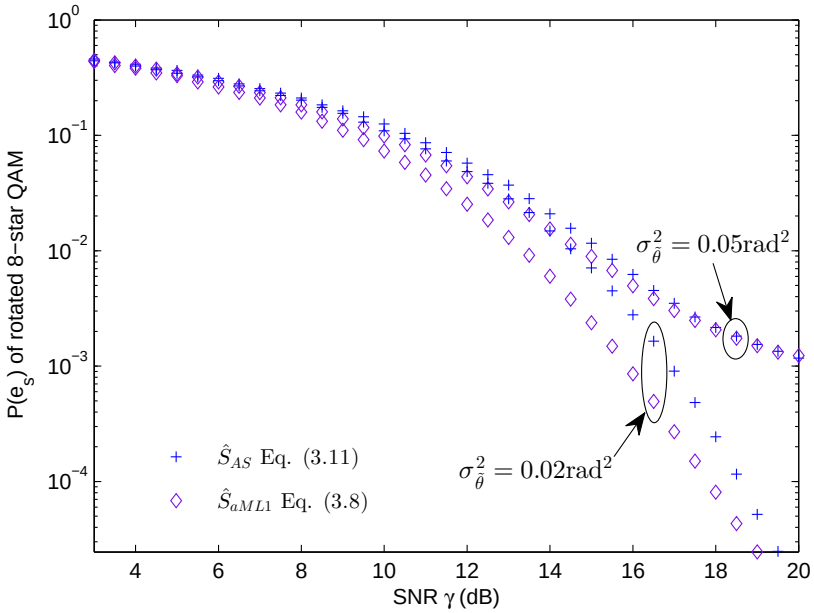

(a)

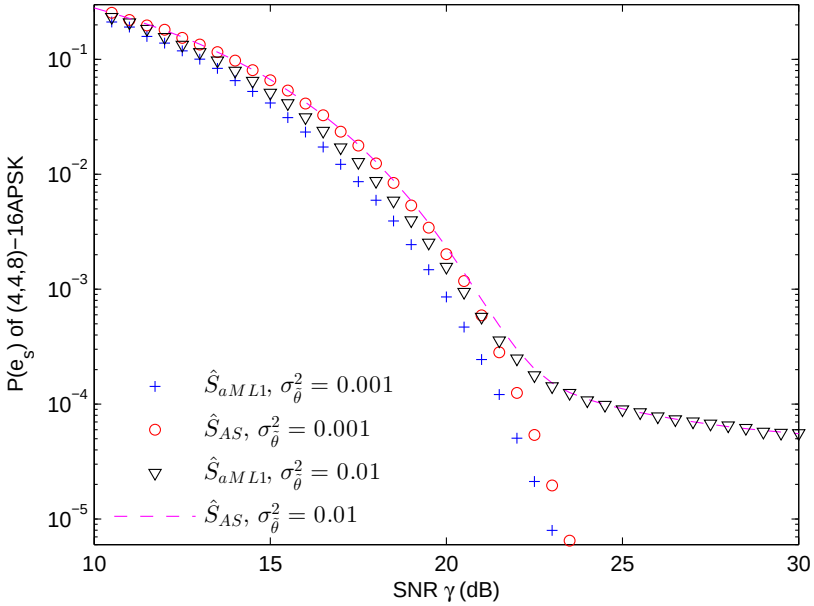

(b)

Figure 3.8: SEP comparison between $\widehat{S}_{aML1}$ and $\widehat{S}_{AS}$: (a) rotated 8-star QAM with $\beta = 2$; and (b) (4,4,8)-16APSK.

For 8-star QAM, Fig. 3.9(b) shows that the performance of $\widehat{S}_{AS}$ agrees with that of $\widehat{S}_{aML1}$ for any γ with $\sigma_p^2(\text{rad}^2)$ ranging from 0 to 10^{-2}, since $\widehat{S}_{aML1}$ and $\widehat{S}_{AS}$ are identical as shown earlier. Thus, our result (4.31) is also an accurate approximation to the SEP of $\widehat{S}_{ML}$ for 8-star QAM with any Δv. The same observation will hold for (4,4,4,4)-16APSK.

3.3.3 Comparison between $\widehat{S}_{aML1}$ and $\widehat{S}_{MED}$

For practical application with DA ML PE, Fig. 3.10 shows the SEP comparison between $\widehat{S}_{aML1}$ and $\widehat{S}_{MED}$ with increasing laser linewidth Δv at a data rate of 40Gbit/s. We give rotated 8-star QAM and 16-point constellations as examples, where we fix γ to be 15dB and 20dB, respectively. The SEP increases as Δv increases from 0KHz to 5MHz. As expected, $\widehat{S}_{aML1}$ performs much better than $\widehat{S}_{MED}$, especially for higher-order modulations. For a given SEP value of 10^{-2} or lower, $\widehat{S}_{aML1}$ is shown to have a much larger laser linewidth tolerance than $\widehat{S}_{MED}$. Moreover, we can see that 16QAM is much more sensitive to increased Δv than (4,4,8)-16APSK.

3.3.4 Comparison between $\widehat{S}_{AS}$ and $\widehat{S}_{MED}$

The detector $\widehat{S}_{MED}$ is optimal in pure AWGN, whereas $\widehat{S}_{AS}$ is asymptotically optimal as $\sigma_{\tilde{\theta}}^2$ or γ increases in phase noise. Both $\widehat{S}_{MED}$ and $\widehat{S}_{AS}$ are simple and do not need the information of $\sigma_{\tilde{\theta}}^2$ and N_0 for practical implementation. Thus, we compare their SEP performance here to show the transition from one to the other. As Fig. 3.11 shows, for small γ, $\widehat{S}_{MED}$ outperforms $\widehat{S}_{AS}$, conforming the fact that the optimal DB are approximately straight lines when AWGN still dominates. As γ increases, the SEP of $\widehat{S}_{MED}$ deteriorates much faster than that of $\widehat{S}_{AS}$. More importantly, we can see that $\widehat{S}_{AS}$ is much more robust to phase noise than $\widehat{S}_{MED}$ in the reasonably high SNR region corresponding to the SEP values of 10^{-3} and lower which are of practical interest. In addition, $\widehat{S}_{MED}$ leads to a much larger error floor than $\widehat{S}_{AS}$. As Fig. 3.12 shows for DA ML PE, $\widehat{S}_{AS}$ performs better than

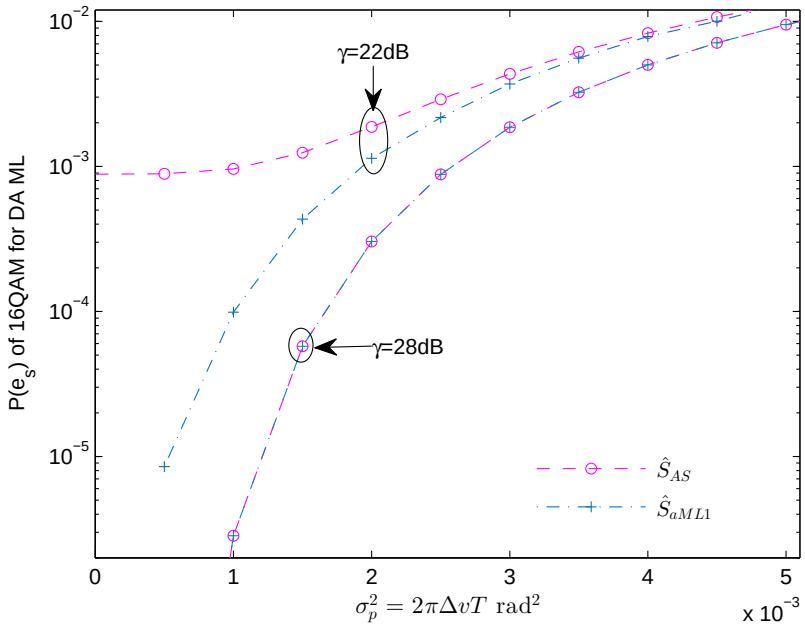

(a)

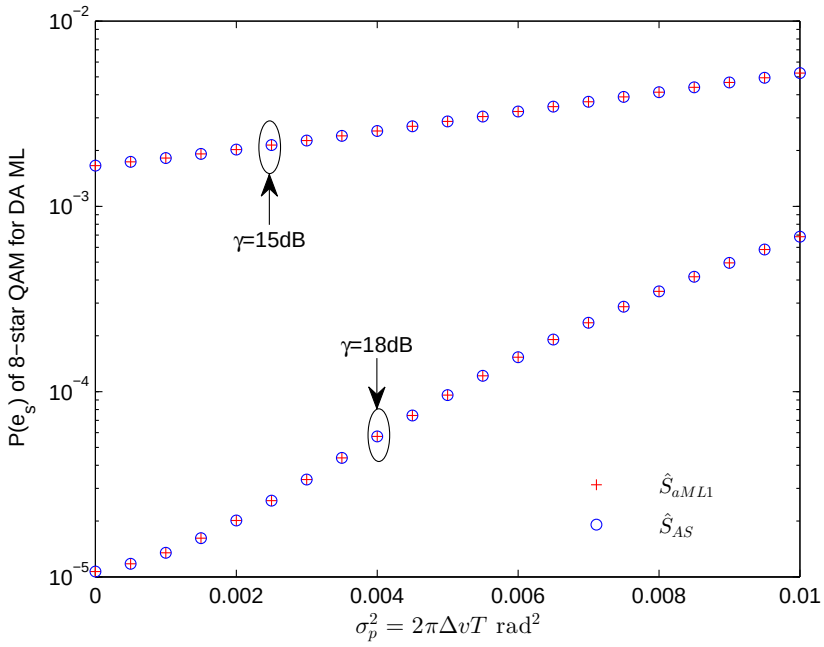

(b)

Figure 3.9: SEP comparison between $\widehat{S}_{aML1}$ and $\widehat{S}_{AS}$ for DA ML PE: (a) 16QAM with $L = 12$; and (b) 8-star QAM with $\beta = 2.4$ and $L = 8$.

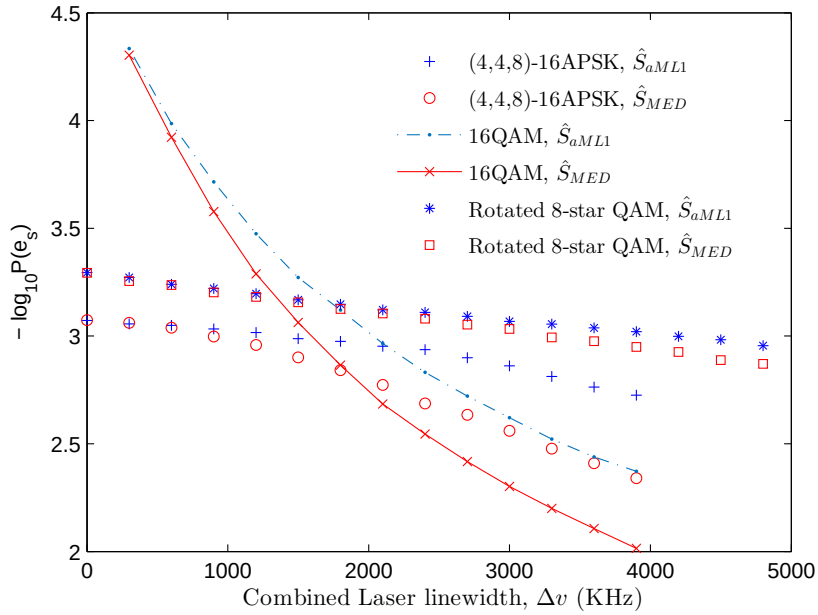

Figure 3.10: SEP comparison as a function of combined laser linewidth Δv between $\widehat{S}_{aML1}$ and $\widehat{S}_{MED}$.

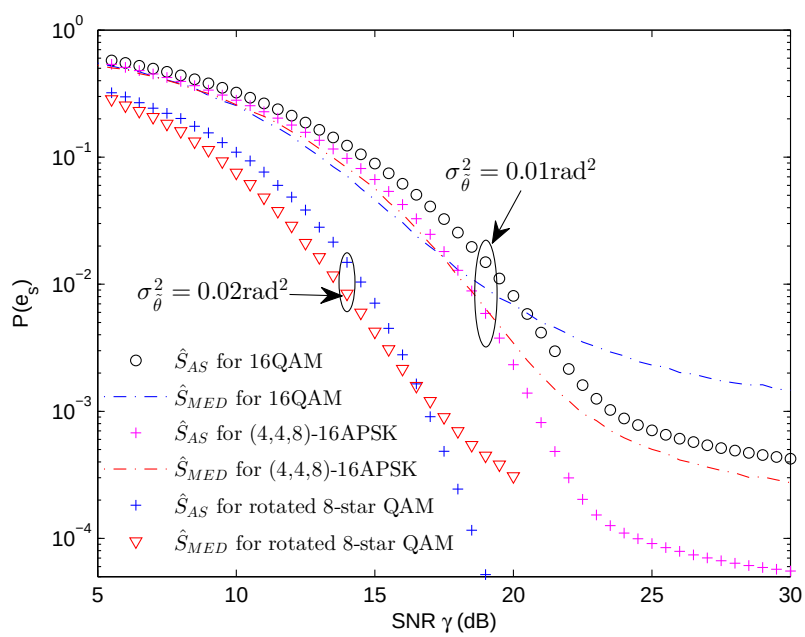

Figure 3.11: SEP comparison between $\widehat{S}_{AS}$ and $\widehat{S}_{MED}$ for rotated 8-star QAM ($\beta = 2$) with $\sigma_{\tilde{\theta}}^2 = 0.02\text{rad}^2$ and 16-point constellations with $\sigma_{\tilde{\theta}}^2 = 0.01\text{rad}^2$.

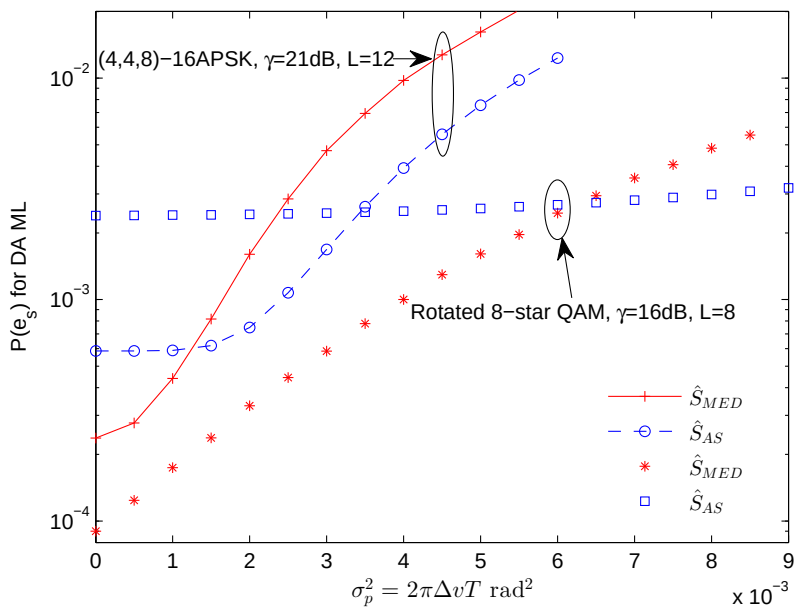

Figure 3.12: SEP comparison between $\widehat{S}_{AS}$ and $\widehat{S}_{MED}$ for DA ML PE as $\sigma_p^2 = 2\pi(\Delta v)T$ increases.

$\widehat{S}_{MED}$ for larger σ_p^2, and thus is much more robust to increased $(\Delta v)T$. The superior performance of $\widehat{S}_{AS}$ can be traced to the geometrical fact in Fig. 3.4(a) that the circular DB shape provides the signal points with more angular distances from the boundaries, and thus more phase-noise-tolerance than the straight-line DB does.

For 8-star QAM, Fig. 3.13 shows that the performance of $\widehat{S}_{AS}$ hardly differs from that of $\widehat{S}_{MED}$ for any σ_p^2 through the whole SNR region. This echoes the geometrical fact in Fig. 3.5 that the changed decision regions or angular distances are small and thus hardly have effect on the performance. Thus, our result (4.31) is also a good approximation to the SEP of $\widehat{S}_{MED}$ for 8-star QAM.

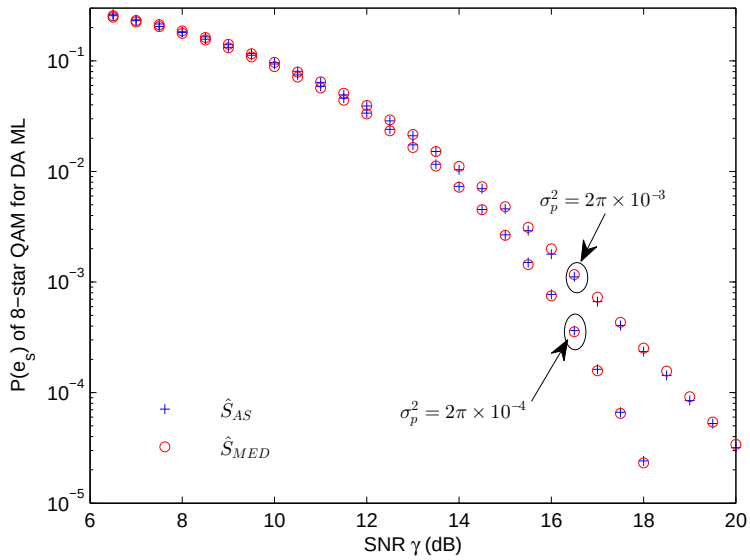

Figure 3.13: SEP comparison between $\widehat{S}_{AS}$ and $\widehat{S}_{MED}$ for 8-star QAM with DA ML PE, $L = 8$.

3.3.5 Parameter Mismatch Analysis

Both the suboptimal MED and AS detectors do not need to know the values of N_0 and $\sigma_{\tilde{\theta}}^2$ for detection. However, our detectors in (3.6), (3.8), (3.9) and (3.10) require the exact information of N_0 and $\sigma_{\tilde{\theta}}^2$ for accurate detection. Therefore, in this subsection, we will show how the mismatch of N_0 and $\sigma_{\tilde{\theta}}^2$ in ML detection affects the system performance. Here, we assume the transmission environment with $N_0 = 1$ and $\sigma_{\tilde{\theta}}^2 = 0.01\text{rad}^2$. We give two mismatched cases: (I, $N_0 = \frac{2}{3}, \sigma_{\tilde{\theta}}^2 = 0.02$) and (II, $N_0 = \frac{1}{2}, \sigma_{\tilde{\theta}}^2 = 0.05$) for numerical comparison of 8-point star QAM. First, for 8-star QAM, since $\widehat{S}_{AS}$ does not depend on N_0 and $\sigma_{\tilde{\theta}}^2$, the error performance of the approximate ML detectors should thus be insensitive to the mismatch, as Fig. 3.14(a) illustrates. However, as Fig. 3.14(b) shows, the mismatch with the practical N_0 and $\sigma_{\tilde{\theta}}^2$ leads to a poor error performance for rotated 8-star QAM. Moreover, the two mismatched cases as examples are (I, $N_0 = 1, \sigma_{\tilde{\theta}}^2 = 0.05$) and (II, $N_0 = \frac{1}{2}, \sigma_{\tilde{\theta}}^2 = 0.05$) for 16-point constellations. As Fig. 3.15(a) shows for 16QAM, although the mismatch increases the SEP in the medium SNR region, it makes no

difference in high SNR region corresponding to the SEP values of 10^{-3} and lower, when $\widehat{S}_{AS}$ approaches $\widehat{S}_{ML}$ as Fig. 3.9(a) shows. More importantly, we can see from Fig. 3.15(b) that (4,4,8)-16APSK is very resistant to the mismatch, since $\widehat{S}_{AS}$ can be almost equivalently applied instead of $\widehat{S}_{ML}$ according to Fig. 3.8(b).

3.4 Concluding Remarks

Our AOPN model provides a unified approach for MAP/ML receiver design in amplitude-phase form for two-dimensional carrier modulations with linear phase noise. The closed-form, approximate ML detectors perform almost the same as the exact one, and are much more efficient in implementation. For strong laser phase noise or high SNR, the optimal DB asymptotically becomes circular in the middle of two rings. Our approximate ML detectors thus approach the AS detector $\widehat{S}_{AS}$, which performs ring detection and phase detection separately. One can implement $\widehat{S}_{AS}$ in phase noise, even without the knowledge of the channel parameters $\sigma_{\tilde{\theta}}^2$ and N_0. This makes the AS detector more useful in practice. It should be emphasized that these detectors can apply to any received signal model with time-varying phase and constant amplitude, including the signal model in the presence of oscillator phase noise and quasi-static fading channels where the fading gain is assumed time-invariant and known to the receiver [9, 10].

Our approximate ML detectors and AS detector can be further used to optimize multiple-ring constellations. These results will be reported in Chap. 5. In addition, the approximate MAP detectors can be used for iterative decoding.

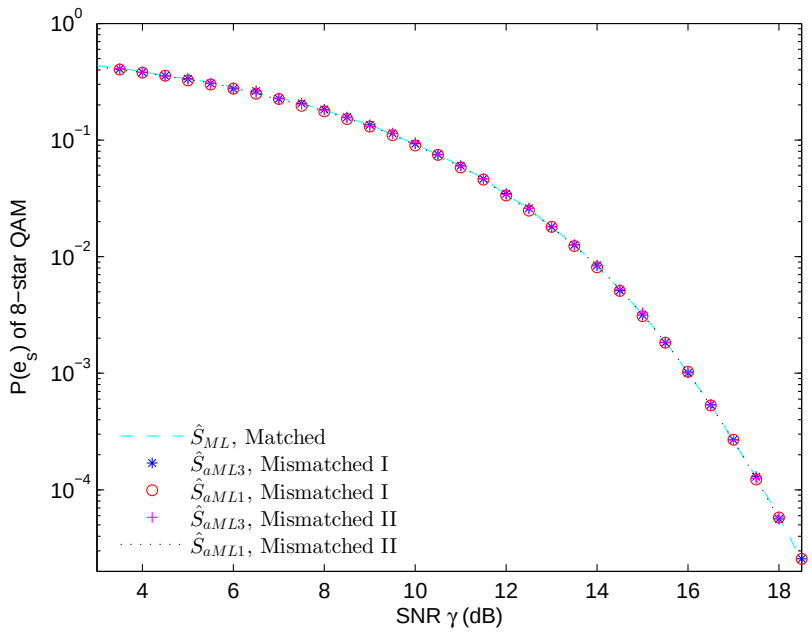

(a)

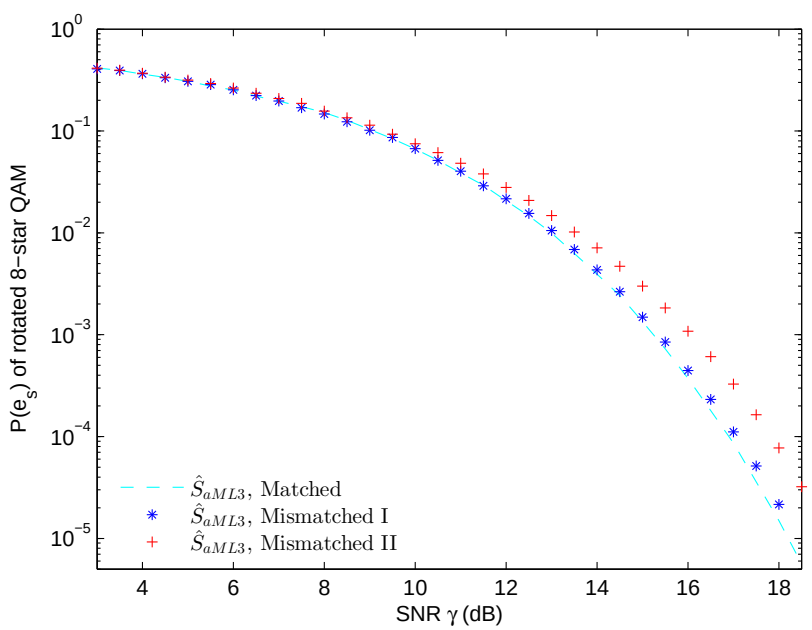

(b)

Figure 3.14: Mismatch of N_0 and $\sigma_{\tilde{\theta}}^2$ in ML detection: (a) 8-star QAM; (b) rotated 8-star QAM.

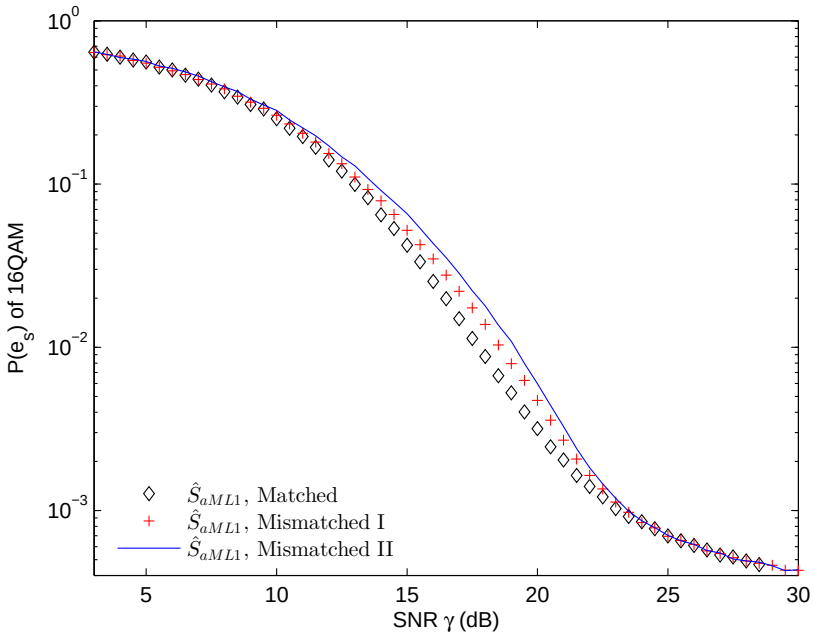

(a)

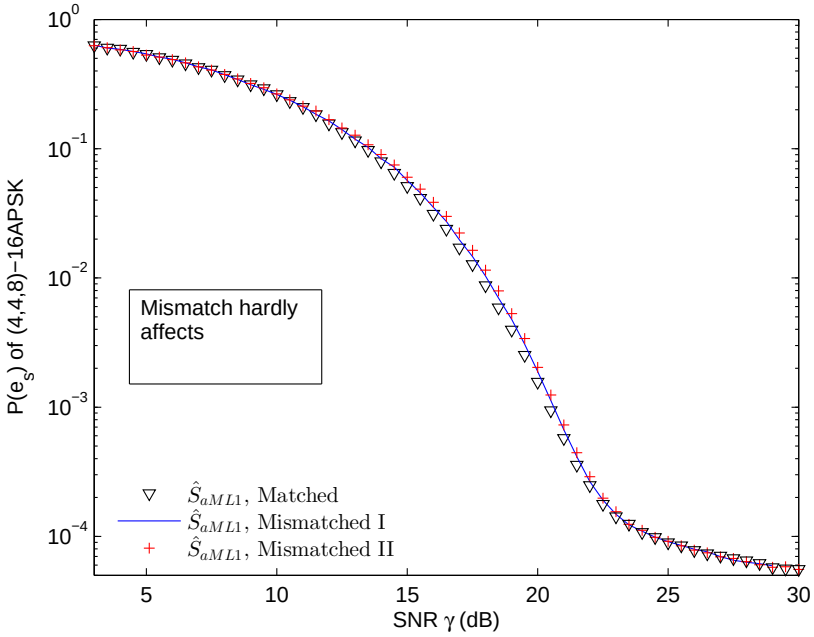

(b)

Figure 3.15: Mismatch of N_0 and $\sigma_{\tilde{\theta}}^2$ in ML detection: (a) 16QAM; (b) (4,4,8)-16APSK.

Chapter 4

Unified Error Probability Analysis in Phase Noise

To efficiently and accurately predict the error performance of the robust detectors impaired by unknown phase noise, this chapter provides a unified and systematic approach to predicting the error probability of MPSK, M-QAM and M-APSK in the presence of AWGN and phase reference error (PRE). Besides, we generalize our systematic approach to obtain the SEP and BEP results of Gray coded MDPSK with residual phase noise (RPN). There are very limited results in the existing literature, where the exact results for MPSK and MDPSK involve very complex multiple integrals and do not facilitate further analysis. Here, simple, accurate and closed-form approximations to the SEP and BEP are derived, and all the results are expressed in terms of Gaussian Q-function. Numerical results are given to validate the accuracy of our derivation.

In Section 4.1, we derive the approximate SEP and BEP expressions for MPSK with the ML detector. Section 4.2 applies our approach to obtain the SEP and BEP approximations for MDPSK with differential detection. New SEP results for the annular-sector (AS) detector are derived in Section 4.3 for multiple-ring constellations, such as M-QAM and M-APSK in the presence of AWGN and PRE.

4.1 Error Probability of MPSK with ML Detection

Based on the received signal model (2.3) with $A_i = \sqrt{E_s}$ for MPSK, we will derive the closed-form error probability expressions of the ML detector. As given

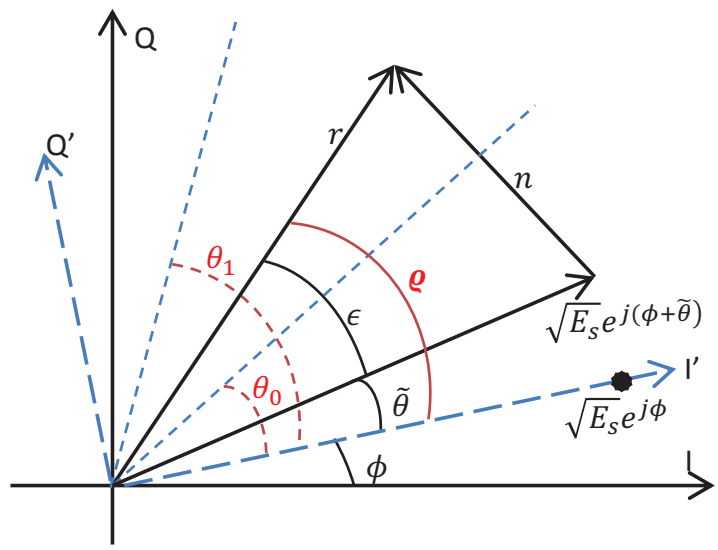

Figure 4.1: Geometric representation of the received signal r for MPSK.

by (2.13) in Section 2.1.2, we have $\varrho \sim N(0, \frac{N_0}{2A_i^2} + \sigma_{\tilde{\theta}}^2)$ in the range $[-\pi, \pi)$, which is the Gaussian AOPN+PRE model. Fig. 4.1 gives a geometric representation of $\sqrt{E_s}e^{j(\phi+\tilde{\theta})}$, n and r in the in-phase-and-quadrature (I-Q) coordinate complex plane.

As a result, the probability of the received signal phasor r falling in any sector, i.e., the probability of the event: $\theta_0 \leq \varrho < \theta_1$, with any transmitted phase ϕ, can be easily calculated, as Fig. 1 shows. Here, we assume arbitrary angles $\theta_0 < \theta_1$ within $[0, \pi)$ from the new coordinate system I'-Q', which is the I-Q-coordinate system rotated by the angle ϕ. Thus, we have

$$P(\theta_0 \leq \varrho < \theta_1) = Q\left(\frac{\theta_0}{\sqrt{0.5\gamma^{-1} + \sigma_{\tilde{\theta}}^2}}\right) - Q\left(\frac{\theta_1}{\sqrt{0.5\gamma^{-1} + \sigma_{\tilde{\theta}}^2}}\right) \tag{4.1}$$

where we have $\gamma = \frac{E_s}{N_0}$, and $Q(x) = \frac{1}{\sqrt{2\pi}} \int_x^\infty \exp\left(-\frac{y^2}{2}\right) dy, x \geq 0$, is the Gaussian Q-function.

The result (4.1) is the explicit, closed-form expression that we will use

throughout this section. We define e_s and e_b as the events of symbol error and bit error, respectively, and $c_s = \overline{e_s}$ as the event of correct symbol decision..

4.1.1 Unified SEP Expression of MPSK with PRE

Since the analysis on the SEP of BPSK has been done before [46], we will derive the approximate SEP expression of MPSK for $M \geq 4$ with PRE via our new result (4.1), to show the accuracy of our unified approach.

For MPSK, we assume the modulated phase ϕ takes on each of the values in $\left\{\phi_i = \frac{2\pi i}{M}\right\}_{i=0}^{M-1}$ with equal probability, i.e., $P(\phi = \phi_i) = \frac{1}{M}$, for any i. Let $P(c_s|\phi = 0)$ represent the correct-decision probability given the signal $\phi = 0$ is sent, i.e., $P(c_s|\phi = 0) = P(\varrho \in [-\frac{\pi}{M}, \frac{\pi}{M})|\phi = 0)$. Noting that we have $P(\varrho \in [-\frac{\pi}{M}, 0)|\phi = 0) = P(\varrho \in [0, \frac{\pi}{M})|\phi = 0)$ by symmetry, it follows that

$$P(c_s|\phi = 0) = 1 - 2Q\left(\frac{\pi}{M}\frac{1}{\sqrt{0.5\gamma^{-1} + \sigma_{\tilde{\theta}}^2}}\right) \tag{4.2}$$

from (4.1) with $\theta_0 = 0$ and $\theta_1 = \frac{\pi}{M}$. Therefore, the new SEP expression of MPSK with AOPN+PRE is given by

$$P(e_s) = 2Q\left(\frac{\pi}{M}\frac{1}{\sqrt{0.5\gamma^{-1} + \sigma_{\tilde{\theta}}^2}}\right). \tag{4.3}$$

First, when $\sigma_{\tilde{\theta}}^2$ is small enough, i.e., $\gamma^{-1} \gg 2\sigma_{\tilde{\theta}}^2$, (4.3) simplifies to $2Q(\frac{\pi\sqrt{2\gamma}}{M})$, which corresponds to the case of no PRE. This result is accurate for $M \geq 4$, since it is the same as [14, eq.(4.3-19)]. Second, when $\gamma \gg (2\sigma_{\tilde{\theta}}^2)^{-1}$, (4.3) reduces to $2Q(\frac{\pi}{M\sqrt{\sigma_{\tilde{\theta}}^2}})$. This is the error floor term denoted as P_{EF} for any MPSK, representing the irreducible SEP due to PRE.

For comparison, the exact conditional SEP expressions for $M \geq 4$ are derived by the polar-coordinate method [71] for $0 < \tilde{\theta} < \pi$, since we have $P(e_s \mid \tilde{\theta},\ 0 < \tilde{\theta} <$

$\pi) = P(e_s \mid \tilde{\theta}, \ -\pi < \tilde{\theta} < 0)$ by symmetry. We thus have

$$P(e_s \mid \tilde{\theta}) = \begin{cases} \int\limits_{\frac{\pi}{M}-\tilde{\theta}}^{\pi} f_1(x,\tilde{\theta})dx + \int\limits_{-\pi}^{-\frac{\pi}{M}-\tilde{\theta}} f_2(x,\tilde{\theta})dx, \\ \qquad\qquad 0 < \tilde{\theta} < \frac{\pi}{M} \\ 1 - \int\limits_{-\pi}^{\frac{\pi}{M}-\tilde{\theta}} f_1(x,\tilde{\theta})dx + \int\limits_{-\pi}^{-\frac{\pi}{M}-\tilde{\theta}} f_2(x,\tilde{\theta})dx, \\ \qquad\qquad \frac{\pi}{M} < \tilde{\theta} < \frac{\pi(M-1)}{M} \\ 1 - \int\limits_{-\pi}^{\frac{\pi}{M}-\tilde{\theta}} f_1(x,\tilde{\theta})dx, \qquad \frac{\pi(M-1)}{M} < \tilde{\theta} < \pi \end{cases}$$

where $f_1(x,\tilde{\theta})$ and $f_2(x,\tilde{\theta})$ are given, respectively, by

$$f_1(x,\tilde{\theta}) = \frac{1}{2\pi} \exp\left[-\frac{\gamma \sin^2(\frac{\pi}{M} - \tilde{\theta})}{\sin^2(x - \frac{\pi}{M} + \tilde{\theta})}\right]$$

and

$$f_2(x,\tilde{\theta}) = \frac{1}{2\pi} \exp\left[-\frac{\gamma \sin^2(\frac{\pi}{M} + \tilde{\theta})}{\sin^2(-x - \frac{\pi}{M} - \tilde{\theta})}\right].$$

Finally, the exact average SEP is given by

$$P(e_s) = 2\int_0^{\pi} P(e_s \mid \tilde{\theta}) p(\tilde{\theta}) d\tilde{\theta}. \tag{4.4}$$

For PLL tracking, $p(\tilde{\theta})$ is given in (2.5). For DA ML PE, we have $\tilde{\theta} \sim N(0, \ \frac{2L^2+3L+1}{6L}\sigma_p^2 + \frac{\sigma_{n'}^2}{2L})$. This expression (4.4) is used to compute the exact results in Figs. 4.2-4.3. Moreover, the exact floor term for any MPSK is thus $\int_I p(\tilde{\theta})d\tilde{\theta}$, where $I = \{\tilde{\theta} : \pi/M < |\tilde{\theta}| < \pi\}$. Numerical comparison shows that our new error floor term $P_{EF} = 2Q(\frac{\pi}{M\sqrt{\sigma_{\tilde{\theta}}^2}})$ is a very good approximation to the exact one for a wide range of σ^2 for $M \geq 4$, the same as MDPSK case shown later.

Fig. 4.3	$M = 4(\gamma)$	$M = 8(\gamma)$	$M = 16(\gamma)$
Eq.(4.3)	14.15 dB	19.78 dB	25.88 dB
Eq.(4.4)	14.62 dB	19.91 dB	25.91 dB
Eq.(4.4)−Eq.(4.3)	0.47 dB	0.13 dB	0.03 dB

Table 4.1: Difference in γ at the SEP of 10^{-6} for DA ML PE

Fig. 4.4	$M = 4(\gamma)$	$M = 8(\gamma)$	$M = 16(\gamma)$
Eq.(4.3)	12.04 dB	18.57 dB	27.52 dB
Eq.(4.4)	12.55 dB	18.69 dB	27.56 dB
Eq.(4.4)−Eq.(4.3)	0.51 dB	0.12 dB	0.04 dB

Table 4.2: Difference in γ at the SEP of 10^{-4} for PLL

4.1.2 Numerical Comparison with Exact SEP

Figs. 4.2-4.3 show the comparison between our result (4.3) and the exact one (4.4) given in double-integral form for PLL and DA ML PE method, respectively. For PLL, we set $\alpha = 150$ for all MPSK, which corresponds to an rms phase error of $\sqrt{\text{var}[\tilde{\theta}]} = 4.68°$ [46]. For DA ML, we set $L = 8$, and σ_p^2 (rad^2) is set to be $4\pi \times 10^{-4}$, $5.4\pi \times 10^{-5}$ and $16\pi \times 10^{-6}$ for QPSK, 8PSK and 16PSK, respectively, which correspond to 4MHz, 360KHz and 80KHz of combined laser linewidth at 40Gbit/s [15]. As an example in Fig. 4.2, the difference in γ at a specific SEP of 10^{-6} for QPSK is 0.47dB, since we have $\gamma = 14.15$dB in (4.3) and $\gamma = 14.62$dB in (4.4). For Fig. 4.3, Table 4.1 lists the differences in γ at the SEP of 10^{-6} between (4.3) and (4.4). We can see that the maximum difference in γ is less than 0.5dB and the difference decreases as M increases. The comparison shows that our unified approach is mathematically simpler and increasingly more accurate through the whole SNR region as M increases. Furthermore, Fig. 4.2 shows that the error floor term P_{EF} is very important especially for higher-order MPSK.

It should be noted that in the design of a typical PLL, the PLL SNR α needs to be designed according to the required SNR of the system. It means that α should be designed larger as M increases. A larger α will reduce the error floor term. In Fig.

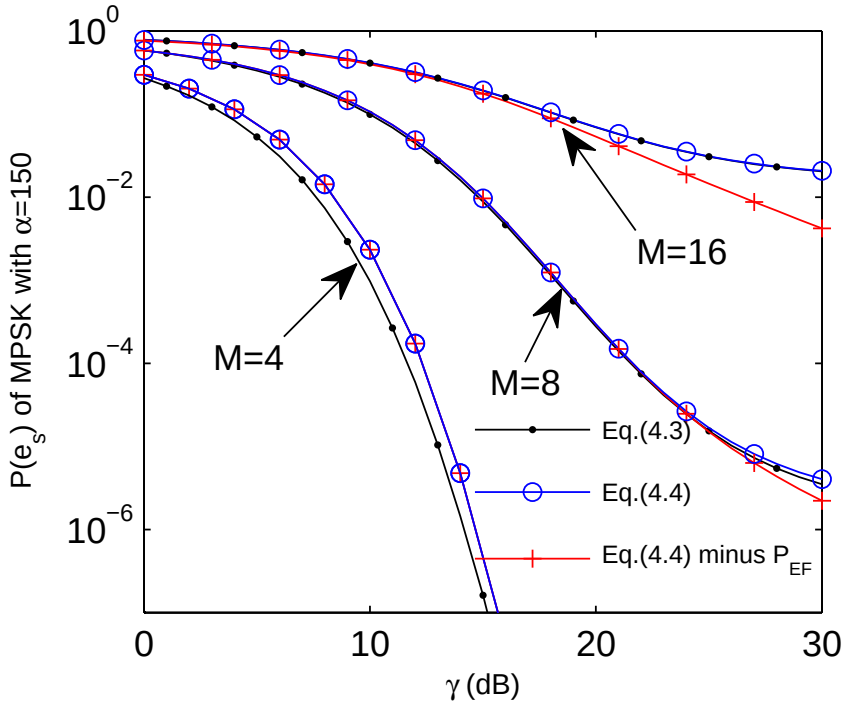

Figure 4.2: SEP comparison for PLL with $\alpha = 150$.

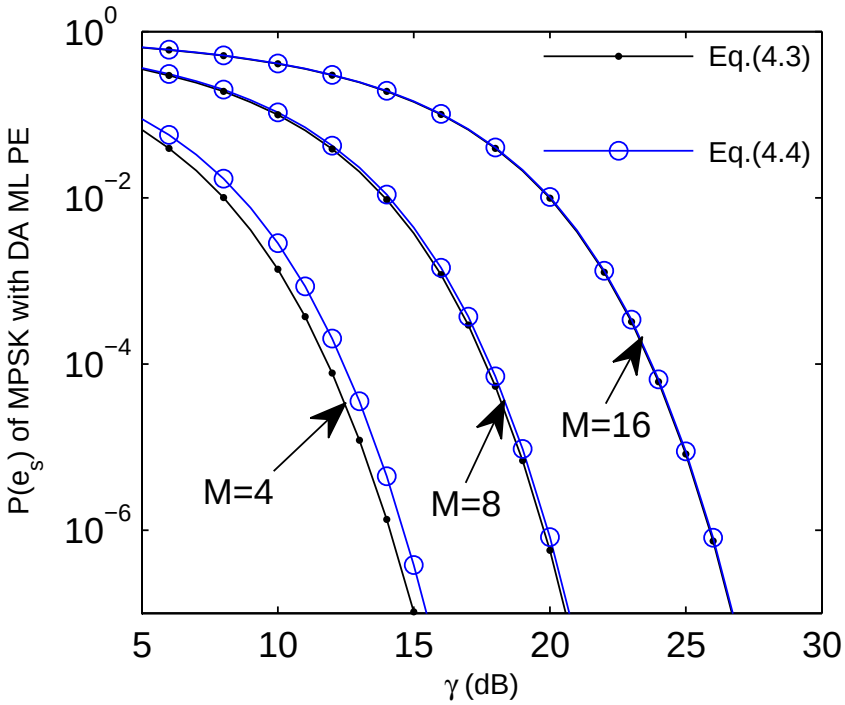

Figure 4.3: SEP comparison for DA ML PE with $L = 8$.

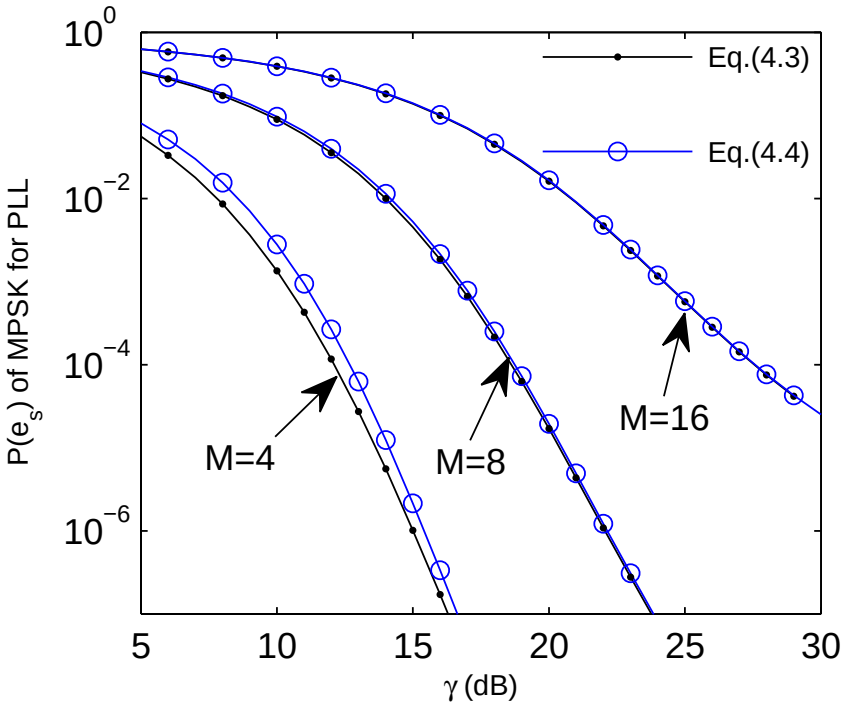

Figure 4.4: SEP comparison for PLL with different α.

4.2, we keep $\alpha = 150$ for all values of M. Now in Fig. 4.4, we set α to be 100, 300 and 600 for QPSK, 8PSK and 16PSK, respectively, which correspond to rms phase errors of $5.73°, 3.31°$ and $2.34°$, respectively, to show the numerical comparison. Table 4.2 displays the differences in γ at a specific SEP of 10^{-4} between (4.3) and (4.4) as an example of Fig. 4.4. It can be seen that the difference is also very small.

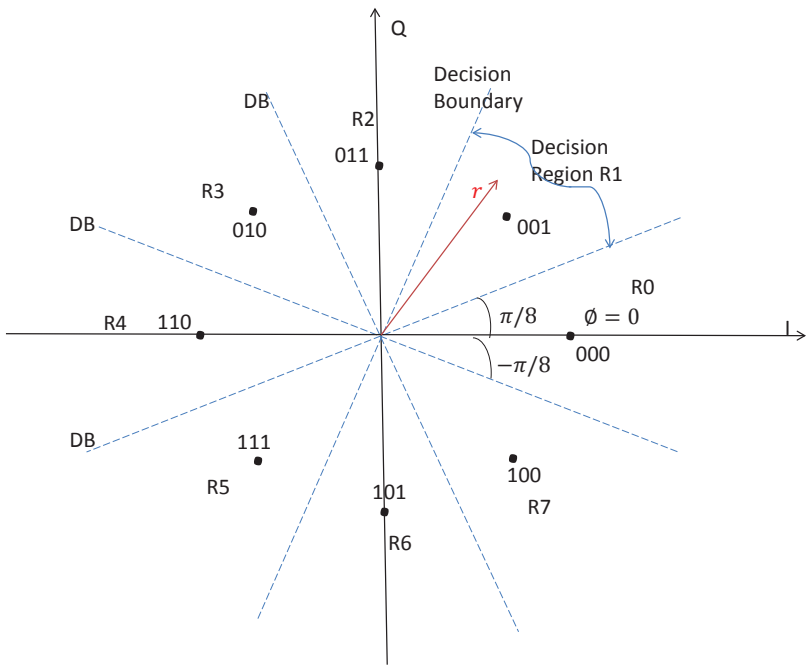

Figure 4.5: Signal-space diagram for 8-PSK (Gray coded).

4.1.3 Unified BEP Expressions of MPSK with PRE

Our approach enables much easier prediction on the BEP of higher-order MPSK with PRE. To show this, this section gives the unified approximate BEP results of MPSK (Gray coded) with AWGN and PRE. Specifically, the energy per bit, E_b, equals $\frac{E_s}{\log_2 M}$ [14].

Our unified approach combined with the method of Lee [106] or the method of Lassing [107] is used to obtain new approximate BEP expressions for $M = 4, 8$ and 16. For $M \geq 32$, the approach is the same. First, let A_k represent the probability of the received signal phasor r falling into the decision region R_k of MPSK when the signal $\phi = 0$ is sent, i.e., $A_k = P(r \in R_k | \phi = 0)$, integer $k \in [0, M-1]$. As Figs.4.5-4.6 show, R_k corresponds to the region where $\theta_0 = \frac{(2k-1)\pi}{M}$ and $\theta_1 = \frac{(2k+1)\pi}{M}$ in (4.1).

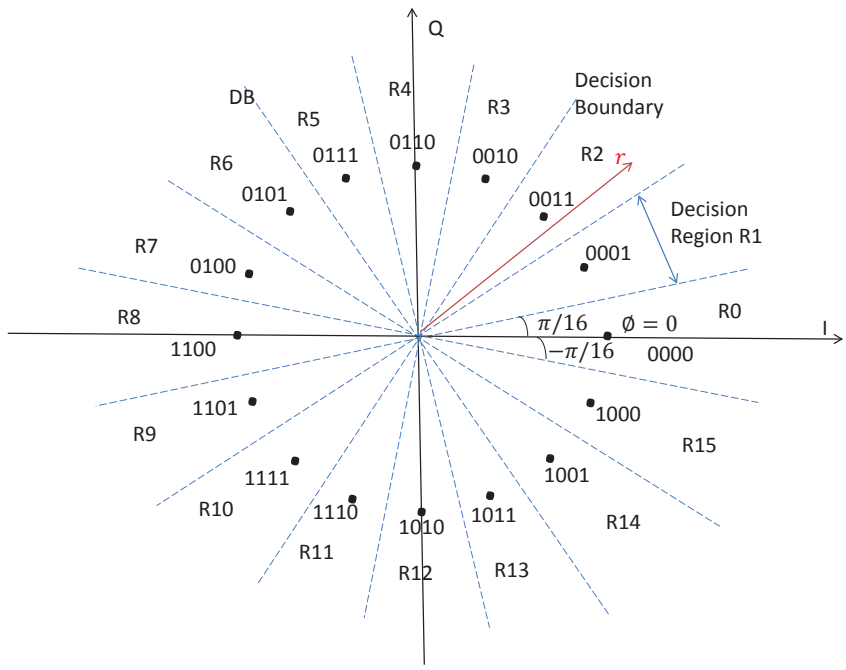

Figure 4.6: Signal-space diagram for 16-PSK (Gray coded).

Therefore, for any $k < \frac{M}{2}$, we have

$$\begin{aligned} A_k &= P\big(\varrho \in [\frac{(2k-1)\pi}{M}, \frac{(2k+1)\pi}{M})\big|\phi = 0\big) \\ &= Q\left(\frac{(2k-1)\pi/M}{\sqrt{0.5\gamma^{-1} + \sigma_{\tilde{\theta}}^2}}\right) - Q\left(\frac{(2k+1)\pi/M}{\sqrt{0.5\gamma^{-1} + \sigma_{\tilde{\theta}}^2}}\right). \end{aligned} \tag{4.5}$$

For the special case of $k = \frac{M}{2}$, we have

$$\begin{aligned} A_{\frac{M}{2}} &= 2P\big(\varrho \in [\frac{(M-1)\pi}{M}, \pi)\big|\phi = 0\big) \\ &= 2Q\left(\frac{(M-1)\pi/M}{\sqrt{0.5\gamma^{-1} + \sigma_{\tilde{\theta}}^2}}\right) - 2Q\left(\frac{\pi}{\sqrt{0.5\gamma^{-1} + \sigma_{\tilde{\theta}}^2}}\right). \end{aligned} \tag{4.6}$$

Normally, $\frac{\pi}{\sqrt{0.5\gamma^{-1}+\sigma_{\tilde{\theta}}^2}}$ is so large that $Q\Big(\frac{\pi}{\sqrt{0.5\gamma^{-1}+\sigma_{\tilde{\theta}}^2}}\Big)$ can be dropped. Moreover, the

following relation holds [106]:

$$A_0 > A_1 = A_{M-1} > \cdots > A_{M/2-1} = A_{M/2+1} > A_{M/2}. \tag{4.7}$$

QPSK Case

The BEP result of QPSK with PRE is thus derived as [106]

$$\begin{aligned} P(e_b) = P(e_b|\phi = 0) &= \frac{1}{2}[A_1 + 2A_2 + A_3] = A_1 + A_2 \\ &\approx Q\left(\frac{\pi/4}{\sqrt{0.5\gamma^{-1} + \sigma_{\tilde{\theta}}^2}}\right) + Q\left(\frac{3\pi/4}{\sqrt{0.5\gamma^{-1} + \sigma_{\tilde{\theta}}^2}}\right). \end{aligned} \tag{4.8}$$

8PSK Case

The BEP result of 8PSK in terms of A_k's is expressed as [106]

$$P(e_b) = P(e_b|\phi = 0) = \frac{2}{3}[\sum_{k=1}^{6} A_k]. \tag{4.9}$$

Based on (4.5)−(4.7), we thus have

$$\begin{aligned} P(e_b) &= \frac{2}{3}[\sum_{k=1}^{7} A_k - A_7] = \frac{2}{3}[P(e_s) - A_1] \\ &\approx \frac{2}{3}\left[Q\left(\frac{\pi/8}{\sqrt{0.5\gamma^{-1} + \sigma_{\tilde{\theta}}^2}}\right) + Q\left(\frac{3\pi/8}{\sqrt{0.5\gamma^{-1} + \sigma_{\tilde{\theta}}^2}}\right)\right]. \end{aligned} \tag{4.10}$$

16PSK Case

Lassing, etc [107] pointed out that the BEP with Gray mapping for $M \geq 16$ is dependent on the transmitted symbols. Here, our unified approach together with the average distance spectrum $\bar{d}(k)$ [107] is used to obtain the BEP results for $M \geq 16$.

Since $\bar{d}(k)$ and $A(k)$ are symmetric around $k = \frac{M}{2}$, the exact BEP expression

of 16PSK is derived as

$$P(e_b) = \frac{1}{4}\sum_{k=1}^{15} \bar{d}(k)A(k) = \frac{1}{2}(A_1 + 2A_2 + 2A_3 + 2A_4 + 2.5A_5 + 3A_6 + 2.5A_7 + A_8). \tag{4.11}$$

Calculating A_k's separately via (4.5)−(4.7), we have

$$\begin{aligned} P(e_b) \approx \frac{1}{2}\Bigg[& Q\left(\frac{\pi/16}{\sqrt{0.5\gamma^{-1}+\sigma_{\tilde{\theta}}^2}}\right) + Q\left(\frac{3\pi/16}{\sqrt{0.5\gamma^{-1}+\sigma_{\tilde{\theta}}^2}}\right) \\ & + \frac{1}{2}Q\left(\frac{9\pi/16}{\sqrt{0.5\gamma^{-1}+\sigma_{\tilde{\theta}}^2}}\right) + \frac{1}{2}Q\left(\frac{11\pi/16}{\sqrt{0.5\gamma^{-1}+\sigma_{\tilde{\theta}}^2}}\right) \\ & - \frac{1}{2}Q\left(\frac{13\pi/16}{\sqrt{0.5\gamma^{-1}+\sigma_{\tilde{\theta}}^2}}\right) - \frac{1}{2}Q\left(\frac{15\pi/16}{\sqrt{0.5\gamma^{-1}+\sigma_{\tilde{\theta}}^2}}\right)\Bigg]. \end{aligned} \tag{4.12}$$

Similar to the case of 16PSK, the BEP results of MPSK for higher order M can also be expressed as linear combinations of single Gaussian Q-functions, via our unified approach. These approximate expressions allow a simple and quick estimation of the BEP performance as functions of the different phase error variances.

4.1.4 Numerical Comparison with Exact BEPs

The exact BEP result of QPSK with PRE is given in detail by [55, eqs.(4)-(13)]. The BEP results conditioned on the PRE $\tilde{\theta}$ for $M = 8$ and 16 are given by [58, eq.(5)] and [58, eqs.(8)-(13)], respectively, where the trivial difference caused by different transmitted symbols is ignored for $M = 16$. It follows that averaging these conditional results over the distribution of $\tilde{\theta}$ from 0 to π gives the exact BEP results [58]. For PLL tracking, $p(\tilde{\theta})$ is given in (2.5). For DA ML PE, we have $\tilde{\theta} \sim N(0, \frac{2L^2+3L+1}{6L}\sigma_p^2 + \frac{\sigma_{n'}^2}{2L})$. The details are not shown here.

Figs. 4.7-4.8 show the comparison between our results and the exact ones for PLL and DA ML PE method, respectively. For PLL, we set $\alpha = 100$ and 200, which

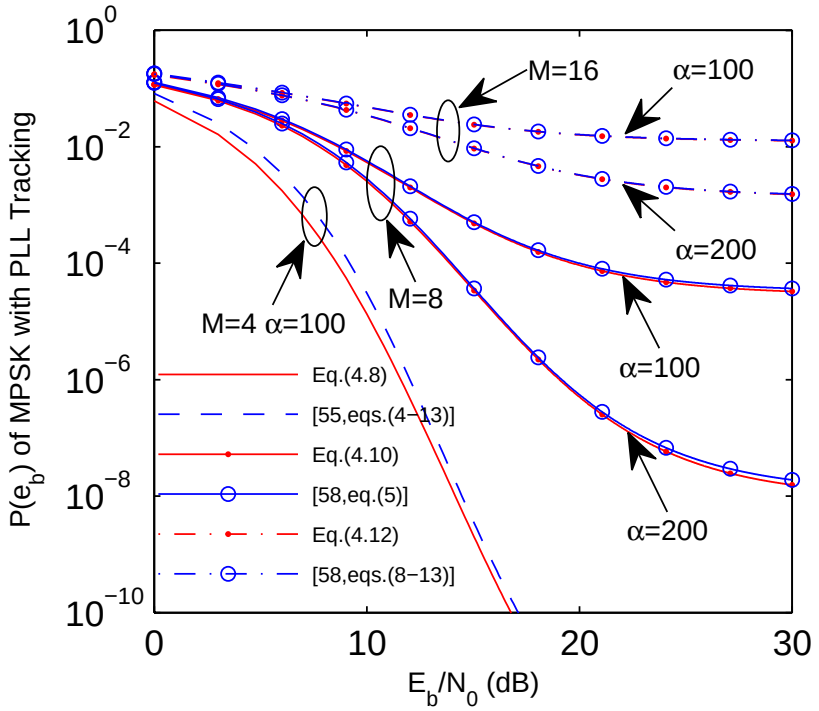

Figure 4.7: BEP comparison for MPSK with PLL: $\alpha = 100$ and 200.

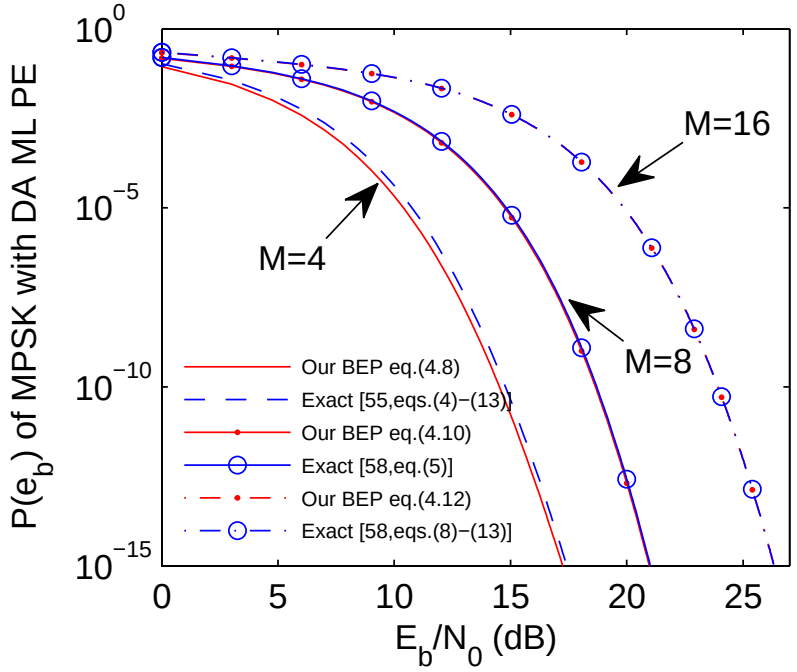

Figure 4.8: BEP comparison for MPSK with DA ML: $L = 6$.

Fig. 4.8	$M = 4(\frac{E_b}{N_0})$	$M = 8(\frac{E_b}{N_0})$	$M = 16(\frac{E_b}{N_0})$
Ours	11.46 dB	15.8 dB	20.93 dB
Exact	11.8 dB	15.85 dB	20.93 dB
Difference	0.34 dB	0.05 dB	0 dB

Table 4.3: Difference in E_b/N_0 at the BEP of 10^{-6} for DA ML PE

correspond respectively to rms phase errors of $\sqrt{\text{var}[\tilde{\theta}]} = 5.73°$ and $\sqrt{\text{var}[\tilde{\theta}]} = 4.05°$. For DA ML, we set $L = 6$, and σ_p^2 (rad^2) is set to be $4.4\pi \times 10^{-4}$, $6\pi \times 10^{-5}$ and $17.6\pi \times 10^{-6}$ for QPSK, 8PSK and 16PSK, respectively, which correspond to 4.4MHz, 400KHz and 88KHz combined laser linewidth at 40Gbit/s [15]. In Fig. 4.7, for instance, the difference in E_b/N_0 at a specific BEP of 10^{-6} for QPSK is 0.5dB, since E_b/N_0 equals 11.5dB in (4.8) and 12dB in the exact result. For Fig. 4.8, Table 4.3 lists the differences in E_b/N_0 at the SEP of 10^{-6} between our approximate results and the exact ones. We can see that although we assume high SNR for our approach, our results are accurate throughout the whole SNR region. It is clear that our expressions are simpler and do not involve any double-integrals, compared with the exact BEP results. Moreover, our approximations are increasingly more accurate as M increases.

In addition, our BEP results (4.8), (4.10) and (4.12) with $\sigma_{\tilde{\theta}}^2 = 0$ are accurate approximations for the BEP of coherent MPSK with no PRE, i.e., $\tilde{\theta}(k) = 0$ for any k in (2.3).

4.2 Error Probability of Differentially Detected MDPSK with RPN

To further demonstrate the usefulness of our systematic approach, we derive the approximate SEP/BEP expressions for differentially detected MDPSK via the AOPN+RPN model, and compare them with the exact ones which are shown concretely for the first time.

4.2.1 SEP Expressions and Numerical Comparison

Based on the signal model (2.14) in Section 2.2, we have $\Delta\tilde{\varrho}(k) \sim N(0,\ \gamma^{-1} + \sigma_p^2)$, which is the Gaussian AOPN+RPN model. The new approximate SEP expression is thus derived as

$$\begin{aligned} P(e_s) &= P(e_s \big| \Delta\phi_0 = 0) = 1 - P\big(\Delta\tilde{\varrho} \in (-\frac{\pi}{M}, \frac{\pi}{M}) \big| \Delta\phi_0 = 0\big) \\ &\approx 2Q\left(\frac{\pi}{M}\frac{1}{\sqrt{\gamma^{-1} + \sigma_p^2}}\right). \end{aligned} \tag{4.13}$$

First, when σ_p^2 is small enough, $\gamma^{-1} \gg \sigma_p^2$, (4.13) simplifies to $2Q(\frac{\pi\sqrt{\gamma}}{M})$, which corresponds to the case of no RPN. This result is accurate for $M \geq 4$, compared with the exact one given by [12, eq.(8.90)]. Also, a comparison between (4.13) with $\sigma_p^2 = 0$ and (4.3) with $\sigma^2 = 0$ gives the well-known fact that the performance of coherent MPSK is 3dB better than that of differentially detected MDPSK. Second, when $\gamma \gg \sigma_p^{-2}$, (4.13) reduces to $2Q(\frac{\pi}{M\sqrt{\sigma_p^2}})$. This is the error floor term for any MDPSK, representing the irreducible SEP due to RPN.

The exact SEP result of 2DPSK is given by [60, eqs.(3)-(6)]. For $M \geq 4$, the exact SEP results of MDPSK with phase noise have not been derived so far. Therefore, we will derive the exact ones based on the results [92, eqs.(9)(11)]. Here, we assume the signal $\Delta\phi_0 = 0$ is transmitted. Thus the angle between the signal vectors $r(k)$ and $r(k-1)$ is $\Delta\tilde{\varrho}$. Let ψ_1 and ψ_2, with $\psi_1 < \psi_2$, be angles lying within the particular 2π interval of interest. According to [92, eq.(9)], the probability

$P(\psi_1 < \Delta\tilde{\varrho} < \psi_2)$ can be expressed in terms of an auxiliary function $F(.)$:

$$P(\psi_1 < \Delta\tilde{\varrho} < \psi_2) = \begin{cases} F(\psi_2) - F(\psi_1) + 1, & \psi_1 < \Delta\theta < \psi_2 \\ F(\psi_2) - F(\psi_1), & \Delta\theta < \psi_1 \text{ or } \Delta\theta > \psi_2 \end{cases} \tag{4.14}$$

where $F(.)$ is given as [92, eq.(11)]

$$F(\psi) = \frac{\sin(\Delta\theta - \psi)}{4\pi} \int_{-\pi/2}^{\pi/2} \frac{e^{-\frac{E_s}{N_0}[1-\cos(\Delta\theta-\psi)\cos t]}}{1 - \cos(\Delta\theta - \psi)\cos t} dt. \tag{4.15}$$

It can be seen that $F(\psi) = F(\psi + 2\pi)$.

Therefore, we can have

$$P(e_s|\Delta\theta) = \begin{cases} F\left(-\frac{\pi}{M}\right) - F\left(\frac{\pi}{M}\right), & -\frac{\pi}{M} < \Delta\theta < \frac{\pi}{M} \\ 1 + F\left(-\frac{\pi}{M}\right) - F\left(\frac{\pi}{M}\right), & \frac{\pi}{M} < |\Delta\theta| < \pi \end{cases}$$

The exact SEP expression is thus obtained as

$$\begin{aligned} P(e_s) &= \int_{-\pi}^{\pi} P(e_s|\Delta\theta) p(\Delta\theta) d\Delta\theta \\ &= \int_{-\pi}^{\pi} \left[F\left(-\frac{\pi}{M}\right) - F\left(\frac{\pi}{M}\right)\right] p(\Delta\theta) d\Delta\theta + \int_I p(\Delta\theta) d\Delta\theta. \end{aligned} \tag{4.16}$$

Here, $I = \{\Delta\theta : \pi/M < |\Delta\theta| < \pi\}$, and $p(\Delta\theta)$ is the Gaussian pdf with zero-mean and variance σ_p^2. Actually, [60, eqs.(3)-(6)] is the same as (4.16) for $M = 2$. The exact error floor term is thus $P_{EF} = \int_I p(\Delta\theta) d\Delta\theta$.

Fig. 4.9 shows that our new error floor term $P_{EF} = 2Q(\frac{\pi}{M\sqrt{\sigma_p^2}})$ is a very good approximation to the exact one for $M \geq 4$ with any σ_p^{-2}. The comparison between (4.13) and (4.16) for $M \geq 4$ is shown in Figs. 4.10-4.11. We can see that our approximate results are accurate for all SNR values of interest.

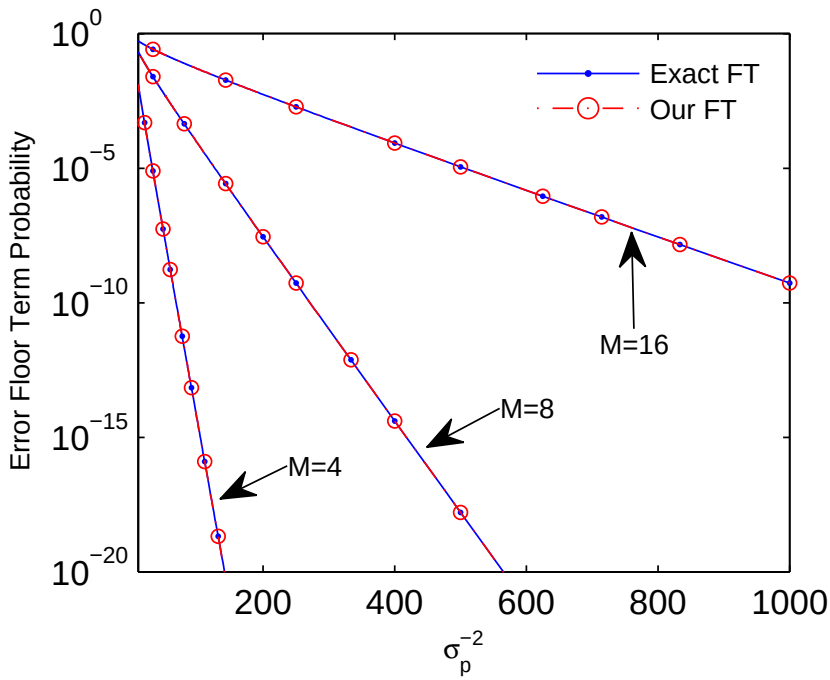

Figure 4.9: Error floor term (FT) P_{EF} comparison for MDPSK with $M \geq 4$.

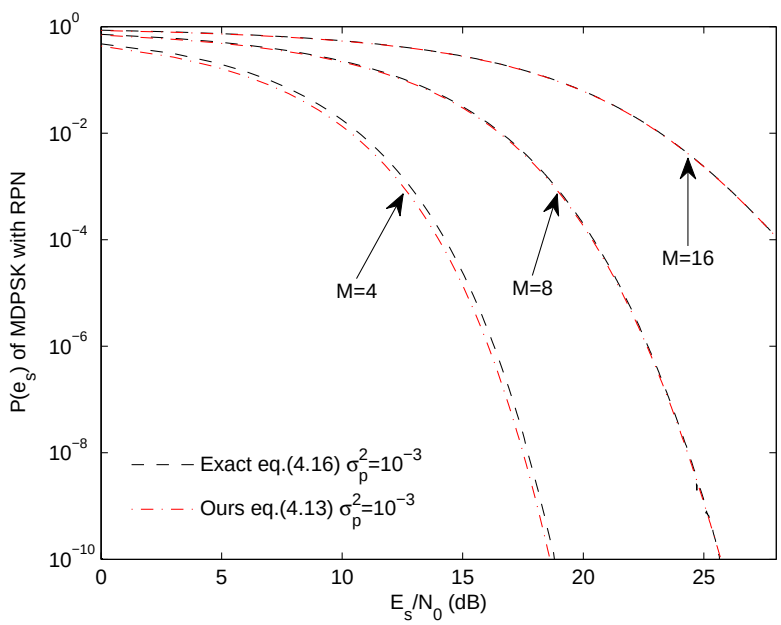

Figure 4.10: SEP comparison for MDPSK with $\sigma_p^2 = 10^{-3}\text{rad}^2$.

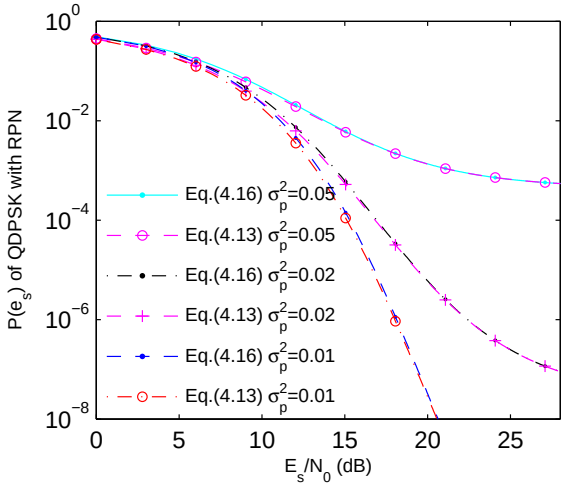

(a)

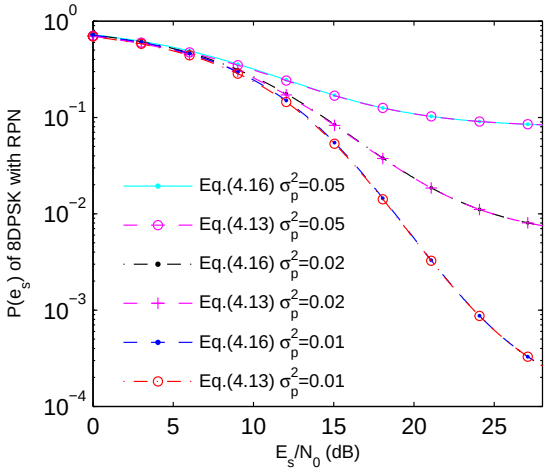

(b)

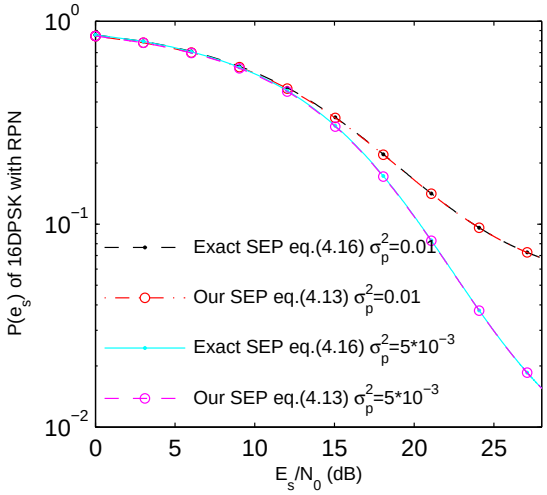

(c)

Figure 4.11: SEP comparison for MDPSK: (a) $M = 4$; (b) $M = 8$; (c) $M = 16$.

4.2.2 Unified Approximate BEP Expressions

We use the approximate Gaussian AOPN+RPN model to obtain new BEP expressions for MDPSK (Gray coded) with phase noise.

Similar to MPSK, we have B_k represent the probability of the event: $\Delta\tilde{\varrho} \in \left[\frac{(2k-1)\pi}{M}, \frac{(2k+1)\pi}{M}\right)$ when the symbol $\Delta\phi_0 = 0$ is sent, i.e., $B_k = P\left(\Delta\tilde{\varrho} \in [\frac{(2k-1)\pi}{M}, \frac{(2k+1)\pi}{M})\middle|\Delta\phi_0 = 0\right)$. The B_k's thus have the same expressions as the A_k's in (4.5)−(4.7), except that the term $0.5\gamma^{-1}$ is replaced by γ^{-1}. Therefore, for $M = 4$, our approach in conjunction with the method of Lee [106] leads to

$$P(e_b) = \frac{1}{2}B_1 + B_2 + \frac{1}{2}B_3 = B_1 + B_2 \approx Q\left(\frac{\pi/4}{\sqrt{\gamma^{-1} + \sigma_p^2}}\right) + Q\left(\frac{3\pi/4}{\sqrt{\gamma^{-1} + \sigma_p^2}}\right). \tag{4.17}$$

For $M = 8$, we have

$$P(e_b) = \frac{2}{3}(P(e_s) - B_1) \approx \frac{2}{3}\left[Q\left(\frac{\pi/8}{\sqrt{\gamma^{-1} + \sigma_p^2}}\right) + Q\left(\frac{3\pi/8}{\sqrt{\gamma^{-1} + \sigma_p^2}}\right)\right]. \tag{4.18}$$

For $M = 16$, our approach in conjunction with the method of Lassing [107] gives the BEP result

$$\begin{aligned} P(e_b) &= \frac{1}{4}\sum_{k=1}^{15} \bar{d}(k)B_k = \frac{1}{2}[P(e_s) - B_1 + 0.5B_5 + B_6 + 0.5B_7] \\ &\approx \frac{1}{2}\left[Q\left(\frac{\pi/16}{\sqrt{\gamma^{-1} + \sigma_p^2}}\right) + Q\left(\frac{3\pi/16}{\sqrt{\gamma^{-1} + \sigma_p^2}}\right)\right] \\ &+ \frac{1}{4}\left[Q\left(\frac{9\pi/16}{\sqrt{\gamma^{-1} + \sigma_p^2}}\right) + Q\left(\frac{11\pi/16}{\sqrt{\gamma^{-1} + \sigma_p^2}}\right)\right] \\ &- \frac{1}{4}\left[Q\left(\frac{13\pi/16}{\sqrt{\gamma^{-1} + \sigma_p^2}}\right) + Q\left(\frac{15\pi/16}{\sqrt{\gamma^{-1} + \sigma_p^2}}\right)\right]. \end{aligned} \tag{4.19}$$

The BEP expressions above are our main results for MDPSK. For $M \geq 32$, the approach is the same. Our results are the only approximations available, even for the case without RPN, i.e., $\sigma_p^2 = 0$.

4.2.3 Exact BEP Results and Numerical Comparison

The exact BEP expressions for $M \geq 4$ with Gray code mapping can be derived based on [92, eqs.(9)(11)]. For simplicity, the signal $\Delta\phi_0 = 0$ is assumed to be sent.

For QDPSK, the events that the angle between the signal vectors $r(k)$ and $r(k-1)$, i.e., $\Delta\tilde{\varrho}$, lies within the ranges $(\pi/4, 3\pi/4)$, $(3\pi/4, 5\pi/4)$ and $(5\pi/4, 7\pi/4)$, correspond to a 1-bit error, a 2-bit error and a 1-bit error, respectively. The probability of each event is different for different subranges of $\Delta\theta$ based on (4.14)-(4.15). It thus follows that we have

$$P(e_b|\Delta\theta) = \begin{cases} F_{QPSK}, & |\Delta\theta| < \frac{\pi}{4} \\ F_{QPSK} + \frac{1}{2}, & \frac{\pi}{4} < |\Delta\theta| < \frac{3\pi}{4} \\ F_{QPSK} + 1, & \frac{3\pi}{4} < |\Delta\theta| < \pi \end{cases} \tag{4.20}$$

where we define

$$F_{QPSK} = \frac{1}{2}\left[F(\frac{7\pi}{4}) + F(\frac{5\pi}{4}) - F(\frac{3\pi}{4}) - F(\frac{\pi}{4})\right]$$

for short. Therefore, the exact BEP result of QDPSK is derived in a double-integral form,

$$P(e_b) = \int_{-\pi}^{\pi} F_{QPSK} p(\Delta\theta) d\Delta\theta + \frac{1}{2}\int_{\frac{\pi}{4}<|\Delta\theta|<\frac{3\pi}{4}} p(\Delta\theta) d\Delta\theta + \int_{\frac{3\pi}{4}<|\Delta\theta|<\pi} p(\Delta\theta) d\Delta\theta. \tag{4.21}$$

Using the same idea as above, the exact BEP result for 8DPSK is derived as

$$\begin{aligned} P(e_b) = \int_{-\pi}^{\pi} \frac{1}{3}\Big[&F(\frac{15\pi}{8}) + F(\frac{13\pi}{8}) + F(\frac{11\pi}{8}) - F(\frac{9\pi}{8}) - F(\frac{7\pi}{8}) + F(\frac{5\pi}{8}) - F(\frac{3\pi}{8}) \\ &-F(\frac{\pi}{8})\Big] p(\Delta\theta) d\Delta\theta + \frac{1}{3}\left(\int_{\frac{\pi}{8}<|\Delta\theta|<\pi} + \int_{\frac{3\pi}{8}<|\Delta\theta|<\pi}\right) p(\Delta\theta) d\Delta\theta. \end{aligned} \tag{4.22}$$

For 16DPSK, ignoring the trivial difference mentioned in [107] for simplicity, we

thus obtain

$$
\begin{aligned}
P(e_b) = \int_{-\pi}^{\pi} \frac{1}{4} \Bigg[& F(\frac{31\pi}{16}) + F(\frac{29\pi}{16}) + F(\frac{27\pi}{16}) - F(\frac{25\pi}{16}) \\
& + F(\frac{23\pi}{16}) + F(\frac{21\pi}{16}) - F(\frac{19\pi}{16}) - F(\frac{17\pi}{16}) - F(\frac{15\pi}{16}) + F(\frac{13\pi}{16}) + F(\frac{11\pi}{16}) \\
& - F(\frac{9\pi}{16}) - F(\frac{7\pi}{16}) + F(\frac{5\pi}{16}) - F(\frac{3\pi}{16}) - F(\frac{\pi}{16}) \Bigg] p(\Delta\theta) d\Delta\theta \\
& + \frac{1}{4} \left(\int_{\frac{\pi}{16} < |\Delta\theta| < \pi} + \int_{\frac{3\pi}{16} < |\Delta\theta| < \pi} + \int_{\frac{9\pi}{16} < |\Delta\theta| < \frac{13\pi}{16}} \right) p(\Delta\theta) d\Delta\theta. \qquad (4.23)
\end{aligned}
$$

As Figs. 4.12-4.13 show, the comparison among these results with different σ_p^2 implies that our approach is accurate through the whole SNR region for a large range of phase noise variance.

Furthermore, we can get the simple, unified BEP expressions for MDPSK without RPN from (4.17)-(4.19) with $\sigma_p^2 = 0$. As Fig. 4.14 shows, these results are also mathematically simpler and increasingly more accurate for larger values of M, in comparison with the exact results in [12, eqs.(8.86)-(8.87)].

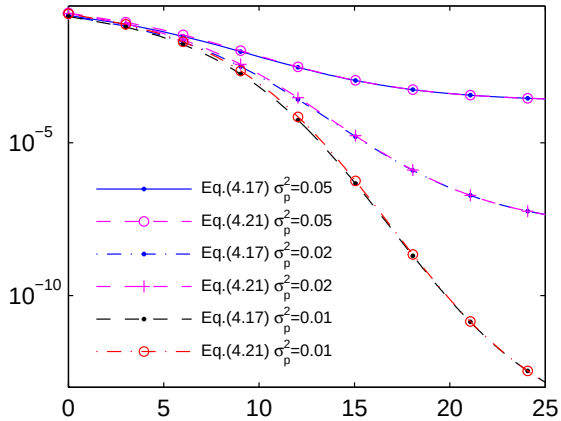

(a)

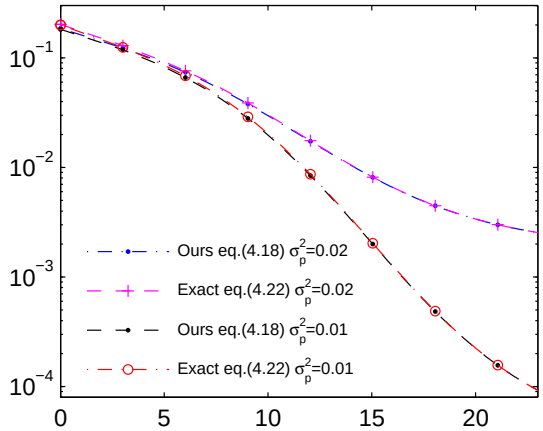

(b)

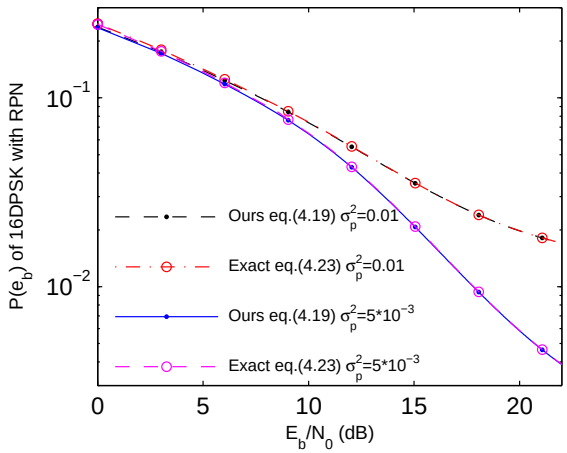

(c)

Figure 4.12: BEP comparison for MDPSK: (a) $M = 4$; (b) $M = 8$; (c) $M = 16$.

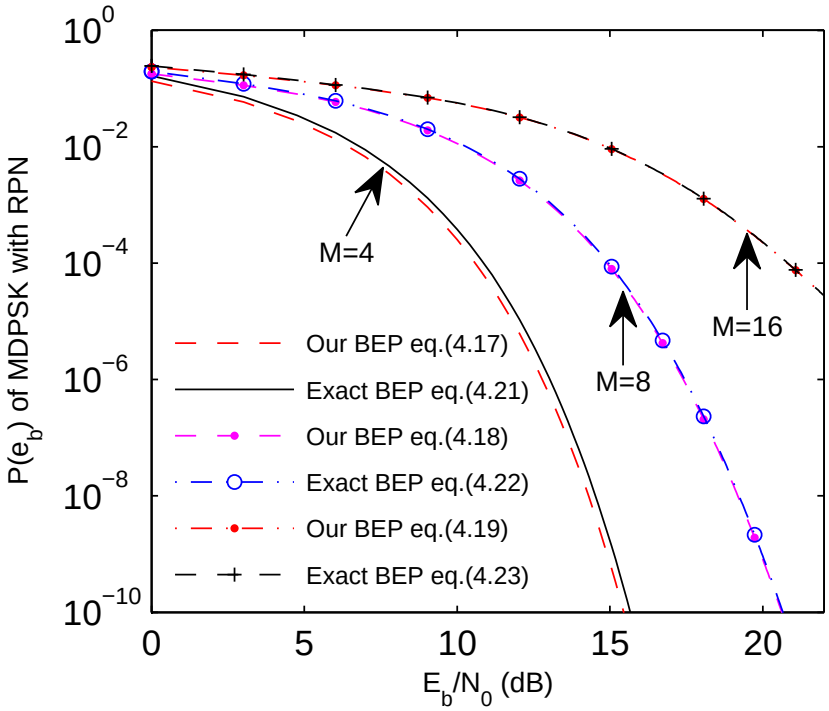

Figure 4.13: BEP comparison for MDPSK with $\sigma_p^2 = 10^{-3}\text{rad}^2$.

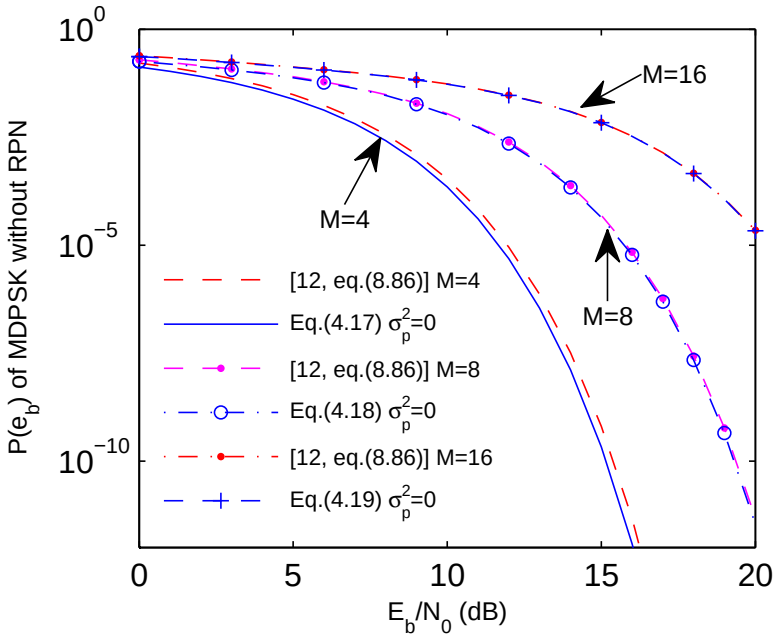

Figure 4.14: BEP comparison for MDPSK with no RPN.

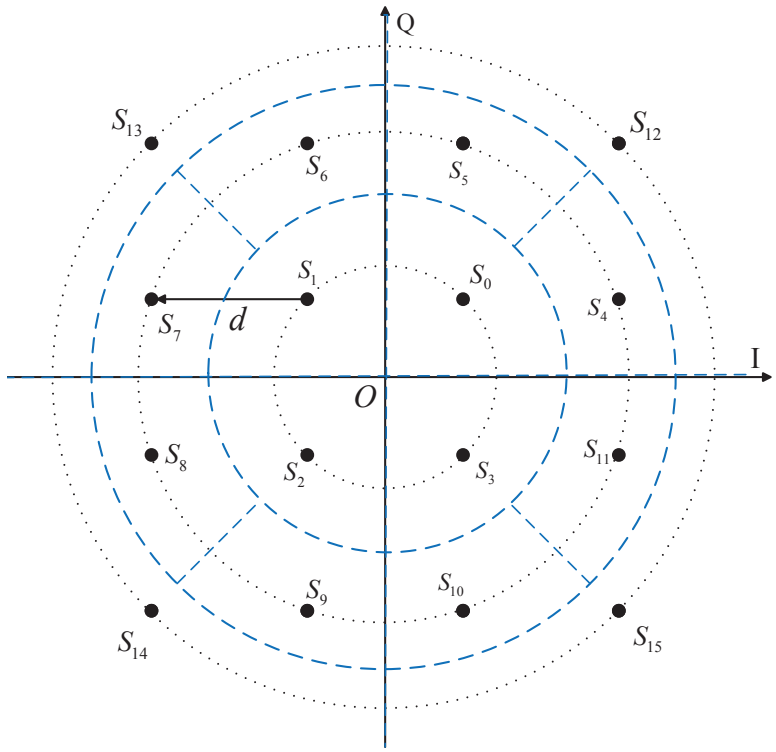

Figure 4.15: 16QAM with AS decision regions.

4.3 New SEP Results for the AS Detector

In this section, we will derive the approximate and closed-form SEP expression of 8-point star QAM with the suboptimal AS detector $\widehat{S}_{AS}$ in (3.11) in strong phase noise. Here, $\widehat{S}_{AS}$ leads to the circular DB between rings whose radius is $r_{th} = \frac{a_1+a_2}{2}$ and the annular sectors as decision regions. We generalize our approach to obtain the SEP results for higher-order modulations, such as 16QAM and (4,4,8)-16APSK using $\widehat{S}_{AS}$ in (3.12). All the SEP results are expressed in terms of Gaussian Q-function $Q(.)$. The constellation maps for 8-point star QAM and 16QAM with $\widehat{S}_{AS}$ are shown earlier in Figs. 3.2 and 3.6, respectively. Fig. 4.15 shows the 16QAM constellation with circular DB and AS decision regions.

Conditioned on $S_i = A_i e^{j\phi_i}$ being sent, the simplified joint pdf (3.7) in conjunction with (3.1) shows that the distribution of $|r|$ and the conditional pdf

of $\angle r$ can be expressed, respectively, as

$$p(|r| \mid S_i) \approx \sqrt{\frac{|r|}{\pi N_0 A_i}} \exp[-\frac{(|r| - A_i)^2}{N_0}] \tag{4.24}$$

and

$$p(\angle r \mid |r|, S_i) \approx \frac{\exp\left[-\frac{(\angle r - \phi_i)^2}{2(\frac{N_0}{2A_i|r|} + \sigma_{\tilde{\theta}}^2)}\right]}{\sqrt{2\pi(\frac{N_0}{2A_i|r|} + \sigma_{\tilde{\theta}}^2)}}. \tag{4.25}$$

Here, $\angle r$ is conditionally Gaussian distributed with mean ϕ_i and variance $\frac{N_0}{2A_i|r|} + \sigma_{\tilde{\theta}}^2$, which depends on $|r|$. For high SNR, i.e., $\gamma \gg 1$, we can have $|r| \approx A_i$ given S_i transmitted. Therefore, (4.24) simplifies to

$$p(|r| \mid S_i) \approx \frac{1}{\sqrt{N_0 \pi}} \exp[-\frac{(|r| - A_i)^2}{N_0}] \tag{4.26}$$

which is a Gaussian pdf with mean A_i and variance $N_0/2$, and (4.25) reduces to

$$p(\angle r \mid S_i) \approx \frac{\exp\left[-\frac{(\angle r - \phi_i)^2}{2(\frac{N_0}{2A_i^2} + \sigma_{\tilde{\theta}}^2)}\right]}{\sqrt{2\pi(\frac{N_0}{2A_i^2} + \sigma_{\tilde{\theta}}^2)}}. \tag{4.27}$$

Thus, we have $\angle r \sim N(\phi_i,\ \frac{N_0}{2A_i^2} + \sigma_{\tilde{\theta}}^2)$, which leads to the Gaussian AOPN+PRE model introduced in Chap. 2, i.e., $\varrho \sim N(0,\ \frac{N_0}{2A_i^2} + \sigma_{\tilde{\theta}}^2)$ which is independent of $|r|$. We observe from (4.26) and (4.27) that $\angle r$ and ϱ become asymptotically independent of $|r|$ for high SNR.

4.3.1 8-star QAM and the Rotated Case

For 8-star QAM, we have $P(c_s|S_i) = P(c_s|S_0)$ for $i = 1, 2, 3$, and $P(c_s|S_i) = P(c_s|S_4)$ for $i = 5, 6, 7$. Thus we only consider $P(c_s|S_0)$ and $P(c_s|S_4)$. As Fig. 3.2(a) shows, $P(c_s|S_0)$ is the probability of the received signal phasor r falling in

the decision region R_0 given S_0 is sent, i.e.,

$$P(c_s \mid S_0) = P(r \in R_0 \mid S_0) = P(0 \leq |r| \leq r_{th}, -\frac{\pi}{4} \leq \varrho \leq \frac{\pi}{4} \mid S_0).$$

Similarly, we have

$$P(c_s \mid S_4) = P(r \in R_4 \mid S_4) = P(r_{th} < |r| < \infty, -\frac{\pi}{4} \leq \varrho \leq \frac{\pi}{4} \mid S_4).$$

For high SNR when circular DB between rings occurs, the event of $\{-\frac{\pi}{4} \leq \varrho \leq \frac{\pi}{4}\}$ is independent of $|r|$, since ϱ and $|r|$ are independent as shown above. It thus follows that we have

$$P(c_s|S_0) = P(0 \leq |r| \leq r_{th} \mid S_0)P(-\frac{\pi}{4} \leq \varrho \leq \frac{\pi}{4} \mid S_0)$$

and

$$P(c_s|S_4) = P(r_{th} < |r| < \infty \mid S_4)P(-\frac{\pi}{4} \leq \varrho \leq \frac{\pi}{4} \mid S_4). \tag{4.28}$$

Since we have $\varrho \sim N(0,\ \frac{N_0}{2a_1^2} + \sigma_{\tilde{\theta}}^2)$ given S_0 is sent, and $\varrho \sim N(0,\ \frac{N_0}{2a_2^2} + \sigma_{\tilde{\theta}}^2)$ given S_4 is sent, and according to (4.1), we thus have

$$P(-\frac{\pi}{4} \leq \varrho \leq \frac{\pi}{4}|S_0) = 1 - 2Q\left(\frac{\pi}{4}\frac{1}{\sqrt{\frac{N_0}{2{a_1}^2} + \sigma_{\tilde{\theta}}^2}}\right)$$

and

$$P(-\frac{\pi}{4} \leq \varrho \leq \frac{\pi}{4}|S_4) = 1 - 2Q\left(\frac{\pi}{4}\frac{1}{\sqrt{\frac{N_0}{2{a_2}^2} + \sigma_{\tilde{\theta}}^2}}\right) \tag{4.29}$$

Similarly, using (4.26), we have

$$P(0 \leq |r| \leq r_{th} \mid S_0) = Q\left(\frac{-a_1}{\sqrt{N_0/2}}\right) - Q\left(\frac{r_{th} - a_1}{\sqrt{N_0/2}}\right)$$

and

$$P(r_{th} < |r| < \infty \mid S_4) = Q\left(\frac{r_{th} - a_2}{\sqrt{N_0/2}}\right). \tag{4.30}$$

Finally, the SEP for 8-star QAM with the AS detector is

$$P(e_s) = 1 - \frac{1}{2}[P(c_s|S_0) + P(c_s|S_4)]. \tag{4.31}$$

Here, (4.28) in conjunction with (4.29) and (4.30) give $P(c_s|S_0)$ and $P(c_s|S_4)$ as, respectively,

$$P(c_s|S_0) \approx \left[1 - 2Q\left(\frac{\pi}{4}\frac{1}{\sqrt{\frac{N_0}{2{a_1}^2} + \sigma_{\tilde{\theta}}^2}}\right)\right] \times \left[Q\left(\frac{-a_1}{\sqrt{N_0/2}}\right) - Q\left(\frac{r_{th} - a_1}{\sqrt{N_0/2}}\right)\right]$$

and

$$P(c_s|S_4) \approx \left[1 - 2Q\left(\frac{\pi}{4}\frac{1}{\sqrt{\frac{N_0}{2{a_2}^2} + \sigma_{\tilde{\theta}}^2}}\right)\right] Q\left(\frac{r_{th} - a_2}{\sqrt{N_0/2}}\right).$$

It should be noted that due to exploiting the detector $\widehat{S}_{AS}$ and using our AOPN+PRE model to calculate the probability of $\angle r$ falling in the correct decision region, any phase offset between the signal points on two different rings does not change the performance of the system. Thus, (4.31) is also the approximate SEP expression for rotated 8-star QAM with AS decision regions in Fig. 3.2(b). The result (4.31) is our new explicit, closed-form SEP expression, which provides insight into how the parameters β, $\sigma_{\tilde{\theta}}^2$ and γ affect the SEP performance. It allows engineers to make a quick estimation of the performance for high SNR or large $\sigma_{\tilde{\theta}}^2$.

Using (4.31), we can predict the error floor, i.e., the irreducible SEP due to a non-zero PRE variance $\sigma_{\tilde{\theta}}^2$. That is, as $\gamma \gg (\sigma_{\tilde{\theta}}^2)^{-1}$ or $N_0 \to 0$, (4.31) reduces to $2Q(\frac{\pi}{4\sqrt{\sigma_{\tilde{\theta}}^2}})$ and increases as $\sigma_{\tilde{\theta}}^2$ increases. For DA ML PE, the error floor is mainly due to the combined normalized laser linewidth ($\sigma_p^2 = 2\pi(\Delta v)T$), since we have

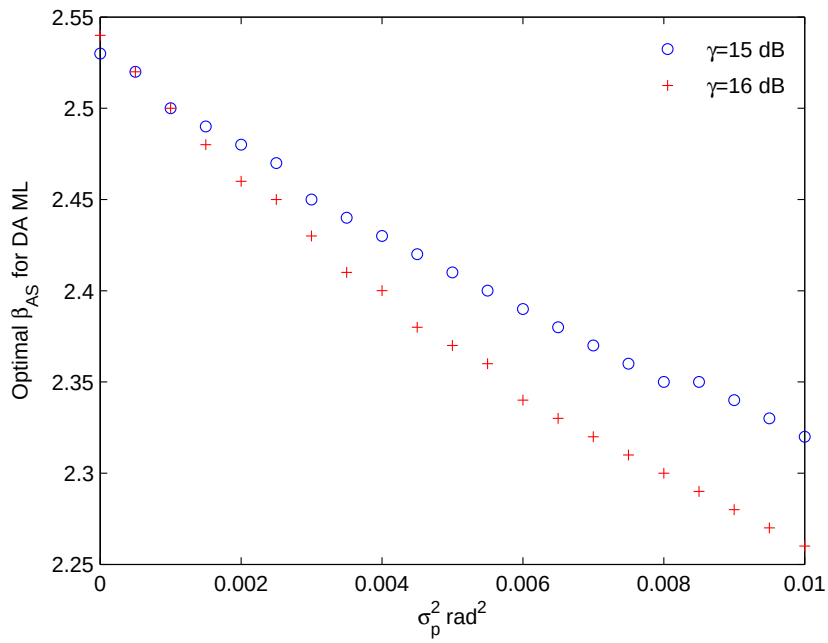

Figure 4.16: Optimal β_{AS} for 8-point star QAM using $\widehat{S}_{AS}$ with DA ML ($L = 8$) as σ_p^2 increases given $\gamma = 15$ and 16dB.

$\sigma_{\tilde{\theta}}^2|_{\gamma\to\infty} = \frac{2L^2+3L+1}{6L}\sigma_p^2$.

Our result (4.31) allows us to plot the figure of $P(e_s)$ against the ring ratio β, and directly find the optimal ring ratio denoted as β_{AS} for minimum SEP of $\widehat{S}_{AS}$. The value of β_{AS} depends on two parameters: γ and $\sigma_{\tilde{\theta}}^2$. As Fig. 4.16 shows, using DA ML with a fixed SNR $\gamma = 15$ and 16dB, respectively, the optimum β_{AS} varies from 2.55 to 2.25, as σ_p^2 (rad^2) increases from 0 to 0.01. Thus, this result can be used to facilitate constellation optimization in the presence of laser phase noise.

4.3.2 General M-ary APSK

Due to using circular DB between rings, different values of the relative phase shift ψ_k on the kth ring have no effect on the SEP result of general M-APSK. Based on the results (4.26)-(4.31), the closed-form SEP expression of M-APSK with the

detector $\widehat{S}_{AS}$ is obtained as

$$\begin{aligned} P(e_s) &= 1 - \sum_{k=1}^{N} \frac{l_k}{M} P(c_s|S_{k\text{th-ring}}) = 1 - \sum_{k=1}^{N} \frac{l_k}{M} \times \\ & P(\frac{a_{k-1}+a_k}{2} \le |r| < \frac{a_{k+1}+a_k}{2}) P(-\frac{\pi}{l_k} \le \varrho \le \frac{\pi}{l_k}) \\ &\approx 1 - \sum_{k=1}^{N} \frac{l_k}{M} \left[1 - 2Q\left(\frac{\pi}{l_k} \frac{1}{\sqrt{\frac{N_0}{2{a_k}^2} + \sigma_{\tilde{\theta}}^2}} \right) \right] \times \\ & \left[Q\left(\frac{a_{k-1}-a_k}{\sqrt{2N_0}} \right) - Q\left(\frac{a_{k+1}-a_k}{\sqrt{2N_0}} \right) \right]. \end{aligned} \tag{4.32}$$

Here, $P(c_s|S_{k\text{th-ring}})$ represents the correct-decision probability conditioned on any symbol on the kth ring being sent, and we have $a_0 = -a_1$ and $a_{N+1} = \infty$ for the signal points on the innermost and outermost rings, respectively. For $l_1 = 1$, the point on the first ring is always placed at the origin, implying that we have $a_1 = 0$ and $P(-\frac{\pi}{l_1} \le \varrho \le \frac{\pi}{l_1}) = 1$ in (4.32) here.

Noteworthily, as 8-star QAM illustrates, for the special structure of M-APSK which has the same values of l_k and θ_k for any k, e.g., (4,4,4,4)-16APSK, (4.32) is also a good approximation to the exact SEP of the ML detector through the whole SNR region of interest.

Moreover, we can easily predict the error floor for any M-APSK constellation using the $\widehat{S}_{AS}$ detector. As $\gamma \gg (\sigma_{\tilde{\theta}}^2)^{-1}$ or $N_0 \to 0$ in (4.32), the error floor P_{EF} is deduced to be

$$P_{EF} = \lim_{\gamma \to \infty} P(e_s) \approx 2 \sum_{k=1}^{N} \frac{l_k}{M} Q\left(\frac{\pi}{l_k} \frac{1}{\sqrt{\sigma_{\tilde{\theta}}^2}} \right) \tag{4.33}$$

which depends on $\boldsymbol{l} \equiv (l_1, \cdots, l_N)$ and increases as $\sigma_{\tilde{\theta}}^2$ increases.

Here, a (4,4,8)-16APSK constellation with uniformly-spaced ring radii, i.e., $\{S_i = \frac{\bar{d}}{2} e^{j(\frac{\pi i}{2} + \frac{\pi}{4})}$ for $i = 0, 1, 2, 3$; $\bar{d} e^{j(\frac{\pi(i-4)}{2} + \frac{\pi}{4})}$ for $i = 4, 5, 6, 7$; and $\frac{3\bar{d}}{2} e^{j(\frac{\pi(i-8)}{4} + \frac{\pi}{8})}$ for $i = 8, 9 ... 15\}$ with $\bar{d} = \sqrt{\frac{16E_s}{23}}$, as shown in Fig. 3.6, is used as an example for numerical illustration. For (4,4,8)-16APSK using $\widehat{S}_{AS}$, the error floor above reduces

to $Q(\frac{\pi}{4\sqrt{\sigma_{\tilde{\theta}}^2}}) + Q(\frac{\pi}{8\sqrt{\sigma_{\tilde{\theta}}^2}})$.

4.3.3 16QAM

For 16QAM, the derivation of the SEP result is very similar to that for M-APSK, except for the middle ring where the eight points are not uniformly spaced. For the signal points on the middle ring of 16QAM, the probability of falling in the correct angular region should be $P(-\nu \leq \varrho \leq \frac{\pi}{4} - \nu)$ instead of $P(-\frac{\pi}{4} \leq \varrho \leq \frac{\pi}{4})$ in (4.32) for (4,4,8)-16APSK. Therefore, the SEP result of 16QAM using $\widehat{S}_{AS}$ is obtained as

$$P(e_s) = 1 - \sum_{k=1}^{3} \frac{l_k}{M} P(c_s|S_{k\text{th-ring}}) \approx 1 - \sum_{k=1,3} \frac{1}{4} \left[1 - 2Q\left(\frac{\pi}{4} \frac{1}{\sqrt{\frac{N_0}{2{a_k}^2} + \sigma_{\tilde{\theta}}^2}} \right) \right] \times \left[Q\left(\frac{a_{k-1} - a_k}{\sqrt{2N_0}} \right) - Q\left(\frac{a_{k+1} - a_k}{\sqrt{2N_0}} \right) \right] - \frac{1}{2} \left[Q\left(\frac{-\nu}{\sqrt{\frac{N_0}{2{a_2}^2} + \sigma_{\tilde{\theta}}^2}} \right) - Q\left(\frac{\frac{\pi}{4} - \nu}{\sqrt{\frac{N_0}{2{a_2}^2} + \sigma_{\tilde{\theta}}^2}} \right) \right] \times \left[Q\left(\frac{a_1 - a_2}{\sqrt{2N_0}} \right) - Q\left(\frac{a_3 - a_2}{\sqrt{2N_0}} \right) \right]. \tag{4.34}$$

Here, we have $a_1 = -a_0 = \frac{d}{\sqrt{2}}$, $a_2 = \frac{\sqrt{10}d}{2}$, $a_3 = \frac{3d}{\sqrt{2}}$ and $a_4 = \infty$, respectively. As $N_0 \to 0$ in (4.34), the error floor for $\widehat{S}_{AS}$ of 16QAM in phase noise is thus derived as

$$P_{EF} \approx Q\left(\frac{\pi}{4\sqrt{\sigma_{\tilde{\theta}}^2}} \right) + \frac{1}{2} \left[Q\left(\frac{\nu}{\sqrt{\sigma_{\tilde{\theta}}^2}} \right) + Q\left(\frac{\pi/4 - \nu}{\sqrt{\sigma_{\tilde{\theta}}^2}} \right) \right].$$

4.3.4 Numerical Results

Using DA ML with $L = 8$, Fig. 4.17 shows numerically that $P_{EF} = 2Q(\frac{\pi}{4\sqrt{\sigma_{\tilde{\theta}}^2}})$ is a good approximation to the simulation results of the error floor of $\widehat{S}_{AS}$ for both 8-star QAM and rotated 8-star QAM, as σ_p^2 increases from 5×10^{-3} to 2.2×10^{-2}(rad^2). Comparing $\widehat{S}_{MED}$ with the $\widehat{S}_{AS}$ in (3.11), we can see that for rotated 8-star QAM, the error floor of $\widehat{S}_{MED}$ using straight-line DB is much larger

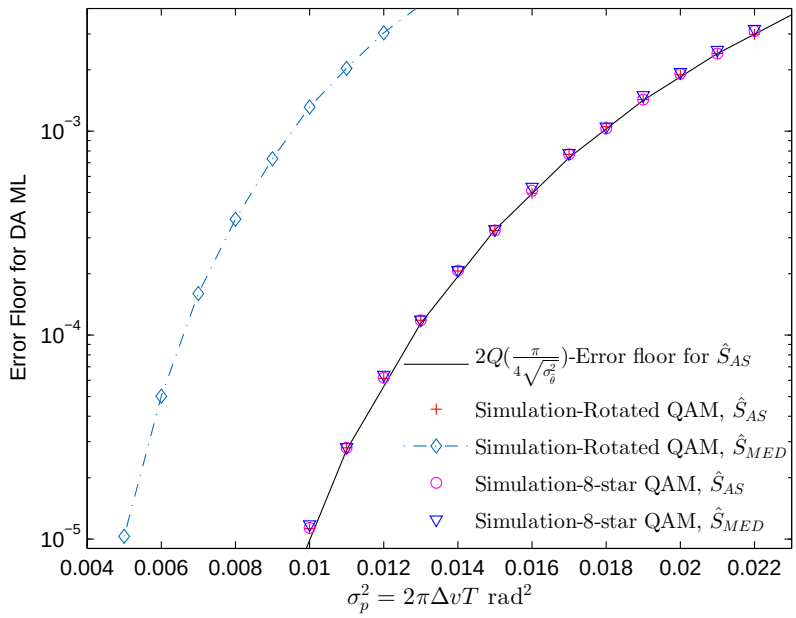

Figure 4.17: Error floor comparison as a function of $\sigma_p^2 = 2\pi(\Delta v)T$ for 8-point star QAM with DA ML PE ($L = 8$).

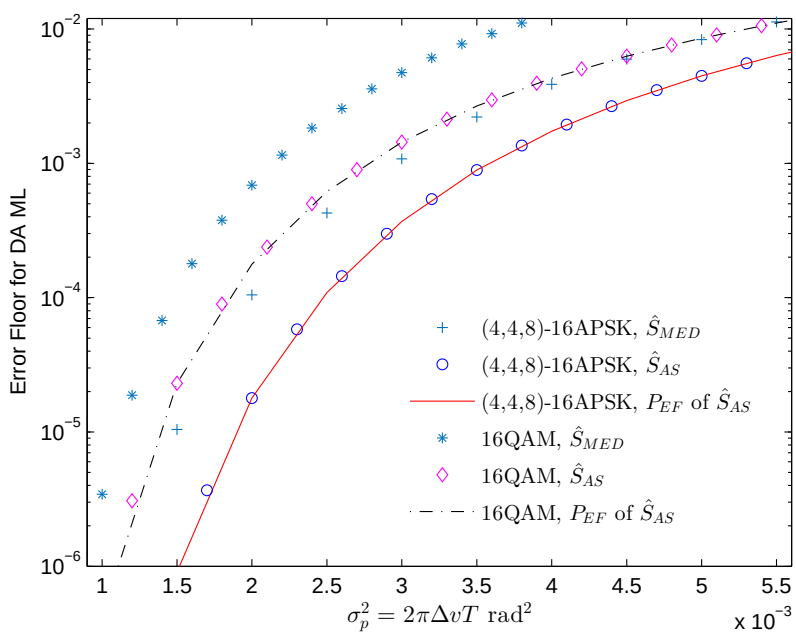

Figure 4.18: Error floor comparison as a function of $\sigma_p^2 = 2\pi(\Delta v)T$ for 16QAM and (4,4,8)-16APSK with DA ML PE ($L = 12$).

than that of $\widehat{S}_{AS}$ using circular DB between rings. Whereas, for 8-star QAM, $\widehat{S}_{MED}$ and $\widehat{S}_{AS}$ have almost the same error floor. These can be explained from Figs. 4.1 and 3.5 where the decision regions for the circular DB of $\widehat{S}_{AS}$ differ much more from those for the straight-line DB of $\widehat{S}_{MED}$ for the rotated case, but differ less for 8-star QAM.

Fig. 4.18 shows numerically that the approximations to the error floor of $\widehat{S}_{AS}$ for both (4,4,8)-16APSK and 16QAM are very accurate. It can be seen that for both 16-point constellations using DA ML PE with $L = 12$, $\widehat{S}_{AS}$ is much more robust to the increased combined normalized laser linewidth than $\widehat{S}_{MED}$, as σ_p^2 increases from 10^{-3} to 5.5×10^{-3}(rad^2). For a 40Gbit/s system, this range of σ_p^2 corresponds to the combined laser linewidth Δv ranging from 1.6MHz to 8MHz. Moreover, (4,4,8)-16APSK has a much larger laser linewidth tolerance than 16QAM, for high SNR.

Here, (4,4R,8)-16APSK and (4,4,4,4)-16APSK constellations with uniformly-spaced ring radii are also included as examples for numerical illustration. As shown in Fig. 5.1(a) in Chap. 5.2, the (4,4R,8)-16APSK signal set is $\{S_i = \frac{\bar{d}}{2}e^{j(\frac{\pi i}{2}+\frac{\pi}{4})}$ for $i = 0,1,2,3$; $\bar{d}e^{j(\frac{\pi(i-4)}{2})}$ for $i = 4,5,6,7$; and $\frac{3\bar{d}}{2}e^{j(\frac{\pi(i-8)}{4}+\frac{\pi}{8})}$ for $i = 8,9...15\}$ with $\bar{d} = \sqrt{\frac{16E_s}{23}}$. As shown in Fig. 5.1(b), the (4,4,4,4)-16APSK signal set is $\{S_i = \frac{d}{2}e^{j(\frac{\pi i}{2})}$ for $i = 0,1,2,3$; $de^{j(\frac{\pi(i-4)}{2})}$ for $i = 4,5,6,7$; $\frac{3d}{2}e^{j(\frac{\pi(i-8)}{2})}$ for $i = 8,9,10,11$; and $2de^{j(\frac{\pi(i-12)}{2})}$ for $i = 12,13,14,15\}$ with $d = \sqrt{\frac{8E_s}{15}}$. For (4,4R,8)-16APSK, the error floor is $P_{EF} = Q(\frac{\pi}{4\sqrt{\sigma^2}}) + Q(\frac{\pi}{8\sqrt{\sigma^2}})$. For (4,4,4,4)-16APSK, (4.33) reduces to $P_{EF} = 2Q(\frac{\pi}{4\sqrt{\sigma^2}})$. Fig. 4.19 shows that (4.33) is a good approximation to the simulation results of the error floor of $\widehat{S}_{AS}$ for any M-APSK with any $\sigma_{\tilde{\theta}}^2$.

Next, we will show that (4.32) and (4.34) are very accurate results for the SEP of our detector $\widehat{S}_{AS}$. In the ideal case of no past decision errors for any PE algorithm, the lower bound on the PRE variance $\sigma_{\tilde{\theta}}^2$ given by the Cramer-Rao bound (CRB) is $\sigma_{\tilde{\theta}}^2 \geq \sigma_{CR}^2 = \frac{1}{2\gamma}\frac{B}{W}$, where σ_{CR}^2 is the linearized variance of the ML PE of an unmodulated carrier [45,108]. Here, we have $B = (LT)^{-1}$ is the estimator

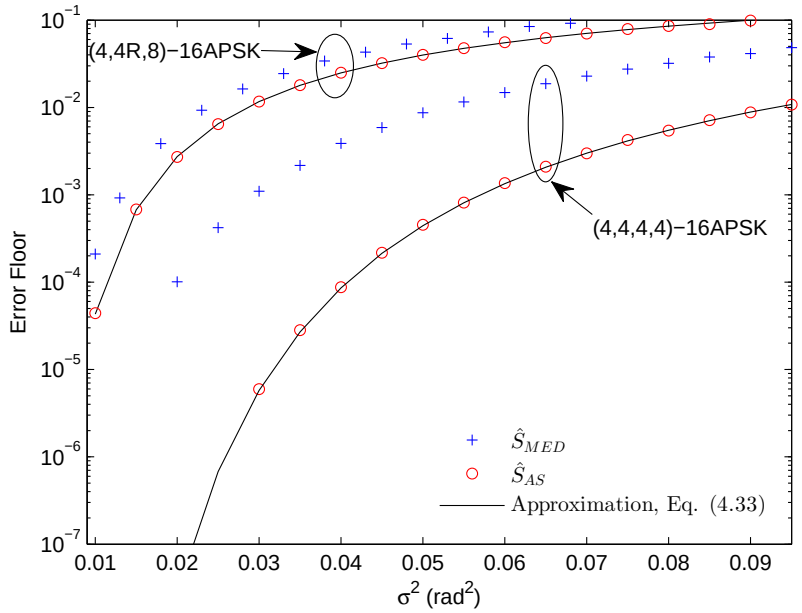

Figure 4.19: Error floor comparison between $\widehat{S}_{AS}$ and $\widehat{S}_{MED}$ for (4,4R,8)-16APSK and (4,4,4,4)-16APSK.

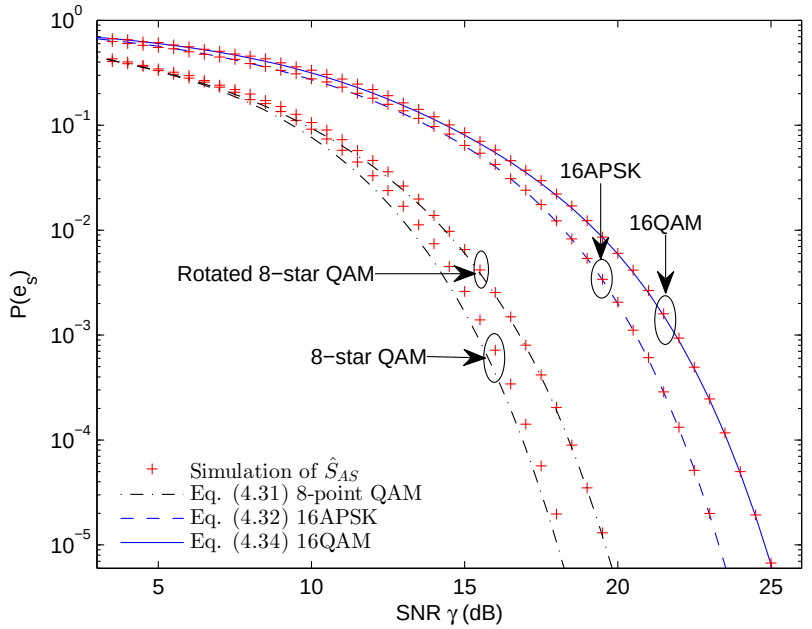

Figure 4.20: Comparison between simulated $\widehat{S}_{AS}$ and (4.31)-(4.34) with $\sigma^2_{\tilde{\theta}} = \sigma^2_{CR} = \frac{1}{2\gamma L}$.

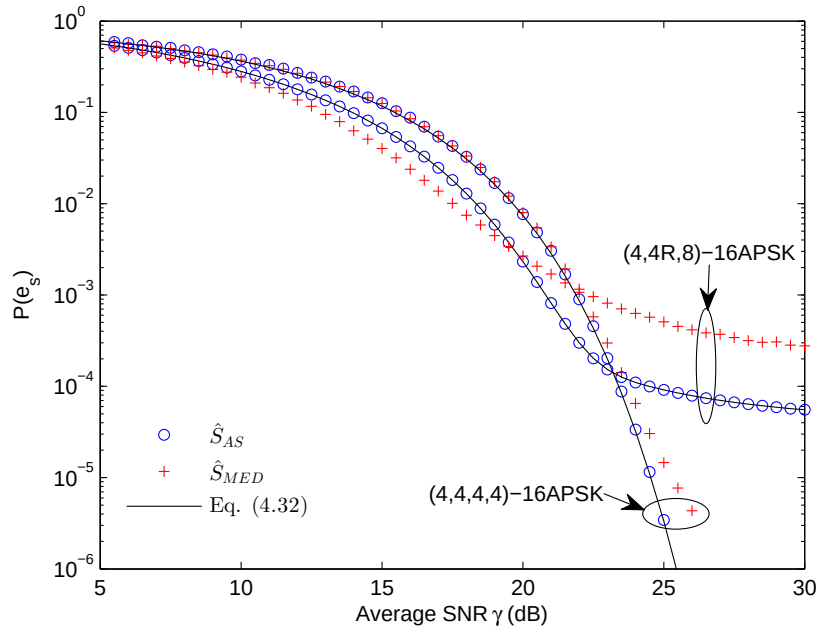

Figure 4.21: SEP comparison between $\widehat{S}_{AS}$ and $\widehat{S}_{MED}$ with $\sigma_{\tilde{\theta}}^2 = 0.01\text{rad}^2$.

bandwidth with L as the averaging memory length, and $W = T^{-1}$ is the message bandwidth. This CRB value corresponds to the case of no laser phase noise, i.e., $\sigma_p^2 = 0$ in DA ML PE where we thus have $\sigma_{\tilde{\theta}}^2 = \sigma_{CR}^2 = \frac{1}{2\gamma L}$. This is the minimum value of $\sigma_{\tilde{\theta}}^2$ to expect in DA ML PE, which is used here. One should know that this CRB value is the lower bound on $\sigma_{\tilde{\theta}}^2$ for any carrier recovery scheme. As Fig. 4.20 shows, our approximate SEP results (4.31), (4.32) and (4.34) agree very well with the simulation results for the SEP of our detector $\widehat{S}_{AS}$ for all SNR values of interest, which validates their accuracy within a wide range of $\sigma_{\tilde{\theta}}^2$ in practice. Moreover, Fig. 4.21 shows that our SEP result (4.32) agrees very well with the simulated SEP results of $\widehat{S}_{AS}$ for all SNR values of interest, which validates its accuracy for any M-APSK. Once again, Fig. 4.21 shows that $\widehat{S}_{AS}$ performs better than $\widehat{S}_{MED}$ as γ increases.

4.4 Concluding Remarks

Using the additive observation phase noise (AOPN) model, we converted the AWGN into an equivalent phase noise. This conversion leads to the new AOPN+PRE/AOPN+RPN model, which facilitates computing the SEP/BEP of MPSK/MDPSK. The AOPN+PRE model further leads to a simple and accurate error performance analysis for M-QAM and M-APSK with the annular-sector detector $\widehat{S}_{AS}$. All the SEP results for $\widehat{S}_{AS}$ are derived in terms of Gaussian Q-function $Q(.)$, which makes the performance analysis more straightforward.

Our new expressions offer quick and accurate predictions of the error performance with respect to different phase noise variances or different combined laser linewidths. Our approach can be further used to analyze the error performance of other complex phase modulation schemes.

Appendix A

We consider perfectly coherent 8-star QAM and rotated 8-star QAM in the pure AWGN channel, i.e., with $\sigma_{\tilde{\theta}}^2$ known to be zero. Their exact SEP expressions can be easily derived by using the polar coordinates method in [71].

Using this approach, the exact SEP of 8-star QAM is given by

$$\begin{aligned} P(e_s) = & \frac{1}{\pi}\int_0^{\vartheta} \exp\left[\frac{-\gamma(\beta-1)^2}{2(\beta^2+1)\cos^2\theta}\right] d\theta \\ & + \frac{1}{2\pi}\left(\int_{\vartheta}^{\pi} \exp\left[\frac{-\gamma}{(\beta^2+1)\sin^2(\theta-\frac{\pi}{4})}\right] d\theta + \int_{\frac{\pi}{4}}^{\pi-\vartheta} \exp\left[\frac{-\gamma\sin^2(\frac{\pi}{4}+\vartheta)}{\sin^2(\theta-\frac{\pi}{4})}\right] d\theta\right) \end{aligned} \tag{4.35}$$

where we have $\vartheta = \arctan(\frac{\beta+1}{\beta-1})$.

Similarly, the SEP of rotated 8-star QAM is shown to be

$$
\begin{aligned}
P(e_s|S_0) &= \frac{1}{\pi}\int_0^{2\varphi+\frac{\pi}{4}} e^{-e^2\alpha^2\gamma}dt + \frac{1}{\pi}\int_{2\varphi+\frac{\pi}{4}}^{\pi} e^{-b^2\alpha^2\gamma}dt, \\
P(e_s|S_4) &= \frac{1}{\pi}\int_{\frac{\pi}{4}}^{\frac{3\pi}{4}-2\varphi} e^{-c^2\alpha^2\gamma}dt + \frac{1}{\pi}\int_{\frac{3\pi}{4}-2\varphi}^{\pi} e^{-d^2\alpha^2\gamma}dt, \\
P(e_s) &= \frac{1}{2}(P(e_s|S_0) + P(e_s|S_4)).
\end{aligned} \tag{4.36}
$$

Here, we have $\varphi = \arctan(\frac{1}{\sqrt{2}\beta-1})$ and

$$
\begin{aligned}
e &= \frac{\cos\varphi}{\sqrt{2}\sin(2\varphi)\sin(\frac{\pi}{4}+t-\varphi)}, \quad b = \frac{1}{\sqrt{2}\sin(t-\frac{\pi}{4})}, \\
c &= \frac{\sqrt{(\beta-\frac{1}{\sqrt{2}})^2+\frac{1}{2}}\cos(2\varphi)}{2\cos(\varphi+\frac{\pi}{4})\sin(t-\frac{\pi}{4})}, \ d = \frac{\sqrt{(\beta-\frac{1}{\sqrt{2}})^2+\frac{1}{2}}}{2\cos(t+\varphi)}.
\end{aligned}
$$

By plotting $P(e_s)$ against the ring ratio β using these results, we directly find the optimal ring ratios for minimum SEP, which are denoted as β^r_{MED} and β_{MED} for rotated 8-star QAM and 8-star QAM, respectively. We have $\beta^r_{MED} \approx 2$ and $\beta_{MED} \approx 2.4$ within a large range of γ (from about 8dB to about 30dB). As Fig. 4.22 shows, with the optimal ring ratios β^r_{MED} and β_{MED}, respectively, rotated 8-star QAM outperforms 8-star QAM in pure AWGN. Our SEP expressions match with the simulation results for the SEP of $\widehat{S}_{aML1}$ with $\sigma^2_{\tilde{\theta}} = 0$.

Appendix B

To explicitly explain when the approximations are good, we alternatively show the comparison of relative error which is defined as $\mid Approximation - Exact \mid /Exact$ in [69]. Figs. 4.23(a) and 4.23(b) show the relative error for MDPSK with $\sigma^2_p = 10^{-3}\text{rad}^2$, which correspond to Figs. 4.10 and 4.13, respectively. Both figures show that the relative error for $M = 16$ is the smallest for a wide range of SNR. For high order modulations, the magnitude of relative error is below 10^{-1}, implying that the approximation is good.

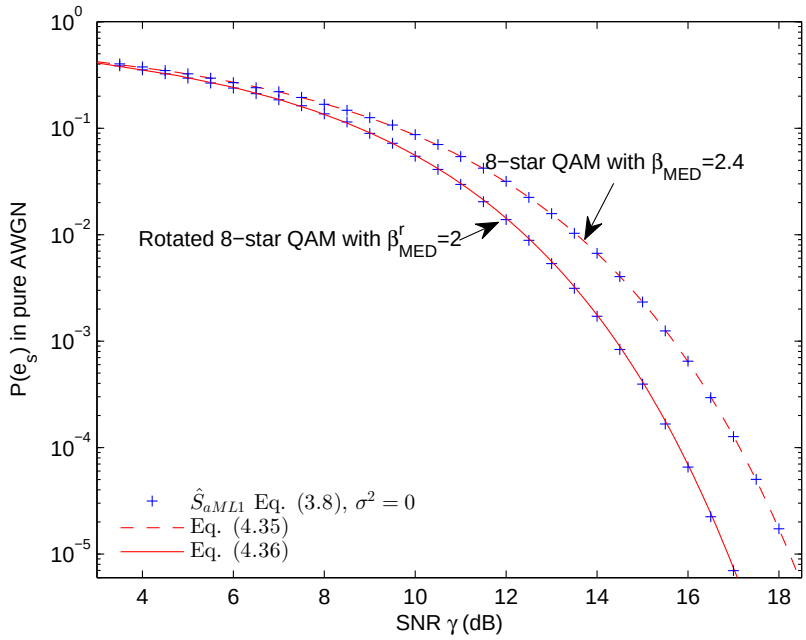

Figure 4.22: Comparision among (4.35), (4.36) and simulated SEP of $\widehat{S}_{aML1}$ with $\sigma_{\tilde{\theta}}^2 = 0$ for 8-point star QAM with optimal β.

The approximations are increasingly more accurate as M increases, since constellations with larger M require higher SNR to achieve the same error probability, as Tables 4.1-4.3 have implied.

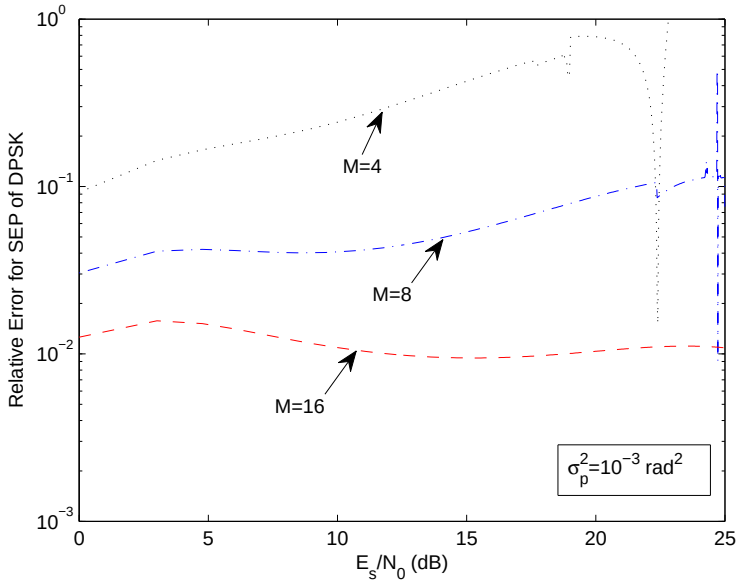

(a)

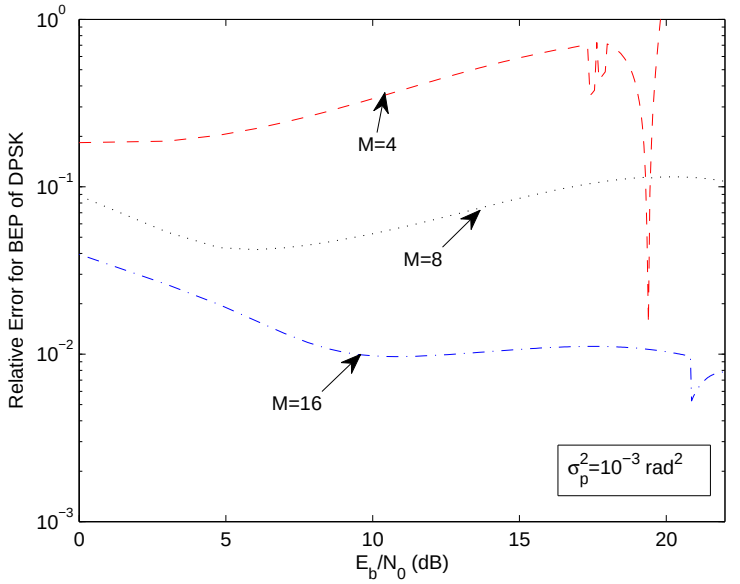

(b)

Figure 4.23: Comparison of relative error for MDPSK with $\sigma_p^2 = 10^{-3}\text{rad}^2$: (a) SEP, (b) BEP.

Chapter 5

Constellation Optimization in Phase Noise

To improve the performance of communication systems with phase reference error (PRE), in this chapter, we address the problem of optimizing signal constellations for the linear phase noise channel [109–111]. Two optimization formulations are proposed by minimizing the error probability, which provide an analytical framework for constellation design. In the first formulation, we seek to design constellations that minimize the SEP of the approximate ML detectors we derived in Chap.3. However, this requires extensive simulations, and thus, this is not efficient. In the second formulation, we optimize constellations in terms of our SEP results for the annular-sector (AS) detector given in Chap.4, which can be achieved by numerical computation and search. These formulations can be used to systematically optimize any multiple-ring constellations in laser phase noise. For simplicity, M-APSK optimization is considered by using the second formulation as an illustration example.

In Section 5.1, the two optimization formulations are introduced. Section 5.2 specifically provides M-APSK optimization, and examples of ring radii optimization are given.

5.1 Optimization Formulations

In this section, we present the optimization formulations by minimizing the SEP $P(e_s)$, to design constellations of order M based on the received signal model (2.3). The comparison of different constellations is based on the same average energy per symbol E_s. That is, we have one constraint given by $\sum_{i=1}^{M} A_i^2 = ME_s$.

Observe that given the signal $S_i = A_i e^{j\phi_i}$ transmitted, the additive observation phase noise (AOPN) ϵ induced by the AWGN n has the variance $\frac{N_0}{2A_i^2}$, which implies that the AWGN has less phase rotation effect on the outer-ring signals because of the larger A_i. Therefore, to reduce the AOPN effect in phase noise, we should intuitively put more signal points on the outer ring compared to those on the adjacent inner ring. Thus, in the following formulations, we will always add an additional constraint, i.e., $l_1 \leq l_2 \leq \cdots \leq l_N$, where N is the number of signal rings in multiple-ring constellations and l_k is the number of signal points on the kth ring. This is a tendency that l_k should increase with k, which guarantees a better performance in phase noise. However, from this constraint, we cannot determine how large the difference between l_k and l_{k-1} should be for a given N. That is, as shown later, the best value of $(l_k - l_{k-1})$ cannot be decided, and it depends on the PRE variance $\sigma_{\tilde{\theta}}^2$ and the SNR per symbol γ.

5.1.1 Approximate ML Formulation

In the first formulation, we aim to design constellations that minimize the SEP of the approximately optimum detectors (3.8), (3.9) and (3.10) proposed in Chap.3, for a fixed average energy E_s and a given PRE variance $\sigma_{\tilde{\theta}}^2$. The optimization problem is posed as follows:

$$\begin{aligned} \underset{\{S_i\}}{\text{minimize}} \quad & P(e_s) \text{ of Detectors Eqs. (3.8), (3.9) and (3.10)} \\ \text{subject to} \quad & \sum_{i=1}^{M} A_i^2 = ME_s \\ & 1 \leq l_1 \leq l_2 \leq \cdots \leq l_N \end{aligned} \tag{5.1}$$

By solving (5.1), we can get the most suitable signal set $\{S_i, i = 0, 1, ..., M-1\}$ to achieve better SEP performance of the ML detector in phase noise, for any given combinations of $(E_s,\ \sigma_{\tilde{\theta}}^2)$. This added constraint avoids the unstructured and impractical constellations proposed in [53,109,111], and thus reduces the search

space size.

However, since no closed-form SEP results are given for these approximate ML detectors, extensive simulations are required to solve this problem, which is thus inefficient and costs a lot of time. Therefore, the optimization problem is simplified as follows.

5.1.2 AS Detector Formulation

We have shown in Chap. 3 that the AS detector $\widehat{S}_{AS}$ is a good approximation to the ML detector for high SNR when $\sigma_{\tilde{\theta}}^2 \neq 0$. Besides, for any multiple-ring constellations, the closed-form SEP results of the AS detector can be easily derived by using the approach in Chap. 4. Another advantage is that the AS detector does not require the information of N_0 and $\sigma_{\tilde{\theta}}^2$ to make decision, i.e., it is practically implementable. Therefore, we can formulate the optimization problem based on the AS detector instead of the ML detector.

That is, by minimizing the SEP of the AS detector (3.12), we optimize any multiple-ring constellation in strong phase noise. For a given average energy constraint E_s, the optimization problem is stated as

$$\begin{aligned} \underset{\{S_i\}}{\text{minimize}} \quad & P(e_s) \text{ of AS Detector Eq. (3.12)} \\ \text{subject to} \quad & \sum_{i=1}^{M} A_i^2 = ME_s \\ & 1 \leq l_1 \leq l_2 \leq \cdots \leq l_N \end{aligned} \tag{5.2}$$

By numerical search, the signal set $\{S_i, i = 0, 1, ..., M-1\}$ obtained is expected to be more suitable for reasonable high SNR in the memoryless phase noise channel.

Solving (5.2) which involves numerically computing the closed-form SEP results is very efficient. Next, by using this formulation, we optimize M-APSK as an example.

5.2 M-APSK Optimization

For constellation design in strong phase noise, both [53] and [109] have found via simulations that the optimized symbol points of the same energy level are separated by the largest possible angular distance, which M-APSK satisfies.

Based on earlier discussion, we add an additional constraint, i.e., $l_1 \leq \cdots \leq l_N$ where N is the number of rings, in the M-APSK optimization, compared to [53, eqs.(14)-(18)]. With the constraint $\sum_{k=1}^{N} l_k = M$ and to keep the symmetrically two-dimensional property, the maximum number of rings is thus $\frac{M}{2}$, i.e., $1 \leq N \leq \frac{M}{2}$.

One of the main contributions here is to apply our SEP result (4.32) in the M-APSK optimization. That is, conditioned on the average energy constraint E_s for a given M, the optimization problem can be formulated as:

$$\begin{aligned} \underset{N,a_k,l_k}{\text{minimize}} \quad & \text{SEP of } \widehat{S}_{AS} \text{ in } Eq.\ (4.32) \\ \text{subject to} \quad & 1 \leq N \leq \frac{M}{2}, \ \sum_{k=1}^{N} l_k = M \\ & l_1 a_1^2 + \cdots + l_N a_N^2 = M E_s \\ & 0 \leq a_1 < \cdots < a_N \\ & 1 \leq l_1 \leq \cdots \leq l_N \end{aligned} \tag{5.3}$$

The added constraint avoids the unstructured and impractical constellations, such as (1,2,1)-APSK or (3,1)-APSK in [53], and thus reduces the search space size. This optimization problem can be solved using the methods given in [53]. Next, examples of ring radii optimization for M-APSK are given.

We show one simple case here where we fix N and $\boldsymbol{l} \equiv (l_1, \cdots, l_N)$ to optimize a_k for every γ. For $M = 8$, we fix $N = 2$. Using (5.3) for different $\boldsymbol{l}$-8APSK, respectively, we can easily obtain the correspondingly optimized a_1 and a_2 for minimum SEP. We show in Fig. 5.2 that (3,5)-8APSK with the optimized a_k performs the best and (1,7)-8APSK performs the worst. As expected, the optimized (3,5)-8APSK outperforms the optimized (5,3)-8APSK, and (2,6)-8APSK

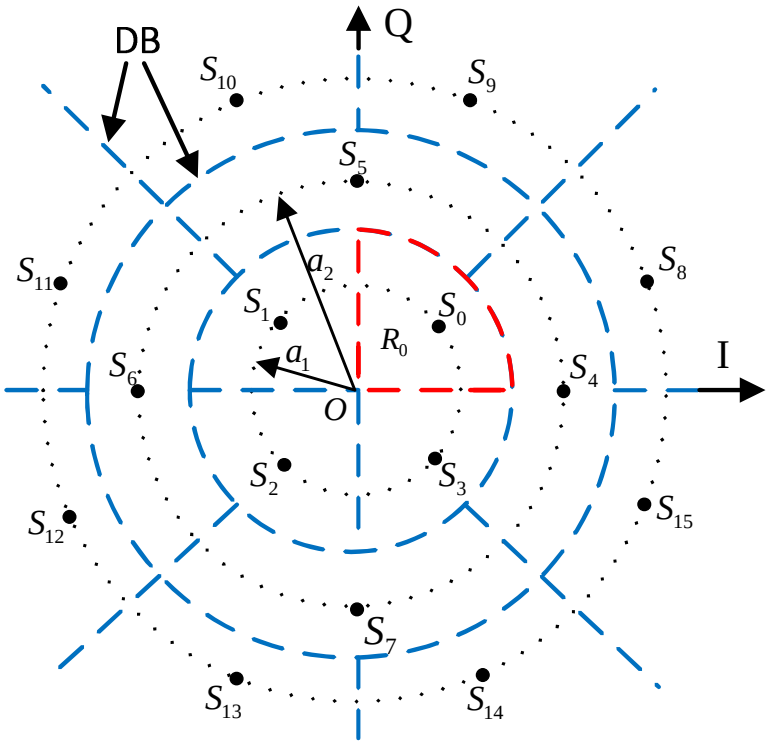

(a) (4,4R,8)-16APSK

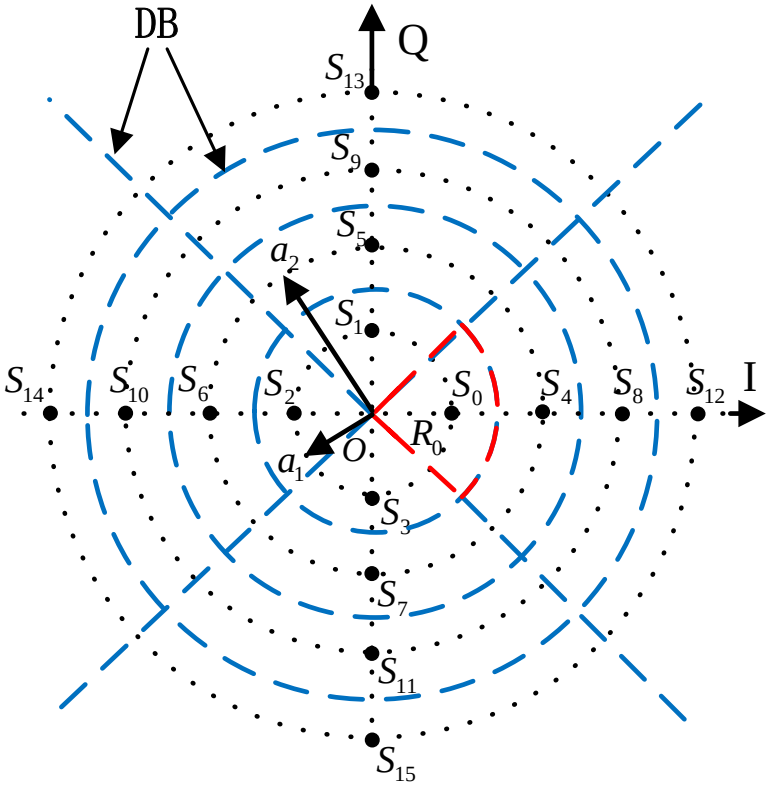

(b) (4,4,4,4)-16APSK

Figure 5.1: 16-APSK constellations with AS decision regions.

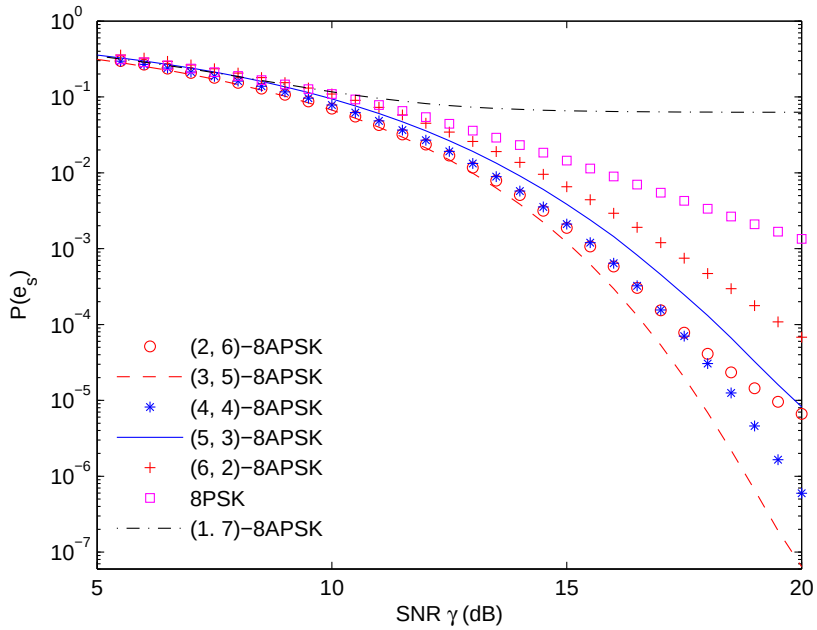

Figure 5.2: Comparison among 8-APSK constellations with optimized a_k for every γ and $\sigma_{\tilde{\theta}}^2 = 0.01\text{rad}^2$.

outperforms (6,2)-8APSK, which validates the usefulness of the added constraint. 8PSK is also included as one special case of 8-APSK whose ring radius is $\sqrt{E_s}$. The SEP result of 8PSK is given by [91, eq.(10)], which is $2Q(\frac{\pi}{8}\frac{1}{\sqrt{0.5\gamma^{-1}+\sigma_{\tilde{\theta}}^2}})$. We can see that 8PSK only performs better than (1,7)-8APSK in strong oscillator phase noise. Moreover, for the SNR region of 10-20dB, (3,5)-8APSK performs better than both (2,6)-8APSK and (4,4)-8APSK, thus implying that the best value of $(l_k - l_{k-1})$ for a given N cannot be decided simply.

For $M = 16$, we use (4,4R,8)-16APSK and (4,4,4,4)-16APSK as examples, as shown in Fig. 5.1. We obtain the minimum SEP with optimized a_k for every γ via (5.3) for (4,4R,8)- and (4,4,4,4)-16APSK. As Fig. 5.3 shows, the SNR gain of both constellations with the optimized a_k compared to those with the uniformly-spaced a_k given above, respectively, is about 1dB at the SEP value of 10^{-3} of practical interest. Note again that different a_k does not affect our error floor (4.33), as Fig. 5.3 implies for (4,4R,8)-16APSK in high SNR. Besides, we note that (4,4,4,4)-16APSK

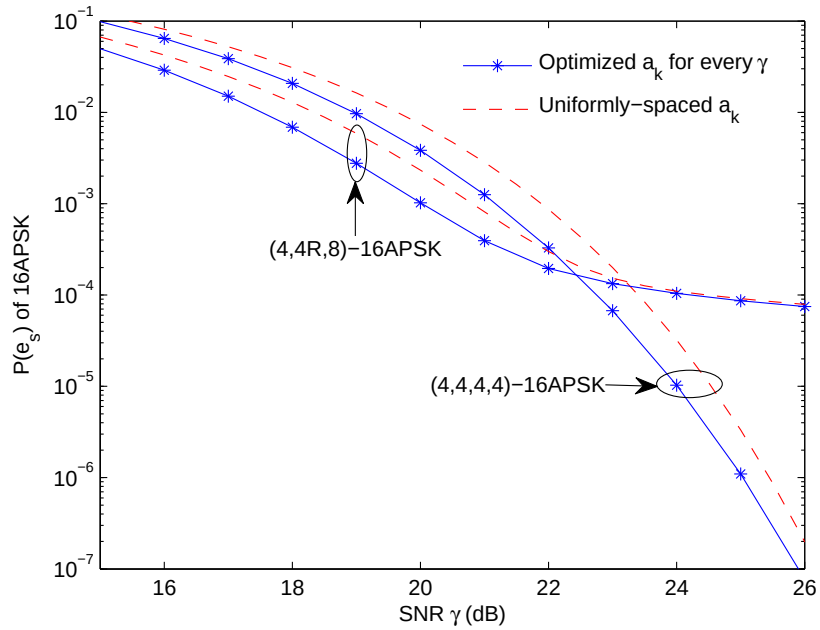

Figure 5.3: SEP comparison between optimized a_k and uniformly-spaced a_k for 16-APSK with $\sigma_{\tilde{\theta}}^2 = 0.01\text{rad}^2$.

outperforms (4,4R,8)-16APSK for high SNR. As Fig. 5.4 shows for $\sigma_{\tilde{\theta}}^2 = 0.01\text{rad}^2$, (4,4,4,4)-16APSK ($N = 4$) performs better than (5,5,6)-16APSK ($N = 3$) for $\gamma > 25$dB. This implies that more signal rings should be used for high SNR in strong phase noise, especially for larger $M \geq 16$. In addition, the performance of (3,4,4,5)-16APSK and (4,4,4,4)-16APSK has a crosspoint, implying that for the same N, the choice of l_k actually depends on γ and $\sigma_{\tilde{\theta}}^2$.

More further research work needs to be done, so that we can have more detailed discussion in the future.

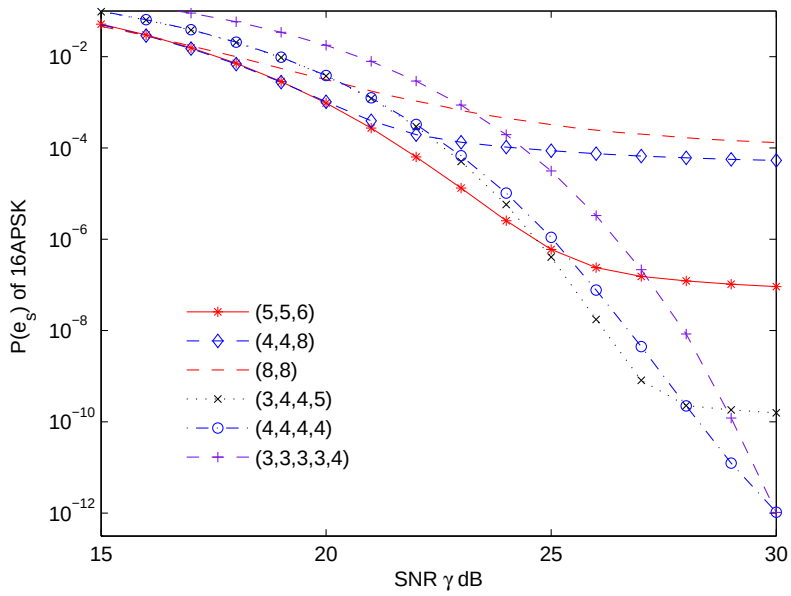

Figure 5.4: Comparison among 16-APSK constellations with optimized a_k for every γ and $\sigma_{\tilde{\theta}}^2 = 0.01\text{rad}^2$.

5.3 Concluding Remarks

This chapter provides an analytical framework for constellation design in the phase noise channel, by minimizing the error probability. We can efficiently design optimized M-APSK constellations using (5.3), since $\widehat{S}_{AS}$ is approximately optimum for large PRE or high SNR. The SEP results for the AS detector facilitate the numerical search.

The signal constellations above that are optimized by minimizing the average SEP depend on the PRE variance and the SNR. Thus, in actual applications, the receiver has to first estimate the channel state information, including the values of N_0 and $\sigma_{\tilde{\theta}}^2$, in order to decide on the best constellation to use. This decision can be fed back to the transmitter in real-time with only a small number of bits, making it possible to realize the adaptive modulation system.

Chapter 6

Error Performance Analysis over Fading

For wireless radio frequency (RF) communications, multipath fading and shadowing inevitably cause amplitude attenuation of the received signal [12]. Multipath fading is due to the constructive and destructive combination of randomly delayed, reflected, scattered, and diffracted signal components. This type of fading is relatively fast and is therefore responsible for the short-term signal variations. Depending on the nature of the radio propagation environment, there are different models describing the statistical behavior of the multipath fading envelope. In terrestrial and satellite land-mobile systems, the link quality is also affected by slow variation of the mean signal level due to the shadowing from terrain, buildings, and trees. A composite multipath/shadowed fading environment consists of multipath fading superimposed on shadowing, such as, landmobile satellite systems subject to vegetative and/or urban shadowing [12].

Free space optical (FSO) communication provides high data rate transmission with higher security and higher flexibility compared with conventional wireless communications. Due to the complexity of phase and frequency modulation, intensity modulation with direct detection is used for most current FSO communication systems [112]. The systems are exposed in environments where background radiation and atmospheric phenomena such as rain, fog, cloud and turbulence are both present and affect the system performance. Besides, the geometric spread and pointing errors caused by the vibration of the upholder of the FSO system cause additional loss and fluctuation of the optical power [6, 88].

For performance analysis, our approximate SEP/BEP results in pure AWGN, which are expressed in terms of Gaussian Q-functions, facilitate the average

error performance analysis in fading channels. This chapter thus illustrates a mathematically tractable approach to deriving the average symbol error probability (ASEP) expressions, respectively, for both wireless fading and FSO links. The approach is to use the tight upper and lower bounds on the Gaussian Q-function we derived recently, which can be easily averaged over the general mixture gamma (MG) distribution. The MG distribution is used to approximate the SNR distributions of a class of fading models, which include the Nakagami-m, Generalized-K (K_G) and Nakagami-lognormal fading as specific examples. We first focus on obtaining tight, simple algebraic-form bounds and invertible expressions for the ASEP of MPSK in a class of composite fading channels. This bounding approach avoids numerical integration of moment generating functions or numerically computing higher-order transcendental functions in the literature. Furthermore, our approach also facilitates analysing the effects of atmospheric turbulence and pointing errors on FSO communication systems. Especially for inter-satellite links, we derive the closed-form invertible approximations to the ASEP from which we can easily get the diversity gain.

Section 6.1 introduces the signal model we use here for both wireless fading and FSO channels. In Section 6.2, we introduce the bounds on the Gaussian Q-function and the MG distribution. In Section 6.3, we derive the bounds and invertible approximations on the ASEP of MPSK over fading in wireless communications. Section 6.4 analyzes the effects of turbulence and pointing errors on the ASEP of FSO links.

6.1 Signal Model

Wireless RF communication links inevitably suffer from multipath fading and shadowing. In this thesis, we only focus on the error performance analysis over different fading models for the fading gain h. We assume coherent detection with perfect phase tracking, i.e., θ in (2.1) is known and well compensated for. For FSO communication links, atmospheric turbulence and pointing errors cause intensity

fluctuations of the transmitted signals and impair link performance [6]. We will focus on analysing the effect of these impairments on the error performance of FSO systems using intensity modulation with direct detection (IM/DD). Since IM/DD is used, the unknown phase shift due to laser propagation, i.e., θ in (2.1), does not affect the error performance of the laser link. Therefore, we only need to consider the influence of h in the statistical model.

In this section, we thus introduce the simplified received signal model. That is,

$$r(k) = h(k)m(k) + n(k). \tag{6.1}$$

This is the statistical model we will use for analysis in fading. For wireless RF channels, the transmitted data symbol $m(k)$ takes on any value from the signal set $\{S_i = A_i e^{j\phi_i},\ i = 0, 1, \ldots, M-1\}$ with equal probability, and E_s is the average energy per symbol. MPSK and M-QAM are normally employed, and we have $n(k) \sim CN(0,\ N_0)$. The instantaneous SNR γ in fading is defined as $\gamma \triangleq h^2 E_s/N_0$. In this thesis, $\bar{\gamma} \triangleq \frac{\mathbb{E}[h^2]E_s}{N_0}$ denotes the average SNR per symbol, where $\mathbb{E}[.]$ denotes the expectation operator. For FSO links, the transmitted data symbol $m(k)$ equally takes on any signal point in M-ary amplitude shift keying (OOK included), and we have $n(k) \sim N(0,\ N_0/2)$..

Next, we will introduce the fading models, which are specifically used here.

6.1.1 A Class of Composite Fading Models

Radiowave propagation through wireless channels is a complicated phenomenon characterized by various effects such as multipath fading and shadowing. A precise mathematical description of this phenomenon is either unknown or too complex for tractable communication system analyses. However, considerable efforts have been devoted to the statistical modelling and characterization of these different effects. The result is a range of relatively simple and accurate statistical models for fading channels that depend on the particular propagation environment and the underlying

communication scenario [11, 12]. Among all the well-known statistical distributions to model the different fading channels, we mainly introduce the Nakagami-m, the Generalized-K (K_G) and the Nakagami-lognormal (NL) fading models, respectively.

Nakagami-m Fading

The SNR distribution, i.e., the pdf of γ, for Nakagami-m fading with the fading severity parameter $m \geq \frac{1}{2}$ is given by [68, eq. (2)]

$$p_\gamma(\gamma) = \frac{1}{\Gamma(m)} \left(\frac{m}{\bar{\gamma}}\right)^m \gamma^{m-1} e^{-m\gamma/\bar{\gamma}}. \tag{6.2}$$

K_G Fading

The SNR distribution of the K_G fading model is a Gamma-Gamma distribution with the distribution shaping parameters l and m, given by [113, eq. (2)]

$$p_\gamma(\gamma) = \frac{2(\frac{lm}{\bar{\gamma}})^{(l+m)/2} \gamma^{(l+m-2)/2}}{\Gamma(m)\Gamma(l)} K_{l-m}\Big[2(\frac{lm\gamma}{\bar{\gamma}})^{1/2}\Big], \tag{6.3}$$

where $K_\alpha(.)$ is the modified Bessel function of the second kind of order α.

NL Composite Fading

The SNR distribution in the NL fading is a gamma-lognormal (GL) distribution, given as [77, eq. (5)]

$$p_\gamma(\gamma) = \int_0^\infty \frac{\gamma^{m-1} e^{-\frac{m\gamma}{\rho t}}}{\Gamma(m)} \left(\frac{m}{\rho t}\right)^m \frac{e^{-\frac{(\ln t - \mu)^2}{2\sigma^2}}}{\sqrt{2\pi}\sigma t} dt, \tag{6.4}$$

where m is the fading parameter in Nakagami-m fading, ρ is the unfaded SNR, and μ and σ are the mean and the standard deviation of the lognormal distribution, respectively. Eq. (6.4) becomes the Rayleigh lognormal (RL) distribution when $m = 1$ [77].

6.1.2 Atmospheric Turbulence and Pointing Errors

The transmission of laser beams through atmosphere is affected by atmospheric turbulence, and geometric spread and pointing errors, which cause signal attenuation and lead to fluctuations of received optical intensity [114]. In the channel model, the channel state, i.e., the channel gain h can be formulated as [88]

$$h = h_a h_p \tag{6.5}$$

where h_a denotes the channel gain due to atmospheric turbulence, and h_p denotes the channel gain due to geometric spread and pointing errors. In the following, h_a and h_p will be introduced separately.

Atmospheric Turbulence

In [115], log-normal distribution is adopted to model h_a for weak turbulence, Gamma-Gamma distribution for moderate to strong turbulence, and the negative exponential distribution for strong turbulence. Since in [116], it has been shown that the Gamma-Gamma distribution can nicely fit the channel fading statistics of all turbulence regimes, in this thesis, we only consider h_a as a Gamma-Gamma distributed random variable, and the pdf of h_a is [88, eq.(6)]

$$p_{h_a}(h_a) = \frac{2(lm)^{(l+m)/2} h_a^{(l+m)/2-1}}{\Gamma(m)\Gamma(l)} K_{l-m}\Big[2(lmh_a)^{1/2}\Big], \tag{6.6}$$

where $K_{l-m}(.)$ is the modified Bessel function of the second kind of order $(l-m)$. Here, $\frac{1}{m}$ and $\frac{1}{l}$ are the variances of the small and large scale eddies, respectively.

Geometric Spread and Pointing Errors

To study the distribution of h_p, we need to first start from the Gaussian beam, for which, the normalized spatial distribution of the transmitted intensity at a

propagating distance z from the transmitter is given by [117] [117]

$$I_{\text{beam}}(\|\boldsymbol{\rho}\|^2;\omega_z) = \frac{2}{\pi\omega_z^2}\exp\left(-\frac{2\|\boldsymbol{\rho}\|^2}{\omega_z^2}\right), \tag{6.7}$$

where $\boldsymbol{\rho}$ is the radial vector from the beam center, and ω_z is the beam radius at which the intensity drops to e^{-2} of the axial value at the distance z. The beam radius ω_z is also referred to as the spot size, and achieves the minimum value ω_0 at $z = 0$, known as the beam waist. The relation between ω_z and ω_0 is given by [117]

$$\omega_z = \omega_0\sqrt{1+\left(\frac{z\lambda}{\pi\omega_0^2}\right)^2}, \tag{6.8}$$

where λ is the laser wave length. It should be noted that the Gaussian beam model fails if wave fronts are tilted by over approximate 0.5 rad, which corresponds to $w_0 \leq 2\lambda/\pi$ [118, P. 630].

Consider a circular optical detector $\mathbf{C}$ with radius r_c located on the received beam plane. The distance between the center of $\mathbf{C}$ and the beam center is the radial displacement caused by the pointing error, denoted as d_r. Apparently, the fraction of power that detector $\mathbf{C}$ can collect is h_p. Since it is related to d_r, r_c, ω_0 and z, we denote it as $h_p(d_r, a, \omega_0, z)$. Obviously, the value of $h_p(d_r, a, \omega_0, z)$ can be obtained by performing a double integral over the detector region, i.e.,

$$h_p(d_r, a, \omega_0, z) = \iint_{\mathbf{C}} I_{\text{beam}}(x^2+y^2;\omega_z)dxdy, \tag{6.9}$$

where d_r, r_c, ω_z, ω_0 and λ are all non-negative parameters.

Furthermore, by modelling the elevation and the horizontal displacement as two independent and identically zero mean Gaussian random variables, we can obtain the pdf of h_p as [88, eq. (11)]

$$p_{h_p}(h_p) = \frac{s^2}{A_0^{s^2}}h_p^{s^2-1},\ 0 \leq h_p \leq A_0. \tag{6.10}$$

Here, A_0 is the fraction of the collected power when no pointing error occurs, and $s = \frac{\omega_{zeq}}{2\sigma_s}$ is the ratio between the equivalent beam radius $\omega_{z_{eq}}$ at the receiver and the pointing error displacement standard jitter σ_s at the receiver [88]. We have $A_0 = [\text{erf(v)}]^2$, $\omega_{z_{eq}}^2 = \omega_z^2\sqrt{\pi}\text{erf}(v)/(2ve^{-v^2})$, and $v = \sqrt{\pi}r_c/(\sqrt{2}\omega_z)$, where erf(.) is the error function [88]. Moreover, we have

$$\mathbb{E}[h_p] = \frac{A_0}{1 + \frac{1}{s^2}} \tag{6.11}$$

where $\mathbb{E}[.]$ denotes the expectation operator.

6.2 Introduction to Bounds and the MG Distribution

Here, we introduce the approach we aim to apply throughout this chapter, which can provide a unified, simple average error probability analysis framework.

6.2.1 Bounds on the Gaussian Q-function

The asymptotically tight upper and lower bounds on the Gaussian Q-function are given, respectively, by [72, eq. (9)] [73, eq. (12)]

$$Q(x) \leq Q_{UB}(x) = \sum_{k=0}^{q} \frac{a_k}{x} \exp(-b_k x^2) \tag{6.12}$$

and

$$Q(x) \geq Q_{LB}(x) = \sum_{k=1}^{q-1} c_k x \exp(-d_k x^2), \tag{6.13}$$

where the adjustable constants a_k, b_k, c_k and d_k are given, respectively, by

$$a_k = \begin{cases} \frac{1}{\sqrt{2\pi}}, & k = 0 \\ -\frac{\epsilon_k - \epsilon_{k-1}}{\sqrt{2\pi}\epsilon_k\epsilon_{k-1}}, & k \geq 1 \end{cases} ; \; b_k = \begin{cases} \frac{1}{2}, & k = 0 \\ \frac{\epsilon_k\epsilon_{k-1}}{2}, & k \geq 1 \end{cases}$$

$$c_k = \frac{\epsilon_k - \epsilon_{k-1}}{\sqrt{2\pi}}, k \geq 1; \; d_k = \frac{\epsilon_k^2 + \epsilon_{k-1}^2 + \epsilon_k\epsilon_{k-1}}{6}, k \geq 1 \tag{6.14}$$

Here, the values of ϵ_k split the integration range $[x, \infty]$ of $Q(x)$ into q sub-ranges such that $x = \epsilon_0 x < \epsilon_1 x < \ldots < \epsilon_q x < \ldots$. For simplicity, we use uniform sub-ranges, i.e., the values of $(\epsilon_k - \epsilon_{k-1})$ for any k are equal. In [72] and [73], these bounds have been shown to be arbitrarily tight as the number of sub-ranges, q, increases.

In addition, a well-known pure exponential upper bound on $Q(x)$ is given by [74, eq.(14)]

$$Q(x) \leq \frac{1}{12}\exp\left(-\frac{x^2}{2}\right) + \frac{1}{4}\exp\left(-\frac{2x^2}{3}\right). \tag{6.15}$$

Similarly, another simple, pure exponential n-term lower bound on $Q(x)$ is given by [75, eqs.(5-6)], which is asymptotically tight as n increases. For simple illustration, we choose $n = 2$ and this 2-term pure exponential bound is [75, eq.(9)]

$$Q(x) \geq Q_{LB-KW}(x) = \frac{1}{6}\exp\left(\frac{-2\sqrt{3}x^2}{\pi}\right) + \frac{1}{6}\exp\left(\frac{-\sqrt{3}x^2}{\pi}\right). \tag{6.16}$$

This bound (6.16) has been shown to be relatively tight in [75].

6.2.2 The MG Distribution

The MG distribution is widely applied, due to its versatility and mathematical tractability [77]. The MG probability density function (pdf) of the SNR γ is composed of a weighted sum of gamma distributions, given by [77, eq. (1)]

$$p_\gamma(\gamma) = \sum_{i=1}^{N} w_i f_i(\gamma) = \sum_{i=1}^{N} \alpha_i \gamma^{\beta_i - 1}\exp(-\zeta_i\gamma). \tag{6.17}$$

Here, $f_i(\gamma) = \zeta_i^{\beta_i}\gamma^{\beta_i-1}\exp(-\zeta_i\gamma)/\Gamma(\beta_i)$ denotes the standard Gamma distribution, $w_i = \alpha_i\Gamma(\beta_i)/\zeta_i^{\beta_i}$ is a weight, N is the number of terms, and α_i, β_i and ζ_i are the parameters of the ith mixture gamma component, which depend on the different fading models we specify later. $\Gamma(.)$ denotes the gamma function given by $\Gamma(t) = \int_0^\infty x^{t-1}e^{-x}dx$. The MGF and the rth moment of the MG distribution are [77, eqs. (3)(4)], respectively,

$$M_\gamma(s) = \int_0^\infty e^{-s\gamma}p_\gamma(\gamma)d\gamma = \sum_{i=1}^{N}\frac{\alpha_i\Gamma(\beta_i)}{(s+\zeta_i)^{\beta_i}}$$

and

$$m_\gamma(r) = \mathbb{E}[\gamma^r] = \sum_{i=1}^{N}\alpha_i\Gamma(\beta_i+r)\zeta_i^{-(\beta_i+r)},$$

where $\mathbb{E}[.]$ denotes the expectation operator. The average SNR $\bar{\gamma}$ is thus obtained as

$$\bar{\gamma} = \mathbb{E}[\gamma] = \sum_{i=1}^{N}\alpha_i\Gamma(\beta_i+1)\zeta_i^{-(\beta_i+1)}. \tag{6.18}$$

The MG distribution provides a unified, simple average error probability analysis framework, since it can be used to approximate a number of the SNR distributions of the fading models, which include the Nakagami-m, K_G and Nakagami-lognormal (NL) fading as specific examples.

6.3 Bounds and Invertible Approximations to ASEP over Fading

In this section, based on the received signal model (6.1) and the MG distribution (6.56), tight, simple algebraic-form bounds and invertible expressions for the ASEP of MPSK are derived in a class of composite fading channels.

6.3.1 Upper Bounds and Invertible Approximations for MPSK for $M > 2$

We first derive the tight upper bounds on the ASEP of MPSK ($M > 2$) for the MG distribution based on the upper bound on the Gaussian Q-function. Invertible approximations are given specifically for the Nakagami-m, the K_G and the NL fading models.

We use the union upper bound given by [12, eq. (8.26)] to approximate the SEP of MPSK in the AWGN channel. Thus, the conditional SEP expression of MPSK with $M > 2$ for a given instantaneous SNR γ in fading is approximated as

$$P(e_s|\gamma) \leq 2Q\left(\sqrt{\frac{2E_s h^2}{N_0}}\sin(\pi/M)\right) = 2Q(\sqrt{g_1\gamma}), \tag{6.19}$$

where $g_1 = 2\sin^2(\pi/M)$ and $\gamma \triangleq h^2 E_s/N_0$. Here, $Q(.)$ is the Gaussian Q-function given by $Q(x) = \frac{1}{\sqrt{2\pi}}\int_x^\infty \exp\left(-\frac{u^2}{2}\right)du$. The accuracy of the union bound in (6.19) improves as M increases, which implies that all the derivations later are more accurate for larger M. The ASEP in fading, denoted as $P(\bar{\gamma})$ which depends on the distribution of γ, i.e., $p_\gamma(\gamma)$, is given by

$$P(\bar{\gamma}) \triangleq \int_0^\infty P(e_s|\gamma)p_\gamma(\gamma)d\gamma \lesssim \int_0^\infty 2Q(\sqrt{g_1\gamma})p_\gamma(\gamma)d\gamma. \tag{6.20}$$

Here, $\bar{\gamma} \triangleq \frac{\mathbb{E}[h^2]E_s}{N_0}$ denotes the average SNR per symbol.

Now, we derive the upper bound on the ASEP $P(\bar{\gamma})$ for $M > 2$, using (6.20), (6.56) and the upper bound $Q_{UB}(.)$ in (6.12). Substituting (6.56) and (6.12) into (6.20), we have the upper bound given as

$$P(\bar{\gamma}) \leq P_{UB}(\bar{\gamma}) = \sum_{k=0}^{q}\sum_{i=1}^{N}\frac{2a_k\alpha_i}{\sqrt{g_1}}\int_0^\infty \gamma^{\beta_i-\frac{3}{2}}\exp(-(b_k g_1+\zeta_i)\gamma)d\gamma.$$

Then substituting $t = \beta_i - \frac{1}{2}$ and $x = (b_k g_1 + \zeta_i)\gamma$ into the gamma function $\Gamma(t)$

defined as $\Gamma(t) = \int_0^\infty x^{t-1}e^{-x}dx$, we have

$$\int_0^\infty \gamma^{\beta_i - \frac{3}{2}} \exp(-(b_k g_1 + \zeta_i)\gamma) d\gamma = \Gamma(\beta_i - \frac{1}{2})(b_k g_1 + \zeta_i)^{-(\beta_i - \frac{1}{2})}.$$

Therefore, combining the two equations above, the upper bound on $P(\bar{\gamma})$ of MPSK ($M > 2$) for the MG distribution is obtained as

$$P(\bar{\gamma}) \leq P_{UB}(\bar{\gamma}) = \sum_{k=0}^{q} \sum_{i=1}^{N} \frac{2a_k \alpha_i \Gamma(\beta_i - \frac{1}{2})}{\sqrt{g_1}} (b_k g_1 + \zeta_i)^{-(\beta_i - \frac{1}{2})}. \tag{6.21}$$

Here, α_i and ζ_i are functions of $\bar{\gamma}$, but β_i is fixed for a specific fading model [77], which we show later. Thus, in terms of computational complexity, $\Gamma(\beta_i - \frac{1}{2})$ is pre-computable and only needs to be computed once for all values of $\bar{\gamma}$. Since a_k, b_k and g_1 are constants, we only need to compute α_i and ζ_i for every $\bar{\gamma}$. Therefore, our result (6.21) is a purely algebraic function in terms of $\bar{\gamma}$. This upper bound is an explicit expression, which provides insights into how the parameters affect the performance.

It is worth noting that by comparing with the exact ASEP, the tight bound (6.21) turns out to be a very accurate approximation which can be inverted for high SNR. The invertible expression is given in the form:

$$P(\bar{\gamma}) \approx C\bar{\gamma}^{-D}, \tag{6.22}$$

where C and D are constants independent of $\bar{\gamma}$. Thus, to achieve a given value of $P(\bar{\gamma})$, one can easily specify the required value of $\bar{\gamma}$ as

$$\bar{\gamma} \approx \left(\frac{C}{P(\bar{\gamma})}\right)^{\frac{1}{D}}. \tag{6.23}$$

The diversity order of the system, denoted as G_d, is defined as [11]

$$G_d = \frac{-\log P(\bar{\gamma})}{\log \bar{\gamma}}|_{\bar{\gamma}\to\infty}.$$

We can see from (6.22) that the diversity order G_d is D here.

The exact ASEP $P(\bar{\gamma})$ of MPSK for any M over the MG distribution is given by [77, eq. (25)] or [12, eq. (9.15)]

$$P(\bar{\gamma}) = \sum_{i=1}^{N} \frac{\alpha_i \Gamma(\beta_i)}{\pi \zeta_i^{\beta_i}} \int_0^{\frac{(M-1)\pi}{M}} \left(\frac{\sin^2\theta}{\sin^2\theta + \frac{\sin^2(\frac{\pi}{M})}{\zeta_i}} \right)^{\beta_i} d\theta \tag{6.24}$$

which can only be computed by numerical integration for every $\bar{\gamma}$. Besides, (6.24) cannot explicitly show how $P(\bar{\gamma})$ depends on $\bar{\gamma}$, and cannot be inverted to get the required $\bar{\gamma}$ given $P(\bar{\gamma})$.

The invertible ASEP expression cannot be directly obtained for the general MG distribution, because $\bar{\gamma}$ is contained in the parameters α_i and ζ_i, which vary with the different fading models used. Therefore, in the following subsections, the tight, algebraic-form bounds and the invertible ASEP expressions are derived specifically for the Nakagami-m, the K_G and the NL composite fading channels, whose SNR distributions are well approximated by the MG distribution. For all these three fading models, no comparable algebraic-form bounds and approximations are available for MPSK with $M > 2$ in the literature.

Nakagami-m Fading

The SNR distribution of Nakagami-m fading, given by (6.2), with the fading severity parameter $m \geq \frac{1}{2}$ is one special case of the MG distribution. This SNR distribution can be rewritten in the MG form (6.56) with parameters [77, Sect.III.G]:

$$N = 1,\ \alpha_1 = \frac{m^m}{\Gamma(m)\bar{\gamma}^m},\ \beta_1 = m,\ \zeta_1 = \frac{m}{\bar{\gamma}}. \tag{6.25}$$

Substituting (6.25) into (6.21), we obtain the upper bound on $P(\bar{\gamma})$ of MPSK ($M > 2$) for Nakagami-m fading:

$$P(\bar{\gamma}) \leq P_{UB}(\bar{\gamma}) = \sum_{k=0}^{q} \frac{2a_k m^m \Gamma(m-\frac{1}{2})}{\sqrt{g_1}\bar{\gamma}^m \Gamma(m)} (b_k g_1 + \frac{m}{\bar{\gamma}})^{-(m-\frac{1}{2})}. \tag{6.26}$$

We can see that our bound (6.26) is in purely algebraic form in terms of $\bar{\gamma}$. As noted, $\Gamma(m)$ and $\Gamma(m-\frac{1}{2})$ are pre-computable and fixed for all $\bar{\gamma}$.

Since our upper bound (6.26) can be extremely tight by adjusting the parameters q and $(\epsilon_k - \epsilon_{k-1})$, (6.26) is further used as a good approximation to $P(\bar{\gamma})$.

For high average SNR $\bar{\gamma}$ such that $m/\bar{\gamma}$ in the bracket can be ignored compared with $b_k g_1$ in (6.26), the upper bound is simplified into the product of a constant and $\bar{\gamma}^{-m}$. Therefore, this simplified bound gives the inverse ASEP expression (6.22) for Nakagami-m fading, where $D = m$ and C is given by

$$C = \sum_{k=0}^{q} \frac{2a_k m^m \Gamma(m-\frac{1}{2})}{\sqrt{g_1}\Gamma(m)} (b_k g_1)^{-(m-\frac{1}{2})}.$$

K_G Fading

The SNR distribution of the K_G fading model is a Gamma-Gamma distribution with the distribution shaping parameters l and m, given by (6.3). It also has the integral-form expression given by [77, eq. (8)]

$$p_\gamma(\gamma) = \frac{(\frac{lm}{\bar{\gamma}})^m \gamma^{m-1}}{\Gamma(m)\Gamma(l)} \int_0^\infty e^{-t} g(t) dt.$$

Here, we have $g(t) = t^{l-m-1} e^{-\frac{lm\gamma}{t\bar{\gamma}}}$. The integral, $I = \int_0^\infty e^{-t} g(t) dt$, can be approximated as a Gaussian-Laguerre quadrature sum, i.e., $I \approx \sum_{i=1}^{N} \omega_i g(t_i)$, where t_i and ω_i are the abscissas and weight factors for the Gaussian-Laguerre integration given in [119]. This integral-form expression can be rewritten in the MG form (6.56) with the corresponding parameters [77, eq. (9)]:

$$\alpha_i = \psi(\theta_i, \beta_i, \zeta_i),\ \beta_i = m,\ \zeta_i = \frac{lm}{t_i \bar{\gamma}},\ \theta_i = \frac{(\frac{lm}{\bar{\gamma}})^m \omega_i t_i^{l-m-1}}{\Gamma(m)\Gamma(l)} \tag{6.27}$$

where $\psi(\theta_i, \beta_i, \zeta_i) = \frac{\theta_i}{\sum_{j=1}^{N} \theta_j \Gamma(\beta_j) \zeta_j^{-\beta_j}}$, which is also used for subsequent cases.

Substituting these parameters into (6.21) leads to the following upper bound

on the ASEP for the K_G fading model:

$$P(\bar{\gamma}) \leq P_{UB}(\bar{\gamma}) = \sum_{k=0}^{q}\sum_{i=1}^{N} \frac{2a_k\Gamma(m-\frac{1}{2})\omega_i t_i^{l-1}}{\sqrt{g_1}\Gamma(m)\sum_{j=1}^{N}\omega_j t_j^{l-1}} (\frac{\bar{\gamma}t_i}{lm})^{-m}\big(b_k g_1 + \frac{lm}{t_i\bar{\gamma}}\big)^{-(m-\frac{1}{2})}. \tag{6.28}$$

For high SNR, the term $\frac{lm}{t_i\bar{\gamma}}$ in the later bracket in (6.28) can be dropped to obtain the invertible ASEP expression. It follows that our simplified bound (6.28) gives the invertible result (6.22) with $D = m$ and C given by

$$C = \frac{2(lm)^m \sum_{i=1}^{N}\omega_i t_i^{l-m-1}}{\sum_{j=1}^{N}\omega_j t_j^{l-1}} \left[\sum_{k=0}^{q} \frac{a_k\Gamma(m-\frac{1}{2})}{\sqrt{g_1}\Gamma(m)}(b_k g_1)^{\frac{1}{2}-m}\right].$$

NL Composite Fading

The SNR distribution in the NL fading is a gamma-lognormal (GL) distribution, given as (6.4).Eq. (6.4) can be expressed as the MG pdf (6.56) with the parameters [77, eq. (7)]:

$$\begin{aligned} &\alpha_i = \psi(\theta_i, \beta_i, \zeta_i),\ \beta_i = m \\ &\zeta_i = \frac{m}{\rho}e^{-(\sqrt{2}\sigma t_i+\mu)},\ \theta_i = \left(\frac{m}{\rho}\right)^m \frac{w_i e^{-m(\sqrt{2}\sigma t_i+\mu)}}{\sqrt{\pi}\Gamma(m)} \end{aligned} \tag{6.29}$$

where t_i and w_i are the abscissas and weight factors for the Gaussian-Hermite integration [119]. Term ρ is the unfaded SNR, and μ and σ are the mean and the standard deviation of the lognormal distribution, respectively.

Therefore, we can have the tight upper bound on the ASEP with respect to ρ in the NL composite fading given by

$$\begin{aligned} P(\bar{\gamma}) \leq P_{UB}(\bar{\gamma}) = &\sum_{k=0}^{q}\sum_{i=1}^{N} \frac{2a_k\Gamma(m-\frac{1}{2})w_i e^{-m(\sqrt{2}\sigma t_i+\mu)}}{\sqrt{g_1}\Gamma(m)\sum_{j=1}^{N} w_j} \\ &\left(\frac{m}{\rho}\right)^m \big(b_k g_1 + \frac{m}{\rho}e^{-(\sqrt{2}\sigma t_i+\mu)}\big)^{-(m-\frac{1}{2})}. \end{aligned} \tag{6.30}$$

Besides, substituting the parameters (6.29) into (6.18) yields

$$\rho = C_1 \bar{\gamma}, \tag{6.31}$$

where $C_1 = \frac{\sum_{j=1}^{N} w_j}{\sum_{i=1}^{N} w_i e^{(\sqrt{2}\sigma t_i + \mu)}}$, is a constant. Thus, we have a linear relation between ρ and $\bar{\gamma}$.

For high average SNR $\bar{\gamma}$ or large value of ρ, the term $\frac{m}{\rho} e^{-(\sqrt{2}\sigma t_i + \mu)}$ in the later bracket in (6.30) can be removed to obtain the invertible ASEP expression. Thus, we have the explicit result (6.22) with $D = m$ and

$$C = \frac{\sum_{i=1}^{N} w_i e^{-m(\sqrt{2}\sigma t_i + \mu)}}{\sum_{j=1}^{N} w_j} \left(\frac{m}{C_1}\right)^m \left[\sum_{k=0}^{q} \frac{2a_k \Gamma(m - \frac{1}{2})}{\sqrt{g_1}\Gamma(m)} (b_k g_1)^{-(m-\frac{1}{2})}\right].$$

6.3.2 Tight Bounds and Invertible ASEP for BPSK

For BPSK ($M = 2$), the transmitted phase is $\phi \in \{0, \pi\}$. Our bounding approach can be easily used on coherent BPSK, since the exact SEP/BEP result of BPSK in the pure AWGN channel is one Gaussian Q-function: $P(e_s) = Q(\sqrt{\frac{2E_s}{N_0}})$ [12]. Thus, the exact ASEP/ABEP $P(\bar{\gamma})$ in fading is given by

$$P(\bar{\gamma}) = \int_0^\infty Q(\sqrt{g_2 \gamma}) p_\gamma(\gamma) d\gamma \tag{6.32}$$

where $g_2 = g_1|_{M=2} = 2\sin^2(\pi/M)|_{M=2} = 2$.

By upper bounding $Q(.)$ in (6.32) with (6.12) and using the same procedure as above, we can obtain the same upper bounds on $P(\bar{\gamma})$ of BPSK as (6.21), (6.26), (6.28) and (6.30), except that all these results have to be divided by a factor of 2. Thus, arbitrarily tight upper bounds $P_{UB}(\bar{\gamma})$ on $P(\bar{\gamma})$ in (6.32) are first obtained, by adjusting the parameters q and $(\epsilon_k - \epsilon_{k-1})$.

Next, we want to derive the arbitrarily tight lower bounds on $P(\bar{\gamma})$ in (6.32), using the lower bound on the Gaussian Q-function given by (6.13). Substituting (6.56) and (6.13) into (6.32), the lower bound on $P(\bar{\gamma})$ for the MG distribution is

derived as

$$P(\bar{\gamma}) \geq P_{LB}(\bar{\gamma}) = \sum_{k=1}^{q-1} \sum_{i=1}^{N} c_k \sqrt{g_2} \alpha_i \Gamma(\beta_i + \frac{1}{2})(d_k g_2 + \zeta_i)^{-(\beta_i + \frac{1}{2})}. \tag{6.33}$$

As noted, in terms of computational complexity, $\Gamma(\beta_i + \frac{1}{2})$ is pre-computable and only needs to be computed once for all values of $\bar{\gamma}$. Since $c_k,\ d_k$ and g_2 are constants, we only need to compute α_i and ζ_i for every $\bar{\gamma}$. Therefore, our result (6.33) is purely algebraic-form in terms of $\bar{\gamma}$.

Moreover, the average of the above upper and lower bounds gives us an accurate approximation to the exact ASEP of BPSK, that is

$$P(\bar{\gamma}) \approx \frac{1}{2}(P_{UB}(\bar{\gamma}) + P_{LB}(\bar{\gamma})), \tag{6.34}$$

which also leads to invertible expressions given in the form of (6.22) for high SNR, specifically for Nakagami-m, K_G and NL composite fading shown below.

For the three fading models, our explicit upper and lower bounds are new and there is no comparable result in the literature. Numerical results show later that the bounds and approximations are arbitrarily tight and accurate compared to the existing results.

Nakagami-m Fading

Substituting (6.25) into (6.33), we obtain the lower bound on $P(\bar{\gamma})$ of BPSK for Nakagami-m fading:

$$P(\bar{\gamma}) \geq P_{LB}(\bar{\gamma}) = \sum_{k=1}^{q-1} \frac{c_k \sqrt{g_2} m^m \Gamma(m + \frac{1}{2})}{\bar{\gamma}^m \Gamma(m)} (d_k g_2 + \frac{m}{\bar{\gamma}})^{-(m+\frac{1}{2})}. \tag{6.35}$$

We can see that our upper bound (6.26) with the corresponding change, i.e., without the factor of 2 and with g_1 replaced by g_2 inside, and our lower bound (6.35) are purely algebraic functions in terms of $\bar{\gamma}$.

Subsequently, (6.34) in conjunction with (6.35) and the changed (6.26) gives a

very good approximation for BPSK.

For large $\bar{\gamma}$ such that $m/\bar{\gamma}$ in the brackets can be ignored compared with $b_k g_2$ in (6.26) or $d_k g_2$ in (6.35), both upper and lower bounds are simplified into the product of a constant and $\bar{\gamma}^{-m}$. Therefore, (6.34) in conjunction with the simplified bounds gives the inverse ASEP expression (6.22) for Nakagami-m fading, where $D = m$ and C is given by

$$C = \sum_{k=0}^{q} \frac{a_k m^m \Gamma(m-\frac{1}{2})}{2\sqrt{g_2}\Gamma(m)} (b_k g_2)^{-(m-\frac{1}{2})} + \sum_{k=1}^{q-1} \frac{c_k \sqrt{g_2} m^m \Gamma(m+\frac{1}{2})}{2\Gamma(m)} (d_k g_2)^{-(m+\frac{1}{2})}.$$

For this Nakagami-m fading case, an approximation to the ASEP of BPSK is given by [65, eq. (10)]. This latter result is comparable in accuracy to our result (6.34) as shown numerically later.

K_G Fading

Substituting the parameters (6.57) into (6.33) leads to the lower bound on the ASEP for the K_G fading model:

$$P(\bar{\gamma}) \geq P_{LB}(\bar{\gamma}) = \sum_{k=1}^{q-1} \sum_{i=1}^{N} \frac{c_k \sqrt{g_2} \Gamma(m+\frac{1}{2}) \omega_i t_i^{l-1}}{\Gamma(m) \sum_{j=1}^{N} \omega_j t_j^{l-1}} (\frac{\bar{\gamma} t_i}{lm})^{-m} \big(d_k g_2 + \frac{lm}{t_i \bar{\gamma}}\big)^{-(m+\frac{1}{2})}. \quad (6.36)$$

For high SNR, the term $\frac{lm}{t_i \bar{\gamma}}$ in the later brackets in the lower bound (6.36) and the correspondingly changed upper bound (6.28) can be dropped to obtain the invertible ASEP expression. It follows that our approximation (6.34) in conjunction with the simplified (6.28) and (6.36) gives the invertible result (6.22) with $D = m$ and C given by

$$C = \frac{(lm)^m \cdot \sum_{i=1}^{N} \omega_i t_i^{l-m-1}}{2\sum_{j=1}^{N} \omega_j t_j^{l-1}} \left[\sum_{k=0}^{q} \frac{a_k \Gamma(m-\frac{1}{2})}{\sqrt{g_2}\Gamma(m)} (b_k g_2)^{-(m-\frac{1}{2})} + \sum_{k=1}^{q-1} \frac{c_k \sqrt{g_2} \Gamma(m+\frac{1}{2})}{\Gamma(m)} (d_k g_2)^{-(m+\frac{1}{2})} \right].$$

NL Composite Fading

Similarly, we can have the tight lower bound on the ASEP with respect to ρ in the NL composite fading given by

$$P(\bar{\gamma}) \geq P_{LB}(\bar{\gamma}) = \sum_{k=1}^{q-1}\sum_{i=1}^{N} \frac{c_k\sqrt{g_2}\Gamma(m+\frac{1}{2})w_i e^{-m(\sqrt{2}\sigma t_i+\mu)}}{\Gamma(m)\sum_{j=1}^{N} w_j} \left(\frac{m}{\rho}\right)^m \left(d_k g_2 + \frac{m}{\rho}e^{-(\sqrt{2}\sigma t_i+\mu)}\right)^{-(m+\frac{1}{2})}. \tag{6.37}$$

Eq (6.31) shows the linear relation between ρ and $\bar{\gamma}$.

For high average SNR $\bar{\gamma}$ or large value of ρ, the term $\frac{m}{\rho}e^{-(\sqrt{2}\sigma t_i+\mu)}$ in the later brackets in (6.30) and (6.37) can be removed to obtain the invertible ASEP expression. That is, by taking the average of the simplified (6.30) and (6.37), we thus have the explicit result (6.22) with $D = m$ and

$$C = \frac{\sum_{i=1}^{N} w_i e^{-m(\sqrt{2}\sigma t_i+\mu)}}{2\sum_{j=1}^{N} w_j} \left[\sum_{k=0}^{q} \frac{a_k\Gamma(m-\frac{1}{2})}{\sqrt{g_2}\Gamma(m)}(b_k g_2)^{-(m-\frac{1}{2})} + \sum_{k=1}^{q-1} \frac{c_k\sqrt{g_2}\Gamma(m+\frac{1}{2})}{\Gamma(m)}(d_k g_2)^{-(m+\frac{1}{2})}\right]\left(\frac{m}{C_1}\right)^m.$$

Furthermore, as mentioned in [77], there are other fading models whose SNR distributions can be accurately approximated by the MG distribution, such as $\eta-\mu$, $\kappa-\mu$, Nakagami-q and Nakagami-n fading. We can directly obtain arbitrarily tight bounds and accurate approximations for these models by using (6.21), (6.33) and (6.34). However, it should be noted that invertible expressions cannot be derived since β_i in these models is not a constant, but varies with i [77].

6.3.3 Numerical Results and Comparisons

To check the accuracy of our bounds and approximations, the exact ASEP expressions for any MPSK are obtained by substituting (6.25), (6.57) and (6.29)

into (6.24), respectively. That is, for Nakagami-m fading, we have

$$P(\bar{\gamma}) = \frac{1}{\pi}\int_0^{\frac{(M-1)\pi}{M}} \left(\frac{\sin^2\theta}{\sin^2\theta + \frac{\bar{\gamma}\sin^2(\frac{\pi}{M})}{m}}\right)^m d\theta. \tag{6.38}$$

For K_G fading, the exact ASEP of MPSK is

$$P(\bar{\gamma}) = \sum_{i=1}^{N} \frac{\omega_i t_i^{l-1}}{\pi\sum_{j=1}^{N}\omega_j t_j^{l-1}} \int_0^{\frac{(M-1)\pi}{M}} \left(\frac{\sin^2\theta}{\sin^2\theta + \frac{\sin^2(\frac{\pi}{M})t_i\bar{\gamma}}{lm}}\right)^m d\theta. \tag{6.39}$$

For NL composite fading, the exact ASEP result is given by

$$P(\bar{\gamma}) = \sum_{i=1}^{N} \frac{w_i}{\pi\sum_{j=1}^{N} w_j} \int_0^{\frac{(M-1)\pi}{M}} \left(\frac{\sin^2\theta}{\sin^2\theta + \frac{\sin^2(\frac{\pi}{M})\rho}{me^{-(\sqrt{2}\sigma t_i+\mu)}}}\right)^m d\theta. \tag{6.40}$$

These can also be obtained using the MGF based approach given in [12, 67].

We compare our invertible result (6.22) with [120, eq. (24)], which is also an invertible approximation to the ASEP of MPSK:

$$P(\bar{\gamma}) \approx \left[\frac{b}{\pi}\int_0^{\frac{(M-1)\pi}{M}} \left(\frac{\sin^2\theta}{\sin^2(\frac{\pi}{M})}\right)^d d\theta\right]\bar{\gamma}^{-d}. \tag{6.41}$$

It can easily be shown that we have $b = \sum_{i=1}^{N}\alpha_i\Gamma(\beta_i)$ and $d = \beta_i$ for the general MG distribution, according to the analysis in [121]. By substituting (6.25), (6.57) and (6.29) into (6.41), we thus have the invertible results for the three models, respectively. For Nakagami-m fading only, another comparable invertible ASEP result for BPSK is given by [65, eq. (11)].

To compare with the exact ASEP results (6.38), (6.39) and (6.40), and the invertible one (6.41), $M = 2, 4, 8$ and 16 are considered for Nakagami-m fading. Only the cases of $M = 2$ and 4 are shown as examples for the K_G and the NL fading for simplicity. For the Nakagami-m fading model, we have $m = 2.7$ here [77]. For the K_G and the NL composite fading, the parameters are chosen as $(m, l, N) = (2, 5, 6)$ and $(m, \sigma, \mu, N) = (2, 1, 0.25, 9)$, respectively [77]. We set $q = 8$ and $(\epsilon_k - \epsilon_{k-1}) = 0.5$

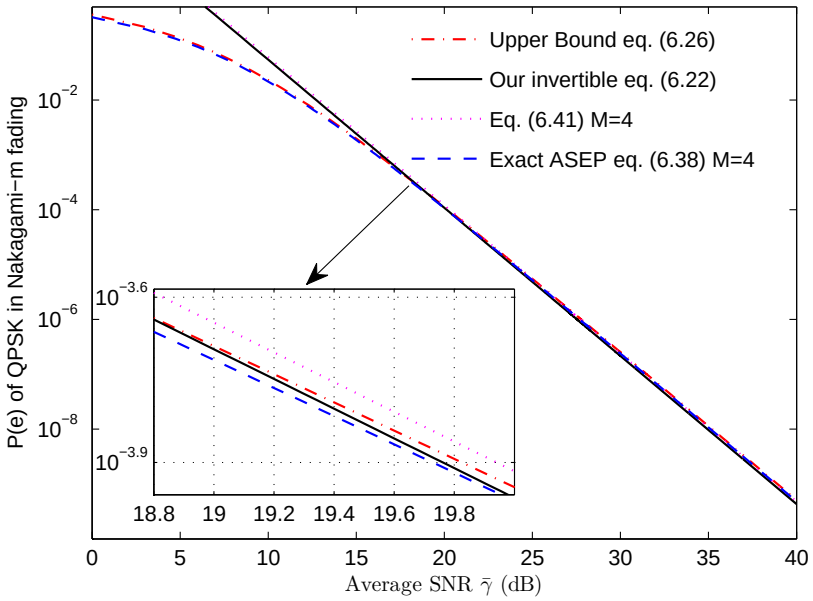

(a)

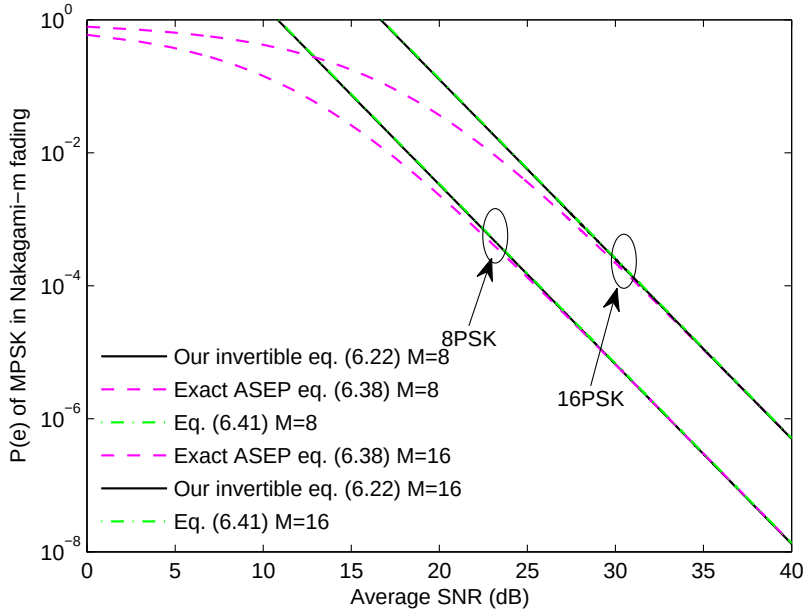

(b)

Figure 6.1: ASEP comparison of MPSK for Nakagami-m Fading: (a) $M = 4$, (b) $M = 8$ and 16.

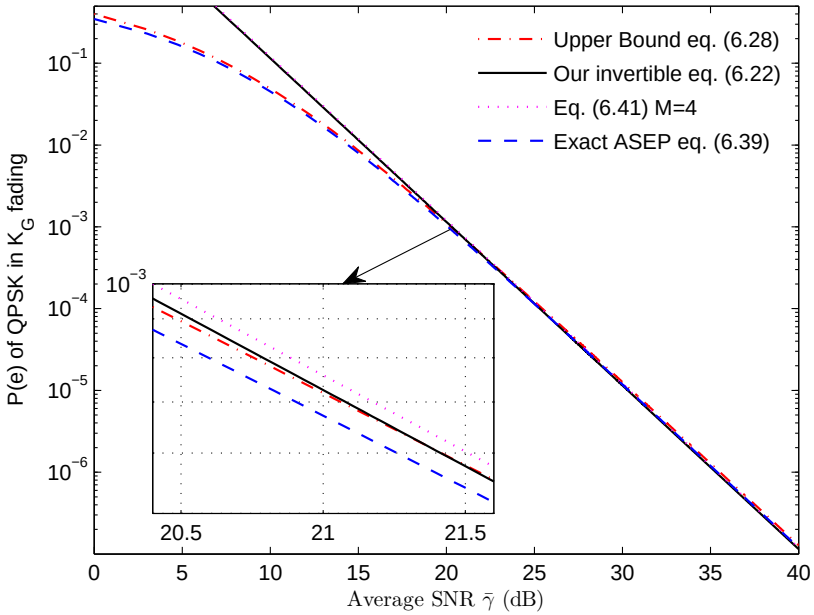

(a)

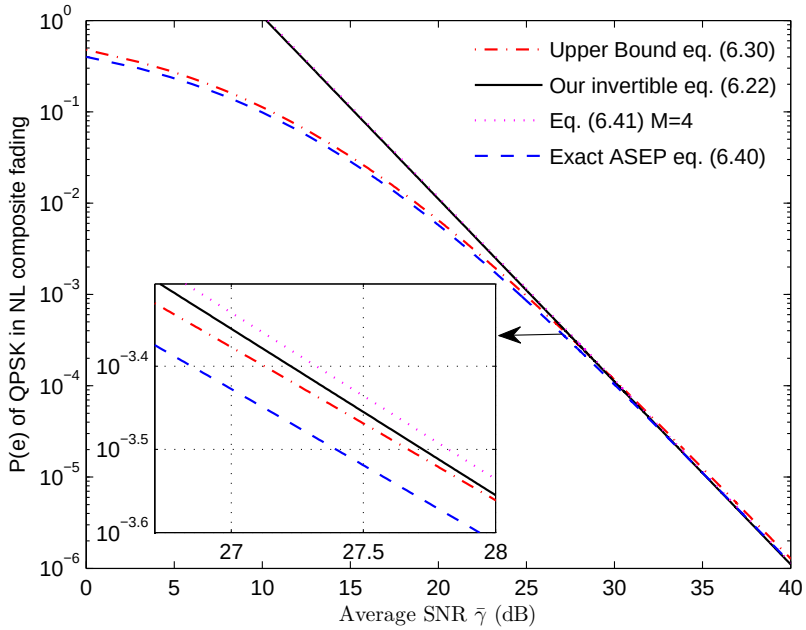

(b)

Figure 6.2: ASEP comparison of QPSK: (a) K_G fading, (b) NL composite fading.

here, which are sufficient for the accuracy of our results.

For $M > 2$, as Figs. 6.1-6.2 show, our upper bounds (6.26), (6.28) and (6.30) are tight throughout the whole SNR region of practical interest. Our new invertible approximations (6.22) are accurate and comparable with (6.41) in the SNR region of interest. They can become more tight and accurate by adjusting the parameters q and ϵ_k in (6.14).

For BPSK, the numerical comparison among the above results is shown in Fig. 6.3. It can be seen that the corresponding upper bound (6.21) and lower bound (6.33), and the approximation (6.34) are accurate for all SNR values of interest in all the three cases. They can be arbitrarily tight and accurate by adjusting the parameters q and $(\epsilon_k - \epsilon_{k-1})$ in (6.14). One way to improve the accuracy is by increasing the number of partition sub-ranges, q. The other way here is to fix q and shift the partition points ϵ_k, making the values of $(\epsilon_k - \epsilon_{k-1})$ smaller to tighten the bounds (6.12) and (6.13). Besides, as Fig. 6.3(a) shows, our approximation and [65, eq. (10)] provide very similar asymptotic behavior to the exact ASEP. Furthermore, our invertible ASEP expressions (6.22) are very accurate in the SNR region corresponding to the ASEP values of 10^{-3} and lower, which are of practical interest. Thus, (6.22) is comparable in accuracy with the result (6.41) in all three cases. Our invertible results are yet adjustable and can be more accurate. This shows the flexibility of our unified approach combined with the Gaussian Q-function bounds (6.12) and (6.13) in different fading channels.

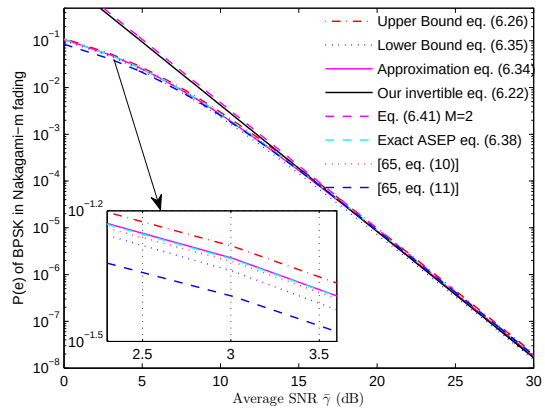

(a)

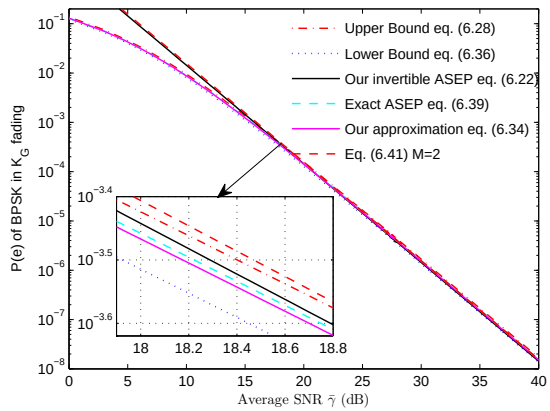

(b)

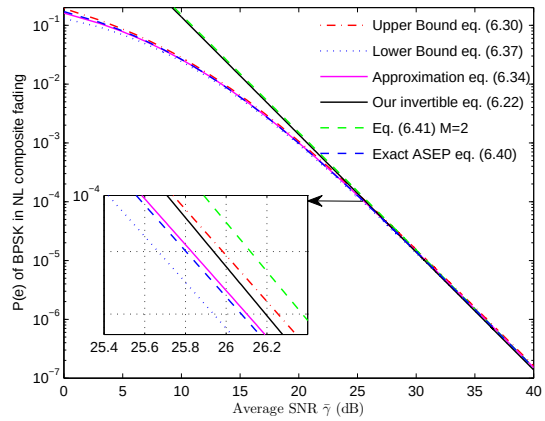

(c)

Figure 6.3: ASEP comparison of BPSK: (a) for Nakagami-m fading $m = 2.7$, (b) for K_G fading $(m, l, N) = (2, 5, 6)$, (c) for NL composite fading $(m, \sigma, \mu, N) = (2, 1, 0.25, 9)$.

6.4 Influence of Turbulence and Pointing Errors on FSO Systems

In this section, we extend the use of our bounds with the MG approximation to analyze the influence of turbulence and pointing errors on FSO systems with the received signal model given by (6.1). We only consider on-off keying (OOK) here, and the transmitted data symbol $m(k)$ takes on any value from set $\{0, \mathrm{A}\}$ with equal probability. The AWGN $n(k)$ has mean zero and variance $N_0/2$, where N_0 is the one-sided power spectrum density. We have $A = 2\sqrt{T_s}RP_t$, where P_t is the transmit power, and R is the photodetector responsivity [122]. We have $T_s = 1/R_{\text{data}}$ where R_{data} is the system data rate, and $R = \frac{\eta e}{h\nu} = \frac{\lambda \eta e}{hc}$ where $\lambda = 1.55\mu$m is the optical carrier wavelength, $\eta = 1$ is the quantum efficiency, h is the Planks constant, e is the elementary charge and c is the light speed in vacuum.

6.4.1 ASEP for Inter-Satellite Laser Communications

Long distance inter-satellite laser communication links are highly vulnerable due to the degrading effect of pointing errors [86–90]. The pointing errors are due to platform vibrations, which cause vibrations of the transmitter telescope and, therefore, misalignment between the transmitter and the receiver [86, 87]. Various statistical models have been proposed over the years to describe the pointing errors [86, 88]. In these works, the effects of misalignment on the error performance have been investigated. However, the existing results for the average bit error probability (ABEP) involve numerical multiple integration [86], or numerically computing higher-order transcendental functions [87], which do not facilitate further analysis. No simple, closed-form expressions for the ABEP are given so far, and the diversity gain cannot be easily derived.

Here, we analyze the effect of pointing errors on the error performance of an inter-satellite laser link. Our approach is to obtain tight, algebraic-form upper and lower bounds on the ABEP, by using the tight bounds on the Gaussian Q-function

derived in [72–75]. For large transmit power, all the bounds can simplify to invertible expressions, which turn out to be accurate approximations corresponding to the ABEP values of 10^{-3} and lower, which are of practical interest. More importantly, the diversity gain is straightforwardly obtained, which is related to the ratio of the equivalent beam radius to the pointing error displacement standard jitter at the receiver. We will show the explicit insights into how the channel parameters affect the ABEP via simulations.

Bounds on the ABEP

For OOK, the conditional BEP for a given value of h_p is given as [122, eq. (17)]

$$P(e|h_p) = Q(h_p\sqrt{\gamma}) = Q\left(h_p\sqrt{\frac{2T_s(RP_t)^2}{N_0}}\right). \tag{6.42}$$

Here, we have $\gamma = 2T_s(RP_t)^2/N_0$. Thus, the ABEP $P(e)$ can be obtained by

$$P(e) = \int_0^\infty P(e|h_p)p_{h_p}(h_p)dh_p, \tag{6.43}$$

with $p_{h_p}(h_p)$ given in (6.10). This exact result involves double integral and does not provide explicit insights on how the parameters affect the error performance.

Using the upper bound (6.12) on (6.42) in conjunction with (6.10) and (6.43), we can derive the upper bound on the ABEP given as

$$P(e) \leq P_{UB}(e) = \sum_{k=0}^{q} \frac{a_k s^2}{2{A_0}^{s^2}\sqrt{\gamma}}\left(b_k\gamma\right)^{\frac{1-s^2}{2}} \underline{\Gamma}\left(\frac{s^2-1}{2}, b_k\gamma {A_0}^2\right), \tag{6.44}$$

since we have $\underline{\Gamma}(\alpha, x) = \int_0^x e^{-t}t^{\alpha-1}dt$, $[\mathfrak{Re}\ \alpha > 0]$, where $\underline{\Gamma}(\cdot,\cdot)$ denotes the lower incomplete gamma function. Moreover, the lower bound (6.13) in conjunction with (6.10)-(6.43) leads to the lower bound on the exact ABEP derived as

$$P(e) \geq P_{LB}(e) = \sum_{k=1}^{q-1} \frac{c_k s^2\sqrt{\gamma}}{2{A_0}^{s^2}}(d_k\gamma)^{-\frac{s^2+1}{2}} \underline{\Gamma}\left(\frac{s^2+1}{2}, d_k\gamma {A_0}^2\right). \tag{6.45}$$

Both bounds (6.44) and (6.45) are explicit, closed-form expressions, which provide explicit insights into how the performance depends on the system parameters. We will show later that these bounds are extremely tight and mathematically tractable for any system parameters.

Moreover, the pure exponential upper bound on $Q(x)$ given by (6.15) in conjunction with (6.10)-(6.43) gives a simple upper bound on $P(e)$, that is,

$$P(e) \leq P_{UB-C}(e) = \frac{s^2}{24A_0^{s^2}}\left(\frac{\gamma}{2}\right)^{-\frac{s^2}{2}} \underline{\Gamma}\left(\frac{s^2}{2}, \frac{\gamma {A_0}^2}{2}\right) + \frac{s^2}{8A_0^{s^2}}\left(\frac{2\gamma}{3}\right)^{-\frac{s^2}{2}} \underline{\Gamma}\left(\frac{s^2}{2}, \frac{2\gamma {A_0}^2}{3}\right). \tag{6.46}$$

Similarly, the pure exponential lower bound (6.16) can lead to a tight lower bound on $P(e)$ as

$$P(e) \geq P_{LB-KW}(e) = \frac{s^2}{12A_0^{s^2}}\left(\frac{\sqrt{3}\gamma}{\pi}\right)^{-\frac{s^2}{2}} \left[(\sqrt{2})^{-s^2}\underline{\Gamma}\left(\frac{s^2}{2}, \frac{2\sqrt{3}\gamma {A_0}^2}{\pi}\right) + \underline{\Gamma}\left(\frac{s^2}{2}, \frac{\sqrt{3}\gamma {A_0}^2}{\pi}\right)\right]. \tag{6.47}$$

Since (6.46) and (6.47) have fewer terms, as we will show, they are not as tight as the bounds given in (6.44) and (6.45). We can see that all of these bounds have similar forms.

Invertible Approximations and Diversity Gain

Here, we will show that for a large value of P_t, i.e., large γ, all of these bounds can reduce to invertible expressions, given in the form:

$$P(e) \approx C\gamma^{-\frac{s^2}{2}} = DP_t^{-s^2}. \tag{6.48}$$

Here, C is a constant, and we have $D = C\left(\frac{2T_sR^2}{N_0}\right)^{-\frac{s^2}{2}}$. For a given value of $P(e)$, one can easily obtain the required value of P_t,

$$P_t \approx \left(\frac{D}{P(e)}\right)^{s^{-2}}. \tag{6.49}$$

It is shown later via simulations that (6.48) turns out to be an accurate approximation to the exact ABEP (6.43).

The diversity order i.e., the diversity gain of the inter-satellite laser link with respective to P_t, denoted as G_d, is defined as [11]

$$G_d = \frac{-\log P(e)}{\log P_t}|_{P_t\to\infty}.$$

Thus, from (6.48), the diversity order G_d is

$$G_d = s^2. \tag{6.50}$$

Note that G_d depends on the ratio s. More importantly, we cannot easily get the value of G_d from the exact ABEP expression (6.43).

Next, we show the values of C in (6.48), respectively, for different bounds. For the upper bound in (6.44), as γ increases, $\underline{\Gamma}\left(\frac{s^2-1}{2}, b_k\gamma {A_0}^2\right)$ can reduce to $\Gamma\left(\frac{s^2-1}{2}\right)$, since $\Gamma(.)$ is the gamma function defined as $\Gamma(\alpha) = \int_0^\infty e^{-t}t^{\alpha-1}dt$. Thus, (6.44) reduces to

$$P(e) \le P_{UB}(e) \approx \sum_{k=0}^{q} \frac{a_k s^2 \Gamma\left(\frac{s^2-1}{2}\right)}{2{A_0}^{s^2}} b_k^{\frac{1-s^2}{2}} \gamma^{-\frac{s^2}{2}}, \tag{6.51}$$

which is show to be a good approximation later. It thus follows that we obtain C in (6.48) as

$$C = \sum_{k=0}^{q} \frac{a_k s^2 \Gamma\left(\frac{s^2-1}{2}\right)}{2{A_0}^{s^2}} b_k^{\frac{1-s^2}{2}}. \tag{6.52}$$

Similarly, as γ increases, the lower bound in (6.45) can be well approximated as (6.48) with C given by

$$C = \sum_{k=1}^{q-1} \frac{c_k s^2 \Gamma\left(\frac{s^2+1}{2}\right)}{2{A_0}^{s^2}} d_k^{-\frac{1+s^2}{2}}. \tag{6.53}$$

For large γ, the bounds (6.46) and (6.47) can simplify to (6.48) with C, respectively, given as

$$C = \frac{s^2 \Gamma\left(\frac{s^2}{2}\right)}{8A_0^{s^2}} \left(\frac{(\sqrt{2})^{s^2}}{3} + (\sqrt{1.5})^{s^2} \right) \tag{6.54}$$

and

$$C = \frac{s^2 \Gamma\left(\frac{s^2}{2}\right)}{12A_0^{s^2}} \left(\frac{\sqrt{3}}{\pi} \right)^{-\frac{s^2}{2}} \left((\sqrt{2})^{-s^2} + 1 \right). \tag{6.55}$$

We can see that all the C above are constants related to A_0 and s.

Numerical Results

The system parameters used for numerical illustrations are given as follows: $R_{\text{data}} = 1$ Gbps, $z = 1000$ km, $r_c = 0.125$ m, and $N_0 = 2.2 \times 10^{-26}$ A^2/Hz (-174 dBm/Hz thermal noise passing through 179700 Ω load resistor [123]).

We set $q = 10$ and $(\epsilon_k - \epsilon_{k-1}) = 0.1$ here, which are sufficient for the accuracy of our results. The comparison with the exact ABEP in (6.43) in Fig. 6.4 shows that the bounds (6.44), (6.45), (6.46) and (6.47) are extremely tight in the whole transmit power region of interest. Eqs. (6.44) and (6.45) can be made arbitrarily tight by adjusting the parameters q and ϵ_k in (6.14), i.e., by increasing the number of sub-ranges, q, or shifting the partition points ϵ_k to make the values of $(\epsilon_k - \epsilon_{k-1})$ smaller.

Fig. 6.5 shows that for $\sigma_s = 50$m, the performance of all the invertible approximations (6.48) with different values of C asymptotically approaches to that

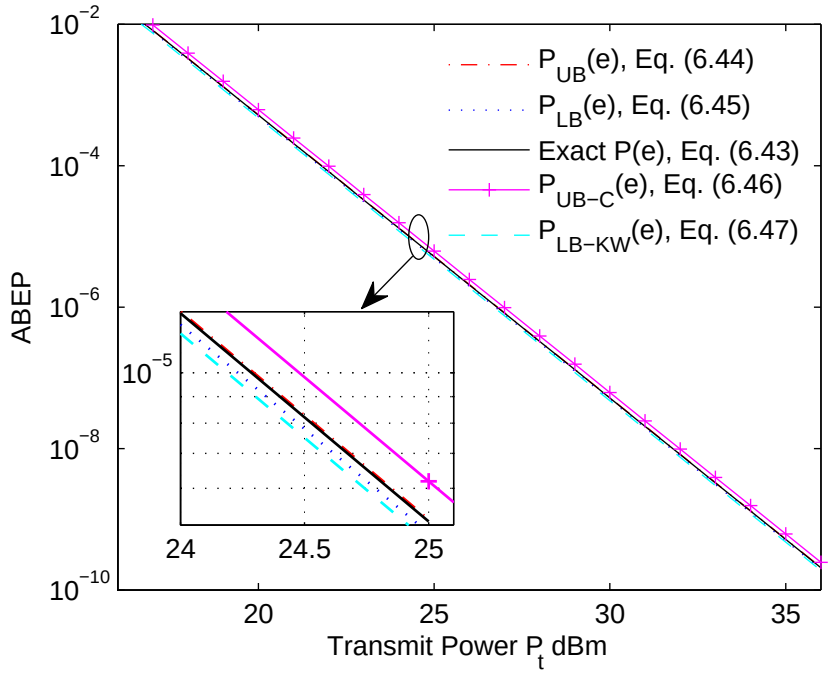

Figure 6.4: ABEP comparison as a function of P_t at $w_z = 400$ m, $\sigma_s = 100$m.

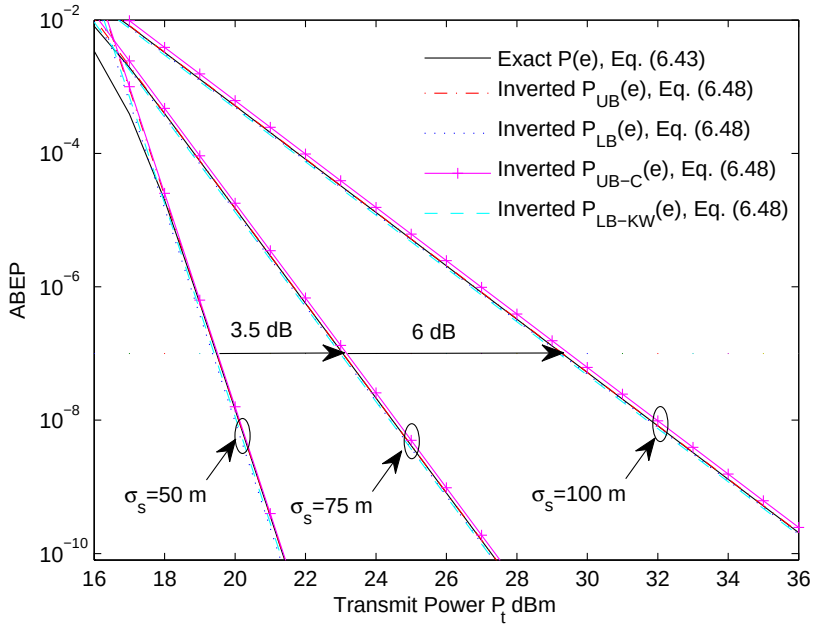

Figure 6.5: Invertible ABEP as a function of P_t for different σ_s at $w_z = 400$ m.

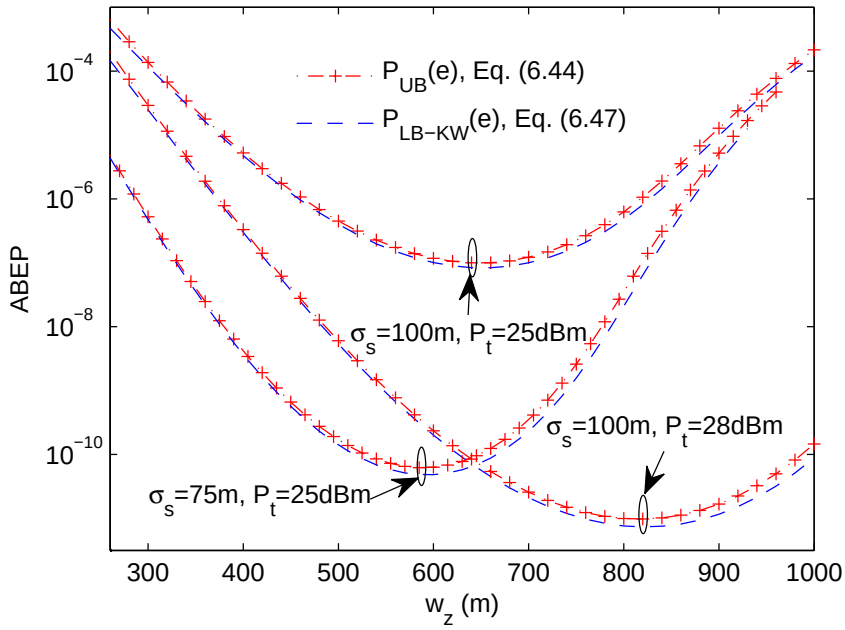

Figure 6.6: ABEP as a function of w_z for different P_t and σ_s.

of the exact ABEP (6.43). As σ_s increases, e.g., $\sigma_s = 75$m and 100m, (6.48) performs almost the same as (6.43) in the region of P_t corresponding to the ABEP values of 10^{-3} and lower, which are of practical interest. From Fig. 6.5, with the ABEP value of 10^{-7}, compared to the case of $\sigma_s = 50$m, the power penalties are 3.5dB and 9.5dB, respectively, for the cases of $\sigma_s = 75$m and 100m.

Furthermore, we explicitly show the effect of the beam radius w_z on the ABEP. We find that the transmit power P_t and standard jitter σ_s jointly decide the optimum value of w_z, the adjustment of which can be done by adjusting the transmitter beam waist according to (6.8). As shown in Fig. 6.6, the optimum values of w_z are 585m, 640m and 820m, respectively, for (σ_s, P_t) combinations to be (75m, 25dBm), (100m, 25dBm) and (100m, 28dBm). In some literatures, e.g., [86], there are wrong impressions that the ratio of w_z and σ_s, i.e., $\frac{w_z}{\sigma_s}$, can be optimized to a fixed value given a certain value of P_t. We hope to emphasize that this is not true from our observation. As given in our example, at $P_t = 25$dBm, the corresponding values of $\frac{w_z}{\sigma_s}$ are 7.8 and 6.4, respectively, for $\sigma_s = 75$m and 100m, which are obviously

non-identical.

6.4.2 Outage in Turbulent Channel with Pointing Errors

Similar to the case of K_G fading in Section 6.3.1, we show that the Gamma-Gamma distribution can be well approximated by the MG distribution [77]. Thus, the pdf of h_a in (6.6) can be rewritten in the form of the MG distribution, which is composed of a weighted sum of gamma distributions, given by

$$p_{h_a}(h_a) = \sum_{i=1}^{N} \alpha_i {h_a}^{\beta_i - 1} \exp(-\zeta_i h_a). \tag{6.56}$$

Here, N is the number of terms, and the parameters of the ith mixture gamma component α_i, β_i and ζ_i are given by [77, eq.(9)]:

$$\alpha_i = \frac{\theta_i}{\sum_{j=1}^{N} \theta_j \Gamma(\beta_j) \zeta_j^{-\beta_j}},\ \beta_i = m,\ \zeta_i = \frac{lm}{t_i},\ \theta_i = \frac{(lm)^m \omega_i t_i^{l-m-1}}{\Gamma(m)\Gamma(l)} \tag{6.57}$$

where t_i and ω_i are the abscissas and weight factors for the Gaussian-Laguerre integration given in [119].

For a turbulent channel with pointing errors, the channel gain is denoted as $h = h_a h_p$. Thus, its pdf can be derived as

$$p_h(h) = \int_{\frac{h}{A_0}}^{\infty} \frac{1}{a} p_{h_a}(a) p_{h_p}\left(\frac{h}{a}\right) da,\ h > 0 \tag{6.58}$$

Substituting (6.10) and (6.56) into (6.58), we have

$$\begin{aligned} p_h(h) &= \frac{s^2 h^{s^2-1}}{A_0^{s^2}} \sum_{i=1}^{N} \alpha_i \int_{\frac{h}{A_0}}^{\infty} a^{\beta_i - s^2 - 1} e^{-\zeta_i a} da \\ &= \frac{s^2 h^{s^2-1}}{A_0^{s^2}} \sum_{i=1}^{N} \alpha_i \zeta_i^{-\beta_i + s^2} \overline{\Gamma}(\beta_i - s^2, \zeta_i \frac{h}{A_0}) \end{aligned} \tag{6.59}$$

since we have $\overline{\Gamma}(\alpha, x) = \int_x^{\infty} e^{-t} t^{\alpha-1} dt$, where $\overline{\Gamma}(\cdot,\cdot)$ denotes the upper incomplete gamma function. This result (6.59) is an analytical and mathematically tractable

model for the channel gain.

The outage probability is defined as

$$P_{out} = P(h < I) = \int_0^I P_h(h)dh \tag{6.60}$$

where I denotes the threshold for outage. Based on $\int x^{b-1}\overline{\Gamma}(\alpha, x)dx = \frac{1}{b}\left[x^b\overline{\Gamma}(\alpha, x) - \overline{\Gamma}(\alpha + b, x)\right]$ with $b = s^2$, $\alpha = \beta_i - s^2$ and $x = \zeta_i \frac{h}{A_0}$, and substituting (6.59) in (6.60), P_{out} is thus derived as

$$P_{out} = \sum_{i=1}^{N} \alpha_i \zeta_i^{-\beta_i} \left[\left(\frac{\zeta_i C}{A_0}\right)^{s^2} \overline{\Gamma}(\beta_i - s^2, \frac{\zeta_i C}{A_0}) - \overline{\Gamma}(\beta_i, \frac{\zeta_i C}{A_0}) + \overline{\Gamma}(\beta_i, 0) \right] \tag{6.61}$$

where we have $\overline{\Gamma}(\beta_i, 0) = \Gamma(\beta_i)$. This outage probability result (6.61) is a novel, closed-form expression, compared with that in [88] for the strong turbulence case which is a very complex double integral.

The ASEP of this combined effect is also analyzed in [87]. Using this new model (6.59) for h, we can get the new ASEP result. For more details and numerical results, one can refer to [124].

6.5 Concluding Remarks

For wireless fading and FSO channels, models for different channel attenuation therein are introduced in detail, and we will mainly analyze the error performance.

In summary, tight, simple algebraic-form bounds and invertible expressions for the ASEP of MPSK are derived in a class of composite fading channels using the MG distribution. Our work can be extended straightforward to obtain the ABEP results for general MPSK, MDPSK or M-QAM, since all the conditional BEP results are approximated as linear combinations of single Gaussian Q-functions [125]. Our approach is more versatile with tight bounds and invertible expressions with no integral involved, and can be made arbitrarily accurate by adjusting the parameters q and ϵ_k. Our invertible results above with all $D = m$ in (6.22) shows that for

the Nakagami-m, K_G and NL composite fading models, the ASEP $P(\bar{\gamma})$ exhibits an asymptotic m-order diversity behaviour as a function of $\bar{\gamma}$.

Tight bounds on the ABEP are also derived for the inter-satellite link with pointing errors. These bounds can reduce to invertible approximations, and the diversity gain is straightforwardly obtained. We have studied the effect of the beam radius on the system ABEP. We also observe that with a fixed transmit power, the ratio of the beam waist and the standard jitter cannot be optimized to a fixed value. This bounding approach and the MG distribution can be further used to analyze the combined effects of atmospheric turbulence and pointing errors for terrestrial laser links, and to achieve analysable expression of outage probability.

Chapter 7

Summary of Contributions and Future Work

7.1 Summary of Contributions

In order to design a robust receiver for communication channels with Brownian motion carrier phase noise, we first apply the decision aided maximum likelihood (DA ML) phase estimation, and assume that the phase reference error (PRE) due to imperfect phase estimation is Gaussian distributed. We then consider the optimum detector design for two-dimensional carrier modulations received in AWGN and PRE. By viewing the AWGN as an equivalent additive observation phase noise (AOPN) model whose statistics is Tikhonov, we arrive at a unified received signal model in amplitude-phase form where the received phase incorporates the PRE and the AOPN. Using the amplitude and phase information of the received signal, the MAP/ML detection scheme is thus derived in amplitude-phase form. For one-ring constellations, the ML detector performs the same as the conventional MED detector which does not consider PRE. For multiple-ring constellations, simpler and closed-form approximations to the ML detector are given, which are shown in simulations to perform almost the same as the exact one. The approximately optimal decision regions can be easily determined using these detection rules. More importantly, when PRE exists, our approximate ML detectors perform much better than the suboptimal MED detector. For high SNR or large PRE variance, the ML detector asymptotically reduces to the suboptimal annular-sector (AS) detector which employs ring and phase detection separately. One can implement the AS detector in practice, even without the knowledge of the channel parameters: AWGN spectrum density and PRE variance. Our work provides a unified view of all the

existing suboptimal detectors in the presence of linear phase noise. Moreover, the SEP performance of all the detectors are compared to show the transition from one to the others. The amplitude-phase form facilitates error performance analysis and constellation optimization in phase noise.

For performance analysis in phase noise channel, we start on deriving the error probability of MPSK with coherent receiver using the ML detector. Then we generalize to differentially detected MDPSK with residual phase noise (RPN). The approach is that for high SNR, the Tikhonov pdf of the AOPN reduces to be approximately Gaussian. This AOPN can be combined with the PRE/RPN, and we obtain the Gaussian AOPN+PRE and AOPN+RPN models. Thus, the closed-form approximations to the error probability of MPSK and MDPSK are expressed as linear combinations of single Gaussian Q-functions. It is shown that our Gaussian AOPN+PRE/RPN model provides a simpler and quicker way to accurately estimate the error performance as a function of the phase error variance. Our unified approach is increasingly more accurate as M increases. Moreover, simple, accurate and closed-form approximations to the SEP of the AS detector are obtained for both 8-star QAM and the rotated case, 16QAM and even general M-APSK. These expressions provide explicit insight into how the PRE variance affects the performance. Within a wide range of PRE variances, our SEP approximations agree very well with the Monte Carlo simulations for all SNR values of interest. Besides, we can easily predict the error floor using these results. The closed-form results also facilitate the constellation optimization in phase noise, e.g., M-APSK optimization, where we should put more signal points on the outer ring to reduce the AOPN effect.

For performance analysis over fading, the bounds on the Gaussian Q-function we employ can be easily averaged over fading. Applying these bounds combined with the MG distribution which is used to approximate different fading models, we derive tight bounds and invertible average error probability expressions over composite fading channels. The tightness of the bounds can be improved by increasing the

number of summation terms or adjusting the coefficients. Our general expressions of ASEP are more efficient than the existing results in literature, for providing insights into how different channel parameters affect the performance. The results find applications in both wireless and optical communications. This bounding approach combined with the MG distribution further facilitates analysing the atmospheric turbulence and pointing error effects on FSO systems. Especially for inter-satellite links with pointing errors only, we derive the closed-form invertible approximations to the ASEP where we can easily get the diversity gain. Furthermore, a closed-form outage probability expression for the combined effects is obtained. We conclude that this approach is a very powerful tool in performance analysis, and it is applicable to a wider class of fading characteristics.

7.2 Future Work

7.2.1 The Nonlinear Phase Noise Channel

It should be noted that our results in this thesis are for linear phase noise. In coherent fiber-optical transmission systems using inline amplifiers, the interaction of a signal and amplifier noise through the Kerr effect leads to nonlinear phase noise that can impair the detection of phase-modulated signals [49]. In nonlinear phase noise, references [49, 51–53] have considered receiver-based detection or compensation techniques, the impact of fiber nonlinearities on system performance, and the optimization of APSK constellations. Besides, [105] obtained the (nonlinear) optimal DB by applying the expectation maximization algorithm to compensate for the distortion and phase shift on the constellations.

In the nonlinear phase noise channel, imperfect phase estimation algorithms are also used to track the nonlinear phase, which leads to a phase estimation error. We thus want to see how the use of the amplitude and phase information of the received signal facilitates the receiver design and performance analysis with the phase estimation error. Combining our amplitude-phase approach with the

statistical model for the nonlinear phase noise proposed in [103], we will first arrive at an optimum amplitude-phase-form receiver structure, and then do error probability analysis in the presence of nonlinear phase noise in the future. One should expect that the error probability results with tractable forms can make constellation optimization much more efficiently.

7.2.2 Differential Amplitude/Phase Modulation

In practical cases where transmission over fading channels has to be performed without having channel state information and/or reliable carrier phase estimation at the receiver, differential encoding at the transmitter and non-coherent reception are proved to be advantageous. Moreover, to achieve higher spectrum efficiencies, mixed phase and amplitude modulation can be used. A straightforward extension of classical DPSK is to transmit information both in phase and in amplitude changes. This scheme is known as differential amplitude and phase-shift keying (DAPSK) [126–129].

For low receiver complexity, we may first consider detector design in amplitude-phase form, by using only two consecutively received signals with taking the previous signal as the reference to do differential detection [130]. Differential encoding rules given in [131–133] are considered. We will use the amplitude-phase-form approach to do performance analysis and optimization for differential amplitude/phase modulated signals with linear phase noise. The analysis can be extended to the nonlinear phase noise channel [61, 62].

7.2.3 Subcarrier FSO Systems

Subcarrier FSO systems become popular recently, since such a system can employ a variety of modulation schemes (coherent or noncoherent or differentially coherent modulation) at the electrical modulator [134–136]. The channel is affected by both unknown phase noise and fading. Therefore, we may consider receiver design and performance analysis with the combined effects.

As shown in Chap. 4, the new SEP results for MPSK, M-QAM and M-APSK with PRE, and for MDPSK with RPN are all expressed in terms of Gaussian Q-functions. Therefore, using the MG distribution to approximate the fading model here and combining with our bounding approach, the average error probability of subcarrier systems with carrier phase noise in turbulence channels can be directly analyzed. The results may provide better insights into how the channel parameters affect the system performance.

7.2.4 Fading Channels with Oscillator Phase Noise

Due to the unprecedented explosion in the number of wireless and mobile devices, there is renewed interest in the issue of oscillator phase noise in recent times. Performance monitoring or channel estimation in the presence of oscillator phase noise has become a hot issue. The impact of oscillator phase noise on the performance of multiple-input multiple-output systems is an important problem, and yet a big challenge. More and more researchers would like to analyze the effect of phase noise on receiver performance. However, recent references [10,94,95] and those therein usually assume quasi-static fading channels, where the coefficient $h(k)$ is assumed to be deterministic, time-invariant, and known to the receiver, as we do in the main thesis.

In practice, it is common that both time-varying fading and oscillator phase noise occur and impair the system performance together. Studying the combined effects is a challenge for the future, and yet no good solution is currently available.

References

[1] G. P. Agrawal, *Fiber-Optic Communication Systems.* Wiley Online Library, 2002.

[2] K.-P. Ho, *Phase-modulated Optical Communication Systems.* New York: Springer, 2005.

[3] H. Nakashima, T. Tanimura, T. Hoshida, S. Oda, J. C. Rasmussen, L. Li, Z. Tao, Y. Ishii, K. Shiota, K. Sugitani *et al.*, "Novel wide-range frequency offset compensator demonstrated with real-time digital coherent receiver," in *in Proc. ECOC, 2008, Mo.3.D.4.*, 2008.

[4] E. Ip and J. M. Kahn, "Compensation of dispersion and nonlinear impairments using digital backpropagation," *J. Lightw. Technol.*, vol. 26, no. 20, pp. 3416–3425, 2008.

[5] A. Demir, "Nonlinear phase noise in optical-fiber-communication systems," *J. Lightw. Technol.*, vol. 25, no. 8, pp. 2002–2032, 2007.

[6] S. Arnon, J. Barry, G. Karagiannidis, R. Schober, and M. Uysal, *Advanced Optical Wireless Communication Systems.* Cambridge university press, 2012.

[7] M. R. Khanzadi, H. Mehrpouyan, E. Alpman, T. Svensson, D. Kuylenstierna, and T. Eriksson, "On models, bounds, and estimation algorithms for time-varying phase noise," in *5th Int. Conf. Signal Process. Commun. Syst. (ICSPCS)*, 2011, pp. 1–8.

[8] M. R. Khanzadi, R. Krishnan, D. Kuylenstierna, and T. Eriksson, "Oscillator phase noise and small-scale channel fading in higher frequency bands," in *IEEE Globecom Workshops*, 2014, pp. 410–415.

[9] M. R. Khanzadi, R. Krishnan, and T. Eriksson, "Receiver algorithm based on differential signaling for SIMO phase noise channels with common and separate oscillator configurations," in *IEEE Global Commun. Conf. (GLOBECOM)*, 2015, pp. 1–6.

[10] R. Krishnan, G. Colavolpe, A. G. i Amat, and T. Eriksson, "Algorithms for joint phase estimation and decoding for MIMO systems in the presence of

phase noise and quasi-static fading channels," *IEEE Trans. Signal Process.*, vol. 63, no. 13, pp. 3360–3375, 2015.

[11] A. Goldsmith, *Wireless Communications.* Cambridge university press, 2005.

[12] M. K. Simon and M.-S. Alouini, *Digital Communication over Fading Channels.* John Wiley & Sons, 2005.

[13] D. Tse and P. Viswanath, *Fundamentals of Wireless Communication.* Cambridge university press, 2005.

[14] J. G. Proakis, *Digital Communications.* 5th ed. New-York: McGraw-Hill, 2007.

[15] S. Zhang, P. Y. Kam, C. Yu, and J. Chen, "Decision-aided carrier phase estimation for coherent optical communications," *J. Lightw. Technol.*, vol. 28, no. 11, pp. 1597–1607, 2010.

[16] C. Xu, X. Liu, and X. Wei, "Differential phase-shift keying for high spectral efficiency optical transmissions," *IEEE J. Sel. Top. Quantum Electron.*, vol. 10, no. 2, pp. 281–293, 2004.

[17] A. H. Gnauck and P. J. Winzer, "Optical phase-shift-keyed transmission," *J. Lightw. Technol.*, vol. 23, no. 1, p. 115, Jan 2005.

[18] R.-J. Essiambre, G. Kramer, P. J. Winzer, G. J. Foschini, and B. Goebel, "Capacity limits of optical fiber networks," *J. Lightw. Technol.*, vol. 28, no. 4, pp. 662–701, 2010.

[19] E. Agrell and M. Karlsson, "Power-efficient modulation formats in coherent transmission systems," *J. Lightw. Technol.*, vol. 27, no. 22, pp. 5115–5126, 2009.

[20] C. Thomas, M. Weidner, and S. Durrani, "Digital amplitude-phase keying with M-ary alphabets," *IEEE Trans. Commun.*, vol. 22, no. 2, pp. 168–180, 1974.

[21] S. L. Miller and R. J. O'Dea, "Peak power and bandwidth efficient linear modulation," *IEEE Trans. Commun.*, vol. 46, no. 12, pp. 1639–1648, 1998.

[22] Y. Zhou, P. J. McLane, and C. Loo, "Performance of predistorted APK modulation for one- and two-link nonlinear power amplifier satellite communication channels," *IEEE Trans. Vehicular Tech.*, vol. 54, no. 2, pp. 629–638, 2005.

[23] R. De Gaudenzi, A. Guillen i Fabregas, and A. Martinez, "Performance analysis of turbo-coded APSK modulations over nonlinear satellite channels," *IEEE Trans. Wireless Commun.*, vol. 5, no. 9, pp. 2396–2407, 2006.

[24] K. Yan, F. Yang, J. Song, F. Ren, and J. Li, "A framework of APSK constellation labeling design for satellite transmission," in *ICC*. IEEE, 2014, pp. 4337–4341.

[25] M. Seimetz, M. Noelle, and E. Patzak, "Optical systems with high-order DPSK and star QAM modulation based on interferometric direct detection," *J. Lightw. Technol.*, vol. 25, no. 6, pp. 1515–1530, 2007.

[26] H. Zhang, P. Y. Kam, and C. Yu, "Performance analysis of coherent optical 8-star QAM systems using decision-aided maximum likelihood phase estimation," *Opt. Express*, vol. 20, no. 8, pp. 9302–9311, 2012.

[27] M. Seimetz, "Laser linewidth limitations for optical systems with high-order modulation employing feed forward digital carrier phase estimation," in *Optical Fiber Commun. Conf.*, 2008, p. OTuM2.

[28] S. Zhang, P. Kam, C. Yu, and J. Chen, "Laser linewidth tolerance of decision-aided maximum likelihood phase estimation in coherent optical M-ary PSK and QAM systems," *IEEE Photon. Technol. Lett.*, vol. 21, no. 15, pp. 1075–1077, 2009.

[29] M. R. Khanzadi, R. Krishnan, and T. Eriksson, "Estimation of phase noise in oscillators with colored noise sources," *IEEE Commun. Lett.*, vol. 17, no. 11, pp. 2160–2163, 2013.

[30] R. Noe, "PLL-free synchronous QPSK polarization multiplex/diversity receiver concept with digital i&q baseband processing," *IEEE Photon. Technol. Lett.*, vol. 17, no. 4, pp. 887–889, 2005.

[31] S. J. Savory, "Digital filters for coherent optical receivers," *Opt. Express*, vol. 16, no. 2, pp. 804–817, 2008.

[32] E. Ip and J. M. Kahn, "Feedforward carrier recovery for coherent optical communications," *J. Lightw. Technol.*, vol. 25, no. 9, pp. 2675–2692, 2007.

[33] M. Taylor, "Accurate digital phase estimation process for coherent detection using a parallel digital processor," in *Proc. ECOC*, vol. 2, 2005, pp. 263–264.

[34] L. Pessoa, H. Salgado, and I. Darwazeh, "Joint mitigation of optical impairments and phase estimation in coherent optical systems," in *Proc. IEEE LEOS Summer Topical Meetings*, 2008, pp. 169–170.

[35] A. Viterbi and A. Viterbi, "Nonlinear estimation of PSK-modulated carrier phase with application to burst digital transmission," *IEEE Trans. Inf. Theory*, vol. 29, no. 4, pp. 543–551, 1983.

[36] F. Rice, M. Rice, and B. Cowley, "A new algorithm for 16QAM carrier phase estimation using QPSK partitioning," *Digital Signal Processing*, vol. 12, no. 1, pp. 77–86, 2002.

[37] H. Louchet, K. Kuzmin, and A. Richter, "Improved DSP algorithms for coherent 16-QAM transmission," in *Proc. ECOC*, 2008, p. Tu.1.E.6.

[38] D.-S. Ly-Gagnon, S. Tsukamoto, K. Katoh, and K. Kikuchi, "Coherent detection of optical quadrature phase-shift keying signals with carrier phase estimation," *J. Lightw. Technol.*, vol. 24, no. 1, p. 12, 2006.

[39] S. Zhang, P. Y. Kam, and C. Yu, "Block length effect of decision-aided maximum likelihood phase estimation in coherent optical communication systems," in *Lasers and Electro-Optics Conf.*, 2009, p. CMZ3.

[40] S. Zhang, P. Kam, J. Chen, and C. Yu, "Decision-aided maximum likelihood detection in coherent optical phase-shift-keying system," *Opt. express*, vol. 17, no. 2, pp. 703–715, 2009.

[41] P. Y. Kam and C. H. Teh, "Reception of PSK signals over fading channels via quadrature amplitude estimation," *IEEE Trans. Commun.*, vol. 31, no. 8, pp. 1024–1027, 1983.

[42] P. Y. Kam, "Optimal detection of digital data over the nonselective Rayleigh fading channel with diversity reception," *IEEE Trans. Commun.*, vol. 39, no. 2, pp. 214–219, 1991.

[43] D. Divsalar and M. K. Simon, "Maximum-likelihood differential detection of uncoded and trellis coded amplitude phase modulation over AWGN and fading channels- metrics and performance," *IEEE Trans. Commun.*, vol. 42, no. 1, pp. 76–89, 1994.

[44] G. Colavolpe and R. Raheli, "Noncoherent sequence detection in frequency nonselective slowly fading channels," *IEEE J. Select. Areas. Commun.*, vol. 18, no. 11, pp. 2302–2311, 2000.

[45] P. Y. Kam, "Maximum likelihood carrier phase recovery for linear suppressed-carrier digital data modulations," *IEEE Trans. Commun.*, vol. 34, no. 6, pp. 522–527, 1986.

[46] P. Y. Kam, S. K. Teo, Y. K. Some, and T. T. Tjhung, "Approximate results for the bit error probability of binary phase shift keying with noisy phase reference," *IEEE Trans. Commun.*, vol. 41, pp. 1020–1022, 1993.

[47] J. Kahn, "Modulation and detection techniques for optical communication systems," in *Coherent Optical Technologies and Applications*, 2006, p. CThC1.

[48] P. Y. Kam, S. S. Ng, and T. S. Ng, "Optimum symbol-by-symbol detection of uncoded digital data over the gaussian channel with unknown carrier phase," *IEEE Trans. Commun.*, vol. 42, no. 8, pp. 2543–2552, 1994.

[49] A. P. T. Lau and J. M. Kahn, "Signal design and detection in presence of nonlinear phase noise," *J. Lightw. Technol.*, vol. 25, no. 10, pp. 3008–3016, 2007.

[50] R. Krishnan, M. R. Khanzadi, T. Eriksson, and T. Svensson, "Soft metrics and their performance analysis for optimal data detection in the presence of strong oscillator phase noise," *IEEE Trans. Commun.*, no. 6, pp. 2385–2395, 2013.

[51] N. Ekanayake and H. Herath, "Effect of nonlinear phase noise on the performance of M-ary PSK signals in optical fiber links," *J. Lightw. Technol.*, vol. 31, no. 3, pp. 447–454, Feb 2013.

[52] L. Beygi, E. Agrell, and M. Karlsson, "Optimization of 16-point ring constellations in the presence of nonlinear phase noise," in *Opt. Fiber Commun. Conf.*, 2011, p. OThO4.

[53] C. Hager, A. Graell i Amat, A. Alvarado, and E. Agrell, "Design of APSK constellations for coherent optical channels with nonlinear phase noise," *IEEE Trans. Commun.*, vol. 61, no. 8, pp. 3362–3373, August 2013.

[54] K. Kikuchi, T. Okoshi, M. Nagamatsu, and H. Henmi, "Degradation of bit-error rate in coherent optical communications due to spectral spread of the transmitter and the local oscillator," *J. Lightw. Technol.*, vol. 2, no. 6, pp. 1024–1033, 1984.

[55] Y. K. Some and P. Y. Kam, "Bit-error probability of QPSK with noisy phase reference," *IEE Proceedings-Commun.*, vol. 142, no. 5, pp. 292–296, 1995.

[56] M. A. Najib and V. K. Prabhu, "Lower bounds on error performance for BPSK and QPSK systems with imperfect carrier phase recovery," in *Communications, 1998. ICC 98.*, vol. 3, 1998, pp. 1253–1258.

[57] M. P. Fitz and R.-M. Cramer, "A performance analysis of a digital PLL based MPSK demodulator," *IEEE Trans. Commun.*, vol. 43, no. 234, pp. 1192–1201, 1995.

[58] C. Yu, S. Zhang, P. Y. Kam, and J. Chen, "Bit-error rate performance of coherent optical M-ary PSK/QAM using decision-aided maximum likelihood phase estimation," *Opt. Express*, vol. 18, no. 12, pp. 12 088–12 103, 2010.

[59] Y. Jang, D. Yoon, and S.-K. Lee, "Generalized BER expression of MPSK in the presence of phase error," *Commun. Lett.*, vol. 17, no. 12, pp. 2213–2216, 2013.

[60] P. Y. Kam, K. Y. Seek, T. T. Tjhung, and P. Sinha, "Error probability of 2DPSK with phase noise," *IEEE Trans. Commun.*, vol. 42, no. 7, pp. 2366–2369, 1994.

[61] K.-P. Ho, "Error probability of DPSK signals with cross-phase modulation induced nonlinear phase noise," *IEEE J. Sel. Top. Quantum Electron.*, vol. 10, no. 2, pp. 421–427, March 2004.

[62] ——, "Impact of nonlinear phase noise to DPSK signals: a comparison of different models," *IEEE Photon. Technol. Lett.*, vol. 16, no. 5, pp. 1403–1405, May 2004.

[63] N. M. Blachman, "The effect of phase error on DPSK error probability," *IEEE Trans. Commun.*, vol. 29, no. 3, pp. 364–365, Mar 1981.

[64] P. Mary, M. Dohler, J.-M. Gorce, G. Villemaud, and M. Arndt, "M-ary symbol error outage over Nakagami-m fading channels in shadowing environments," *IEEE Trans. Commun.*, vol. 57, no. 10, pp. 2876–2879, 2009.

[65] ——, "BPSK bit error outage over Nakagami-m fading channels in lognormal shadowing environments," *IEEE Commun. Lett.*, vol. 11, no. 7, pp. 565–567, 2007.

[66] A. Conti, M. Z. Win, and M. Chiani, "On the inverse symbol-error probability for diversity reception," *IEEE Trans. Commun.*, vol. 51, no. 5, pp. 753–756, 2003.

[67] M. K. Simon and M.-S. Alouini, "A unified approach to the performance analysis of digital communication over generalized fading channels," *Proc. IEEE*, vol. 86, no. 9, pp. 1860–1877, 1998.

[68] H. Shin and J. H. Lee, "On the error probability of binary and M-ary signals in Nakagami-m fading channels," *IEEE Trans. Commun.*, vol. 52, no. 4, pp. 536–539, 2004.

[69] Q. Shi and Y. Karasawa, "An accurate and efficient approximation to the Gaussian Q-function and its applications in performance analysis in Nakagami-m fading," *IEEE Commun. Lett.*, vol. 15, no. 5, pp. 479–481, 2011.

[70] P. Loskot and N. C. Beaulieu, "Prony and polynomial approximations for evaluation of the average probability of error over slow-fading channels," *IEEE Trans. Vehicular Tech.*, vol. 58, no. 3, pp. 1269–1280, 2009.

[71] J. W. Craig, "A new, simple and exact result for calculating the probability of error for two-dimensional signal constellations," *Military Commun. Conf. MILCOM'91*, pp. 571–575, 1991.

[72] H. Fu, M.-W. Wu, and P.-Y. Kam, "Explicit, closed-form performance analysis in fading via new bound on Gaussian Q-function," in *IEEE ICC Wireless Commun. Symp.*, 2013, pp. 5819–5823.

[73] ——, "Lower bound on averages of the product of L Gaussian Q-functions over Nakagami-m fading," in *VTC-Spring. IEEE 77th*, 2013, pp. 1–5.

[74] M. Chiani, D. Dardari, and M. K. Simon, "New exponential bounds and approximations for the computation of error probability in fading channels," *IEEE Trans. Wireless Commun.*, vol. 2, no. 4, pp. 840–845, 2003.

[75] M. Wu, X. Lin, and P.-Y. Kam, "New exponential lower bounds on the Gaussian Q-function via Jensen's inequality," in *Vehicular Tech. Conf. (VTC Spring)*. IEEE, 2011, pp. 1–5.

[76] A. Laourine, M.-S. Alouini, S. Affes, and A. Stéphenne, "On the performance analysis of composite multipath/shadowing channels using the G-distribution," *IEEE Trans. Commun.*, vol. 57, no. 4, pp. 1162–1170, 2009.

[77] S. Atapattu, C. Tellambura, and H. Jiang, "A mixture gamma distribution to model the SNR of wireless channels," *IEEE Trans. Wireless Commun.*, vol. 10, no. 12, pp. 4193–4203, 2011.

[78] O. Alhussein, S. Muhaidat, J. Liang, and P. D. Yoo, "A unified approach for representing wireless channels using EM-based finite mixture of gamma distributions," in *Globecom Workshops*, 2014, pp. 1008–1013.

[79] B. Selim, O. Alhussein, S. Muhaidat, G. K. Karagiannidis, and J. Liang, "Modeling and analysis of wireless channels via the mixture of gaussian distribution," *arXiv preprint arXiv:1503.00877*, 2015.

[80] Y. Jeong, H. Shin, and M. Z. Win, "H-fading: Towards H-transform theory for wireless communication," in *European Networks and Commun. Conf. (EuCNC)*, 2015, pp. 26–30.

[81] W. Cheng, "Performance analysis and comparison of dual-hop amplify-and-forward relaying over mixture gamma and generalized-k fading channels," in *International Conf. WCSP*, 2013, pp. 1–6.

[82] J. Jung, S.-R. Lee, H. Park, S. Lee, and I. Lee, "Capacity and error probability analysis of diversity reception schemes over generalized-K fading channels using a mixture gamma distribution," *IEEE Trans. Wireless Commun.*, vol. 13, no. 9, pp. 4721–4730, 2014.

[83] J. Jung, S.-R. Lee, H. Park, H. Lee, and I. Lee, "A PDF-based capacity analysis of diversity reception schemes over composite fading channels using a mixture gamma distribution," in *Vehicular Technol. Conf. (VTC Fall)*, 2014, pp. 1–5.

[84] A. A. Hammadi and et al, "Unified analysis of cooperative spectrum sensing over composite and generalized fading channels," *arXiv preprint arXiv:1503.01415*, 2015.

[85] A. Agrawal and R. S. Kshetrimayum, "Analysis of UWB communication over IEEE 802.15. 3a channel by superseding lognormal shadowing by Mixture of Gamma distributions," *AEU-International J. Electron. and Commun.*, 2015.

[86] M. Toyoshima, T. Jono, K. Nakagawa, and A. Yamamoto, "Optimum divergence angle of a Gaussian beam wave in the presence of random jitter in free-space laser communication systems," *JOSA A*, vol. 19, no. 3, pp. 567–571, 2002.

[87] H. G. Sandalidis, T. Tsiftsis, G. K. Karagiannidis, M. Uysal *et al.*, "BER performance of FSO links over strong atmospheric turbulence channels with pointing errors," *Commun. Lett.*, vol. 12, no. 1, pp. 44–46, 2008.

[88] A. Farid, S. Hranilovic *et al.*, "Outage capacity optimization for free-space optical links with pointing errors," *J. Lightw. Technol.*, vol. 25, no. 7, pp. 1702–1710, 2007.

[89] J. Ma, Y. Jiang, L. Tan, S. Yu, and W. Du, "Influence of beam wander on bit-error rate in a ground-to-satellite laser uplink communication system," *Optics lett.*, vol. 33, no. 22, pp. 2611–2613, 2008.

[90] H. Guo, B. Luo, Y. Ren, S. Zhao, and A. Dang, "Influence of beam wander on uplink of ground-to-satellite laser communication and optimization for transmitter beam radius," *Optics lett.*, vol. 35, no. 12, pp. 1977–1979, 2010.

[91] Q. Wang and P. Y. Kam, "Simple, unified, and accurate prediction of error probability for higher order MPSK/MDPSK with phase noise in optical communications," *J. Lightw. Technol.*, vol. 32, no. 21, pp. 3531–3540, Nov. 2014.

[92] R. F. Pawula, S. Rice, and J. Roberts, "Distribution of the phase angle between two vectors perturbed by Gaussian noise," *IEEE Trans. Commun.*, vol. 30, no. 8, pp. 1828–1841, 1982.

[93] Q. Wang and P. Y. Kam, "Optimum detection of two-dimensional carrier modulations with linear phase noise using received amplitude and phase information and performance analysis," *J. Lightw. Technol.*, vol. 34, no. 10, pp. 2439–2451, May 2016.

[94] M. R. Khanzadi, G. Durisi, and T. Eriksson, "Capacity of SIMO and MISO phase-noise channels with common/separate oscillators," *IEEE Trans. Commun.*, vol. 63, no. 9, pp. 3218–3231, 2015.

[95] R. Krishnan, M. R. Khanzadi, N. Krishnan, Y. Wu, A. G. i Amat, T. Eriksson, and R. Schober, "Linear massive MIMO precoders in the presence of phase noiseA large-scale analysis," *IEEE Trans. Commun.*, vol. 65, no. 5, pp. 3057–3071, 2016.

[96] G. Colavolpe, A. Barbieri, and G. Caire, "Algorithms for iterative decoding in the presence of strong phase noise," *IEEE J. Sel. Areas Commun.*, vol. 23, no. 9, pp. 1748–1757, 2005.

[97] M. R. Khanzadi, D. Kuylenstierna, A. Panahi, T. Eriksson, and H. Zirath, "Calculation of the performance of communication systems from measured oscillator phase noise," *IEEE Trans. Circuits Syst. I, Reg. Papers*, vol. 61, no. 5, pp. 1553–1565, 2014.

[98] H. Mehrpouyan, M. R. Khanzadi, M. Matthaiou, A. M. Sayeed, R. Schober, and Y. Hua, "Improving bandwidth efficiency in E-band communication systems," *IEEE Commun. Mag.*, vol. 52, no. 3, pp. 121–128, 2014.

[99] G. Nicholson, "Probability of error for optical heterodyne DPSK system with quantum phase noise," *Electron. Lett.*, vol. 24, no. 20, pp. 1005–1007, 1984.

[100] A. J. Viterbi, *Principles of coherent communication.* New York: McGraw-Hill, 1966.

[101] H. L. Van Trees, *Detection, Estimation and Modulation Theory: Part I.* New York: Wiley, 1968.

[102] H. Fu and P. Y. Kam, "Phase-based, time-domain estimation of the frequency and phase of a single sinusoid in AWGN-the role and applications of the additive observation phase noise model," *IEEE Trans. Inf. Theory*, vol. 59, no. 5, pp. 3175–3188, May 2013.

[103] P. Poggiolini, "The GN model of non-linear propagation in uncompensated coherent optical systems," *J. Lightw. Technol.*, vol. 30, no. 24, pp. 3857–3879, 2012.

[104] E. Ip and J. M. Kahn, "Carrier synchronization for 3-and 4-bit-per-symbol optical transmission," *J. Lightw. Technol.*, vol. 23, no. 12, pp. 4110–4124, 2005.

[105] D. Zibar, O. Winther, N. Franceschi, R. Borkowski, A. Caballero, V. Arlunno, M. N. Schmidt, N. G. Gonzales, B. Mao, Y. Ye *et al.*, "Nonlinear impairment compensation using expectation maximization for dispersion managed and unmanaged PDM 16-QAM transmission," *Optics express*, vol. 20, no. 26, pp. B181–B196, 2012.

[106] P. Lee, "Computation of the bit error rate of coherent M-ary PSK with Gray code bit mapping," *IEEE Trans. Commun.*, vol. 34, pp. 488–491, 1986.

[107] J. Lassing, E. G. Strom, E. Agrell, and T. Ottosson, "Computation of the exact bit-error rate of coherent M-ary PSK with Gray code bit mapping," *IEEE Trans. Commun.*, vol. 51, no. 11, pp. 1758–1760, 2003.

[108] L. Franks, "Synchronization subsystems: analysis and design," *Digital Commun.: Satellite/Earth Station Engineering*, pp. 294–335, 1983.

[109] R. Krishnan, A. Graell i Amat, T. Eriksson, and G. Colavolpe, "Constellation optimization in the presence of strong phase noise," *IEEE Trans. Commun.*, vol. 61, no. 12, pp. 5056–5066, 2013.

[110] T. Freckmann, R. Essiambre, P. Winzer, G. Foschini, and G. Kramer, "Fiber capacity limits with optimized ring constellations," *IEEE Photon. Technol. Lett.*, vol. 21, no. 20, pp. 1496–1498, 2009.

[111] F. Kayhan and G. Montorsi, "Constellation design for memoryless phase noise channels," *IEEE Trans. Wireless Commun.*, vol. 13, no. 5, pp. 2874–2883, 2014.

[112] T. Song and P.-Y. Kam, "A robust GLRT receiver with implicit channel estimation and automatic threshold adjustment for the free space optical channel with IM/DD," *J. Lightw. Technol.*, vol. 32, no. 3, pp. 369–383, 2014.

[113] P. S. Bithas, N. C. Sagias, P. T. Mathiopoulos, G. K. Karagiannidis, A. Rontogiannis *et al.*, "On the performance analysis of digital communications over generalized-k fading channels," *IEEE Commun. Lett.*, vol. 10, no. 5, pp. 353–355, 2006.

[114] D. K. Borah and D. G. Voelz, "Pointing error effects on free-space optical communication links in the presence of atmospheric turbulence," *J. Lightw. Technol.*, vol. 27, no. 18, pp. 3965–3973, 2009.

[115] M. Riediger, R. Schober, and L. Lampe, "Blind detection of on-off keying for free-space optical communications," in *Electrical and Computer Engineering, 2008. CCECE 2008. Canadian Conference on.* IEEE, 2008, pp. 001 361–001 364.

[116] M. Al-Habash, L. C. Andrews, and R. L. Phillips, "Mathematical model for the irradiance probability density function of a laser beam propagating through turbulent media," *Optical Engineering*, vol. 40, no. 8, pp. 1554–1562, 2001.

[117] M. A. Bandres and J. C. Gutiérrez-Vega, "Ince-Gaussian beams," *Optics lett.*, vol. 29, no. 2, pp. 144–146, 2004.

[118] A. E. Siegman, *Lasers.* University Science Books, 1986.

[119] M. Abramowitz and I. A. Stegun, *Handbook of mathematical functions: with formulas, graphs, and mathematical tables.* Courier Corporation, 1964.

[120] Z. Wang and G. B. Giannakis, "A simple and general parameterization quantifying performance in fading channels," *IEEE Trans. Commun.*, vol. 51, no. 8, pp. 1389–1398, 2003.

[121] J. Jung, S.-R. Lee, H. Park, and I. Lee, "Diversity analysis over composite fading channels using a mixture gamma distribution," in *IEEE ICC Wireless Commun. Symp.*, 2013, pp. 5824–5828.

[122] T. Song and P.-Y. Kam, "Efficient symbol detection for the FSO IM/DD system with automatic and adaptive threshold adjustment: The multi-level pam case," *arXiv preprint arXiv:1505.02536*, 2015.

[123] S. Dolinar, D. Divsalar, J. Hamkins, and F. Pollara, "Capacity of pulse-position modulation (PPM) on Gaussian and Webb channels," *Jet Propulsion Lab., Pasadena, CA, USA, TMO Progr. Rep.*, 2000.

[124] H. G. Sandalidis, "A versatile model for turbulence and pointing error effects in FSO systems," in *WCNC 2016*. IEEE, 2016, pp. 001 361–001 364.

[125] J. Lu, K. B. Letaief, J. C. Chuang, and M. L. Liou, "M-PSK and M-QAM BER computation using signal-space concepts," *IEEE Trans. Commun.*, vol. 47, no. 2, pp. 181–184, 1999.

[126] N. A. B. Svensson, "On differentially encoded star 16QAM with differential detection and diversity," *IEEE Trans. Vehicular Tech.*, vol. 44, no. 3, pp. 586–593, 1995.

[127] R. Fischer, L. H.-J. Lampe, S. Muller-Weinfurtner, and J. B. Huber, "Coded modulation for differential encoding and non-coherent reception on fading channels," *ITG FACHBERICHT*, pp. 139–146, 2000.

[128] Y.-M. Chen and Y.-L. Ueng, "Noncoherent amplitude/phase modulated transmission schemes for rayleigh block fading channels," *IEEE Trans. Commun.*, vol. 61, no. 1, pp. 217–227, 2013.

[129] ——, "Differential amplitude/phase modulation for correlated rayleigh fading channels: Performance analysis and labeling design," *IEEE Trans. Commun.*, vol. 62, no. 8, pp. 2927–2938, 2014.

[130] H. Yuan and P.-Y. Kam, "On the LLR metrics for DPSK modulations over two-symbol observation intervals for the flat rician fading channel," *IEEE Trans. Commun.*, vol. 63, no. 12, pp. 4950–4963, 2015.

[131] D. Warrier and U. Madhow, "Spectrally efficient noncoherent communication," *IEEE Trans. Inf. Theory*, vol. 48, no. 3, pp. 651–668, 2002.

[132] R.-Y. Wei, "Differential encoding by a look-up table for quadrature-amplitude modulation," *IEEE Trans. Commun.*, vol. 59, no. 1, pp. 84–94, 2011.

[133] R.-Y. Wei, S.-S. Gu, and T.-C. Sue, "Noncoherent block-coded TAPSK," *IEEE Trans. Commun.*, vol. 57, no. 11, pp. 3195–3198, 2009.

[134] X. Song, F. Yang, J. Cheng, and M.-S. Alouini, "Ber of subcarrier mpsk and mdpsk systems in atmospheric turbulence," *J. Lightw. Technol.*, vol. 33, no. 1, pp. 161–170, 2015.

[135] X. Song, F. Yang, J. Cheng, N. Al-Dhahir, and Z. Xu, "Subcarrier phase-shift keying systems with phase errors in lognormal turbulence channels," *J. Lightw. Technol.*, vol. 33, no. 9, pp. 1896–1904, 2015.

[136] C. Xu, J. Cheng, and H. Zhang, "Performance of subcarrier PSK systems using PSAM maximum likelihood estimation in turbulence channels," *J. Lightw. Technol.*, vol. 34, no. 9, pp. 2267–2279, 2016.

List of Publications

1. Q. Wang and P. Y. Kam, "Simple, unified, and accurate prediction of error probability for higher order MPSK/MDPSK with phase noise in optical communications", *J. Lightw. Technol.,* vol. 32, no. 21, pp. 3531–3540, Nov. 2014.

2. Q. Wang, H. Lin and P. Y. Kam, "Tight bounds and invertible average error probability expressions over composite fading channels", *J. Commun. Networks,* vol. 18, no. 2, pp. 182–189, Apr. 2016.

3. Q. Wang and P. Y. Kam, "Optimum Detection of Two-Dimensional Carrier Modulations With Linear Phase Noise Using Received Amplitude and Phase Information and Performance Analysis", *J. Lightw. Technol.,* vol. 34, no. 10, pp. 2439–2451, May 2016.

4. T. Song, Q. Wang, M. Wu and P. Y. Kam, "Performance of Laser Inter-Satellite Links with Dynamic Beam Waist Adjustment," *Optics Express*, vol. 24, no. 11, pp. 950–960, May 2016.

5. Q. Wang, T. Song and P. Y. Kam, "Performance Optimization of M-APSK in AWGN and Oscillator Phase Noise with Annular-Sector Detection," in *Proc. IEEE Veh. Technol. Conf. (VTC 2016-Spring)*, Nanjing, May 2016, pp. 1–5.

6. Q. Wang, T. Song, M. Wu, T. Ohtsuki, M. Gurusamy and P. Y. Kam, "Influence of Pointing Errors on Error Probability of Inter-Satellite Laser Communications," in *21st OptoElectronics and Commun. Conf. (OECC)*, Japan, July 2016.

7. Q. Wang, T. Song, M. Wu, T. Ohtsuki, M. Gurusamy and P. Y. Kam, "Impacts of Pointing Errors on Error Probability of Inter-Satellite Laser Communications," submitted to *J. Lightw. Technol.* 2016.

8. Y. Li, Q. Wang, C. Yu, M. Gurusamy and P. Y. Kam, "Performance of Two-Dimensional ML Detector with Laser Phase Noise and Frequency Offset," submitted to *Conference on Lasers and Electro-Optics*, OSA Technical Digest (2017).